DEVELOPMENT OF A SEAMLESS MORPHING WING

MICHAEL PETERSEN

Cape Peninsula
University of Technology

DEVELOPMENT OF A SEAMLESS MORPHING WING

by

Michael Petersen

Thesis submitted in fulfilment of the requirements for the degree

Master of Technology: Mechanical Engineering

in the Faculty of Engineering

at the Cape Peninsula University of Technology

Supervisor: Professor Oscar Philander

Bellville
June 2010

DECLARATION

I, Michael Petersen, declare that the contents of this dissertation/thesis represent my own unaided work, and that the dissertation/thesis has not previously been submitted for academic examination towards any qualification. Furthermore, it represents my own opinions and not necessarily those of the Cape Peninsula University of Technology.

Signed _____ **Date** _____

ABSTRACT

The Cape Peninsula University of Technology (CPUT) Advanced Manufacturing and Technology Laboratory (AMTL) developed an Unmanned Aerial Vehicle (UAV) Technology Demonstrator for the purpose of testing and maturing adaptronic devices. Extending the flight envelope of this unmanned aerial vehicle by increasing its range and endurance is the next step in its development. A seamless variable angle of incidence (sVAI) morphing wing is proposed to increase the lift with little coupling to drag during takeoff; and decrease the drag with little effect on lift during climb, thus increasing the total flight performance of the aircraft. CAD models of the conceptualized sVAI wing and a conventional (CON) wing, as used on the Technology Demonstrator, were modeled. Numerical analyses on these CAD models showed that the sVAI wing concept at a 4° twist decreased the ground roll distance and stall velocity by ±17% and ±31% respectively, as compared to the CON wing in standard takeoff configuration. This allowed for ±11.7% less power required for takeoff allowing the aircraft to get to its operational altitude quicker, thus saving fuel and reducing energy losses; and increasing range and endurance. The results also showed that the sVAI wing concept could reduce the drag during climb by ±14%, but the lift is also proportionately reduced thus having little improvement on the climb phase of flight performance. A prototype of the morphing wing was then conceptualized and designed, using a 3D CAD modeler, and then manufactured. The product development chain produced for this morphing wing included two rapid prototyping machines and reverse engineering technologies. The chain allowed for the rapid manufacturing of light weight and intricate parts. The manufactured wing is then incorporated into a test rig to compare the actual morphing ability of the prototype to the theoretical morphing ability of the CAD model, and thus make flight performance predictions of the actual vehicle. 3D scans were taken of the prototype and then converted to 3D CAD files. The geometrical and topographical deformation of the prototype was then compared to that of the CAD model showing an average difference of ±1.2% and ±3% at maximum positive and negative configurations, respectively. This allowed one to make the prediction that the sVAI wing will increase the performance of the Technology Demonstrator.

FORWARD

The research conducted for this report ran over a course of four years, beginning in August 2006 and ending in June 2010, under the academic supervision of Professor Oscar Philander.

This research was presented at four different conference arenas as listed below.

- In September and November of 2007 a presentation titled "The Effects of a Twisting Wing on Flight Characteristics" was presented at the Technical Aerospace and Unmanned Systems Conference (TAUSC) and at the 8th annual Rapid Product Development Association of South Africa (RAPDASA) Conference, respectively. Preliminary results presented showed that the twisting concept could produce more favourable lift over drag (L/D) values compared to a conventional wing configuration.
- A presentation titled "Aerodynamic Characteristics of a Seamless Twisting Wing for Different Flight Conditions" was presented at the South African International Aerospace Symposium (SAIAS) in September 2008. This presentation underlined the value the twisting wing concept could have in aiding specific phases of the flight envelope due to its ability to increase lift and decrease drag by seamlessly changing the angle of incidence of the wing.
- A paper titled "A Seamless Twisting Wing for Takeoff and Climb Flight Conditions" was presented in November 2008 at the 9th annual RAPDASA conference. The possible effects that the twisting wing could have on the takeoff and climb phases of flight were proposed in the presentation. Numerical results showing the improvement of flight performances during these phases of flight were also presented.

ACKNOWLEDGEMENTS

I wish to firstly express a special thanks to my parents for their love, support, understanding and relentless commitment to see my success. A warm thanks also goes out to the rest of my family for all the well wishes and support.

I would like to thank Professor Oscar Philander for his academic advice, guidance and supervision; and for allowing me the opportunity to work on this project. I am especially thankful to Morne Riddles for his vision and invaluable support in the conceptualisation and design of the project.

I would like to express immense gratitude to my fellow AMTL colleagues that have assisted me in various ways; Michael Sam for his help and advice in the scanning and modelling process, J. B. Kaelo, X. Ngxola, and L. Nangamso for their assistance in the manufacturing process.

I would like to thank Monty Morris and the team at ESTEQ for their advice and support with EFD

I would also like to thank the employees at Jaco Bond for taking the time and their money to offer sound advice and provide adhesive solutions for the manufacturing of the prototype.

TABLE OF CONTENTS

LIST OF FIGURES

LIST OF TABLES

LIST OF SYMBOLS

α	Angle of attack
α_{climb}	Climb angle
η	Propeller efficiency
ρ_∞	Flow stream density
μ_r	Coefficient of rolling friction
C_D	Total drag coefficient
$C_{D,0}$	Zero-lift parasite drag coefficient
c_f	Nominal fuel coefficient
C_L	Coefficient of lift
$(CL)_{max}$	Maximum coefficient of lift
D	Drag
E	Endurance
f	Function
g	Gravity
K	Drag due to lift constant
L	Lift
P_r	Power required
R	Rolling friction
R/C	Rate of climb
S	Wing surface area
S_g	Ground roll
T	Thrust
V_∞	Flow stream velocity
V_{climb}	Climb velocity
V_{LO}	Lift off velocity
V_{stall}	Stall velocity
W	Weight
W_1	Gross takeoff weight
W_2	Gross weight

CHAPTER 1

This chapter is introduced with a scope of the thesis, a brief introduction and description to the CPUT UAV Technology Demonstrator is then given, followed by a background to UAV design, motivation for the research and application of wing morphing technologies, a list of objectives and methods of achieving the mentioned objectives, and a brief summary of existing research in this field of study is given.

1.1 INTRODUCTION

The Cape Peninsula University of Technology (CPUT) Adaptronics AMTL, has developed an Unmanned Aerial Vehicle (UAV) Technology Demonstrator to test and mature their adaptronic devices and systems. The UAV platform specifications include a payload weight of 1.0kg, wing span of 2.50m, length of 1.5m, a maximum take-off mass (MTOM) > 7kg & < 20/25kg, a flight altitude > 150m, and flight beyond the visual line of sight of the pilot. The CPUT Adaptronics AMTL Technology Demonstrator airframe consists of composite materials, wet hand lay-up construction techniques, and fuselage load bearing structures. Flight control systems utilize direct and simple linkages. Ailerons and flaps are individually actuated for each wing, permitting safe operation of the aircraft in the event of actuator or linkage failure.

The Airfoil section considered is specifically selected for its optimal aeronautical characteristics for low speed flight. The airframe is designed to withstand +4G loading on landing, thereby providing structural safety in normal operational conditions. The aircraft can be partially disassembled for transport by a small utility vehicle. The aircraft flight specifications include: maximum speed, Vmax of 100km/h, stall speed, Vstall of $\geq$ 12km/h, cruise speed, Vcruise of 80km/h, loiter speed Vloiter of 60km/h, and Range $\leq$ 5km.

The next phase in the development of this aircraft was to investigate ways to extend its flight envelope by improving its performance.

In most aircraft design a compromise, i.e. making the best means for all the good qualities, has to be reached between factors that are ideal for flight conditions and factors that degrade flight conditions (Kermode, 1996). Focusing on one good quality deteriorates the others, e.g. in the climb phase, to increase the climb rate one would need to decrease drag, and to decrease drag one would need to decrease lift. This can limit mission capabilities and performance platforms for most aircraft designs.

In UAV design, certain attractive points are focused on in order to satisfy certain single mission objectives and performance capabilities (Manzo, 2006). Range and Endurance are important parameters in classifying mission platforms, such as surveillance, target acquisition or combat, for UAVs.

UAVs are usually classed into two types, namely high range and high endurance vehicles. Combat and target, and decoy vehicles fall into the high range category, and are usually characterised with high speeds and high manoeuvrability with high levels of control. Commercial and civil, and surveillance and reconnaissance vehicles fall into the high endurance category, and are characterised with long loiter intervals.

However, future unmanned aircraft may be required to achieve multiple mission objectives in a single platform (Blondeau, 2004). The CPUT Adaptronics AMTL thus developed a UAV Technology Demonstrator to test and mature adaptronic devices and structures that will enable multiple mission objectives in a single platform. To enable this capability the concept of variable geometry has been proposed as a means to extend the capability of this vehicle's platform and therefore increase its performance.

Advances in science and technology have made wing morphing a promising technology for future use on fixed-wing unmanned aircrafts. A seamless morphing wing is able to provide variations in lift and drag to suite different flight conditions by altering its configuration (Henry, 2004). These variable geometry concepts propose the ability to improve flight efficiencies, enable multiple mission capabilities on a single platform, increase the range and endurance and improve on the safety of the flight (Blondeau (2004), Henry (2004)).

New developments in smart materials and new manufacturing capabilities have shown promise of eliminating the problems associated with conventional high-lift systems, such as discontinuities in the wing surface and excessive weight of the actuation system (Poonsong, 2004). These new manufacturing capabilities can allow for easier and inexpensive production of intricate parts. Seamless wing surfaces with lighter and better actuation systems can improve on the aerodynamic performance of a wing.

1.2 SCOPE OF THESIS

This thesis consists of six chapters. Chapter 1 begins with the introduction and background as discussed above. The objectives and the methodology follow. A literature survey is then presented and then followed by a brief discussion on the relation between the literature reviewed and the research done in this thesis.

Chapter 2 follows with a detailed description of the takeoff and climb phases, both analytically and theoretically. An explanation of high lift devices is then given, with a discussion of current and proposed morphing concepts. A detailed description of the analysis then follows, with explanations of the CAD models used for the analyses of a morphing concept and a conventional wing. An explanation on the takeoff and climb phase of flight analysis set up and protocol are also discussed here. Lastly in chapter 2, the computational fluid dynamics (CFD) software used for the analyses is described.

Chapter 3 is a discussion of the results. This is where the outputs of the takeoff and climb flight phase analyses obtained on the CFD software package, are discussed.

Chapter 4 then follows with a detailed description of the design and manufacturing of the morphing wing.

The scanning of the manufactured wing is then discussed in chapter 5. This is followed by a detailed explanation on converting the scanned image to a 3 dimensional solid CAD model. The chapter is concluded with a comparison between the morphing CAD model used in the analysis and the 3D CAD model converted from the scans of the manufactured prototype.

In the conclusions a summary of the work presented in this thesis and recommendations for improvement are given. The thesis concludes with a list of references and appendix.

1.3 OBJECTIVES

The primary objective of this study was the development of a seamless wing morphing concept to be used during the take-off and climb condition of the CPUT Adaptronics AMTL Technology Demonstrator flight envelope (see in figure 1.1) and its effects on the overall performance of this vehicle. This seamless morphing concept should have the ability to increase the takeoff and climb performance thus increasing the overall performance of the aircraft.

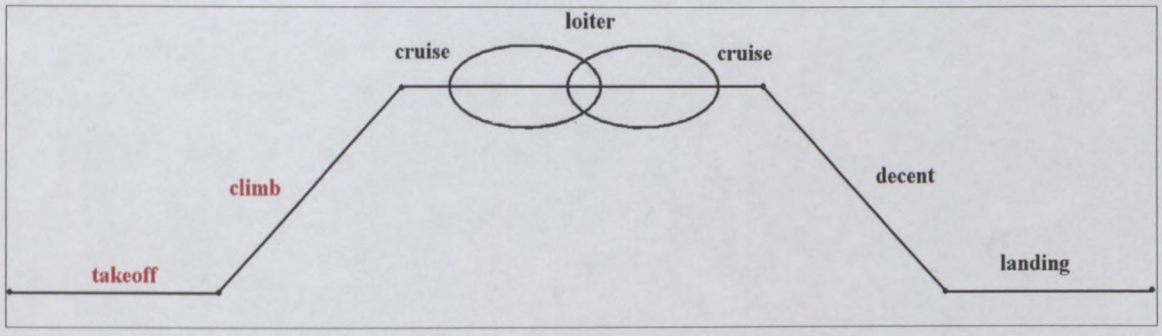

Figure 1.1: Proposed flight phases of the CPUT Adaptronics AMTL Technology Demonstrator.

In order to achieve the primary objective, the following sub-objectives should be achieved.

1.3.1 To investigate the effects that a given wing morphing concept could have on the takeoff phase of flight of the vehicle using numerical methods;

1.3.2 To investigate the effects that a given wing morphing concept could have on the climb phase of flight of the vehicle using numerical methods;

1.3.3 To investigate the effects that a given wing morphing concept could have on the power consumption of the vehicle during these flight phases;

1.3.4 To investigate the effects that a given wing morphing concept could have on the overall range and endurance of the vehicle;

1.3.5 To investigate the effects that a given wing morphing concept could have on the overall flight performance of the vehicle;

1.3.6 To manufacture a wing for the CPUT Adaptronics AMTL Technology Demonstrator that incorporates the wing morphing concept;

1.3.7 To incorporate this wing into a test rig to determine its morphing ability and thus make predictions on the flight performance of the actual vehicle.

In achieving the above primary objective, one could envision a method of increasing the amount of lift on the wing with less coupling to drag during takeoff and decreasing the amount of drag with little effect on the lift during climb. This would decrease the ground roll (S_g) and time taken before liftoff, and increase the excess power during climb therefore increasing the rate of climb.

The concept used in this study is based on a ***seamless V***ariable ***A***ngle of ***I***ncidence (***sVAI***) ***M***orphing ***W***ing. With the ability to generate more lift during ground roll (S_g) by increasing the angle of incidence before rotation, one would reduce the stall speed thus making flight more efficient and safer. A reduced takeoff time or distance would mean less fuel consumption during this flight phase. Altering the angle of incidence to reduce the amount of drag during climb would decrease the power required and the time taken to climb. Less power required would mean less energy consumption. With this the range and endurance of the aircraft is increased, allowing for more distance and time during its service phase of flight. Also, asymmetrical variations in angle of incidence of the wings could allow for differential lift and providing a means of effective roll control.

1.4 METHODOLOGY

To investigate the effects of the sVAI wing, CAD models of the conventional (CON) and sVAI wings were designed and developed. These models were intended to predict the flow characteristics of the wings by running analyses on them and obtaining results. The results were observed and compared to find the most favourable wing design and configuration.

Analyses were run on the CAD models at takeoff configuration. This was done to obtain a value for the velocity at lift off (V_{LO}) for each wing configuration and then compare the results. Values for maximum coefficient of lift (CL_{max}) and drag (D) were also obtained and used to determine the ground roll (S_g) for each wing configuration during takeoff, where

$$S_g = f(V_{LO} f(V_{stall} f(CL_{max})))$$

therefore,

$$\textit{Optimal takeoff efficiency} = < CL_{max} \Rightarrow V_{stall}, > V_{LO} \textit{ ; resulting in } > S_g .$$

An increase in CL_{max} decreases V_{stall}, therefore decreasing V_{LO} and enabling a decrease in S_g. This, therefore allows for a favourable wing design.

Analyses were run on the CAD models at climb configuration. This was done to obtain a climb angle (α_{climb}) and values for the maximum power/glide ratio ($CL^{3/2}/CD_{max}$), and then compare the results. These values were then used to determine the rate of climb (R/C), where

$$R/C = f(P_r f(CL^{3/2}/CD))$$

therefore,

$$\textit{Optimal climb efficiency} = > CD = < CL^{3/2}/CD \textit{ ; resulting in } > P_r = < R/C$$

An increase in $CL^{3/2}/CD$ decreases P_r (power required to climb), thus enabling an increase in R/C. This, therefore allows for a favourable wing design.

The value of $CL^{3/2}/CD$ was obtained for each of the different wing designs and configurations to predict the power usage during takeoff and climb. The higher the value of $CL^{3/2}/CD$, the less power is consumed for the flight phases.

In determining the effect of the different wing configurations on S_g and R/C during takeoff and climb respectively, the effects on the overall range and endurance of the aircraft are also determined. The less S_g and the quicker R/C is, the more favourable the effects on the overall range and endurance are. Therefore, in observing all of the above parameters the wing concept with the most efficient overall flight performance could be determined.

The sVAI wing was developed, manufactured and tested at the CPUT AMTL Adaptronics. Advanced manufacturing processes were used in the development and

manufacturing of the flexible section, along with standard fibre glass hand layup methods. A flexible skin was prepared to cover the skeleton of the flexible section, and should allow no ripples or adverse geometry gradients that could cause parasite drag to occur.

The morphing ability of the wing was then tested on a test rig. Scans were taken of the wing at different angles of morphing. These scans were then converted to 3 dimensional CAD files so that the geometry can be compared to that of the initial CAD model. This was done to test the credibility of the CAD model and predict the flight performance of the actual aircraft when equipped with the sVAI wing.

1.5 LITERATURE REVIEW

1.5.1 Aeromorphing

The first morphing wing was designed by the Wright Brothers and was used on the Wright flyer (shown if figure 1.2). They used a method of warping the camber of the wings to aid in the steering of the aircraft. (Historic milestones in Aerospace, 2003)

Figure 1.2: The Wright Flyer. (Historic milestones in Aerospace, 2003)

These days there are numerous different morphing concepts under investigation, such as variable aspect ratio or span morphing, variable camber, variable span wise camber, variable sweep, wing twisting, wing curling and twisterons. Morphing wings propose to increase the range and endurance of an aircraft, and allow for multiple mission capabilities on a single platform.

1.5.2 Flight control energy requirements

Johnston et al, 2003 have developed a model to predict the control energy requirements of a morphing aircraft. They have concluded that morphing vehicles allow for less aerodynamic energy requirements than conventional vehicles due to the independent spanwise deflection in certain morphing applications even though they induce a strain energy not found with conventional aircraft.

Johnston et al proclaim that at higher flight speeds and with advanced wing structures a morphing wing might supersede a conventional wing in flight control energy requirements.

1.5.3 Variable aspect ratio and span morphing wing.

The aspect ratio is a powerful indicator of the general performance of an aircraft wing. It is represented as the ratio between the aircrafts wingspan and wing area, and is categorized as either a high or low aspect ratio.

The idea of a variable aspect ratio wing is to generate flight behaviour characteristic of high and low aspect ratios, on the same aircraft. Variation of aspect ratio affects the amount of lift produced on the wing directly. It could also provide roll control by means of differential lift. Blondeau, 2004 suggests that increasing an aircrafts wingspan will tend to increase that aircrafts endurance.

Figure 1.3 shows the telescopic wing developed by J. Blondeau in different aspect ratio configurations for different flight situations.

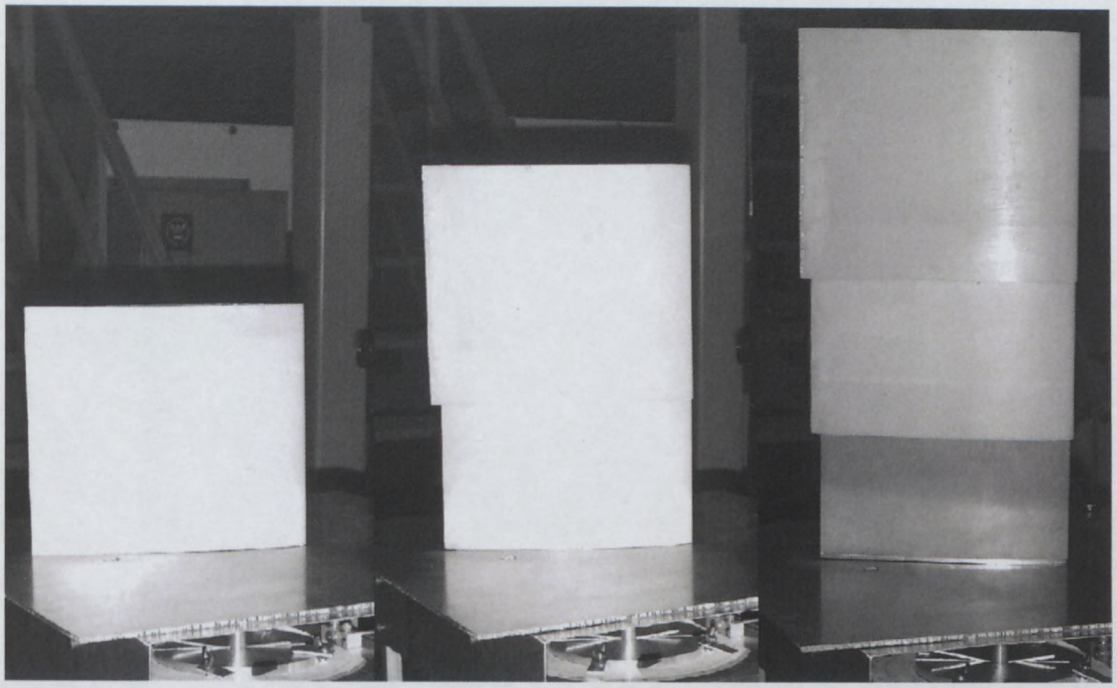

Figure 1.3: Variable aspect ratio wing using telescopic spars at different stages. (Blondeau, 2004)

Blondeau, 2004 designed, developed and tested a pneumatic telescopic wing that used pneumatic actuators to change the aspect ratio of the wing. His wing is able to undergo a 230% change in aspect ratio while supporting aerodynamic loads. Wind tunnel test results and theoretical results however, confirm that the aerodynamic performance of the telescopic wing suffers slightly of parasitic drag. Blondeau also states that a recent theoretical study of variable span wing shows advantages such as drag reduction, range increase and good roll motion control.

In the development of a variable aspect ratio wing, it was found that the inclusion of ailerons would not be feasible in the wing design. Therefore a method of morphing the telescopic wings asymmetrically for use in roll control was researched.

Henry, 2005 developed the span morphing wing to test the efficiency of its capabilities in roll control. The span-morphing wing uses asymmetric morphing so as to increase the lift on one side of the craft, thus creating a roll motion. Henry founded in his experiments that the span-morphing wing could produce roll coefficients that are equivalent to, and even greater than those from ailerons. Figure 1.4 shows two stages of the span-morphing wing.

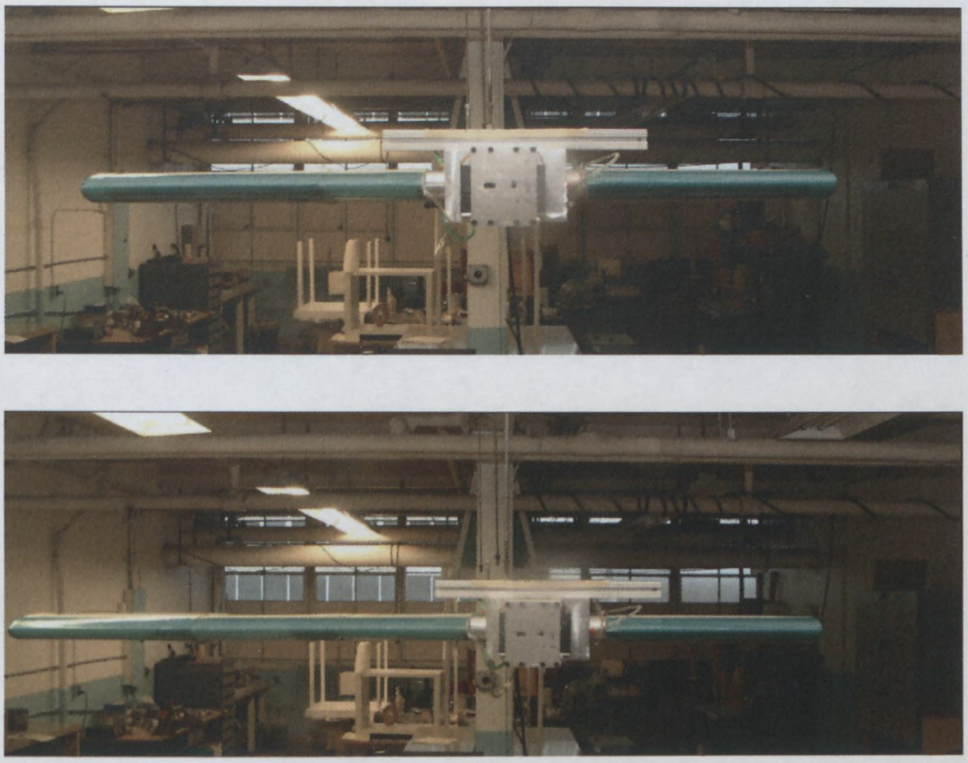

Figure 1.4: The span morphing wing at 60%-40% (top), and 100%-40% (bottom) morphing stages. (Henry, 2005)

1.5.4 Variable chordwise camber

A variable camber device is a mechanism that allows for change in the curvature of an airfoil as described by Poonsong, 2004. Essentially, this change in geometry can allow for roll, yaw and pitch control. It also improves on the aerodynamic performance of an aircraft.

The most significant variable camber devices currently used in most aircrafts are high-lift devices such as leading-edge slats and trailing-edge flaps. These devices have demonstrated very promising results in reducing fuel consumption.

Camber variation can be used to steer an airplane. It can also be used to improve its flying capabilities at specific times. This can be done by directly influencing the amount of lift and drag produced on the airfoil. (Poonsong 2004)

Figure 1.5 and 1.6 show cross sections of the variable camber wing.

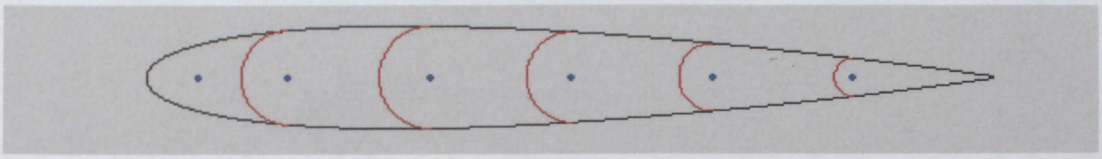

Figure 1.5: Cross section drawing of a multi-section variable camber wing. (Poonsong, 2004)

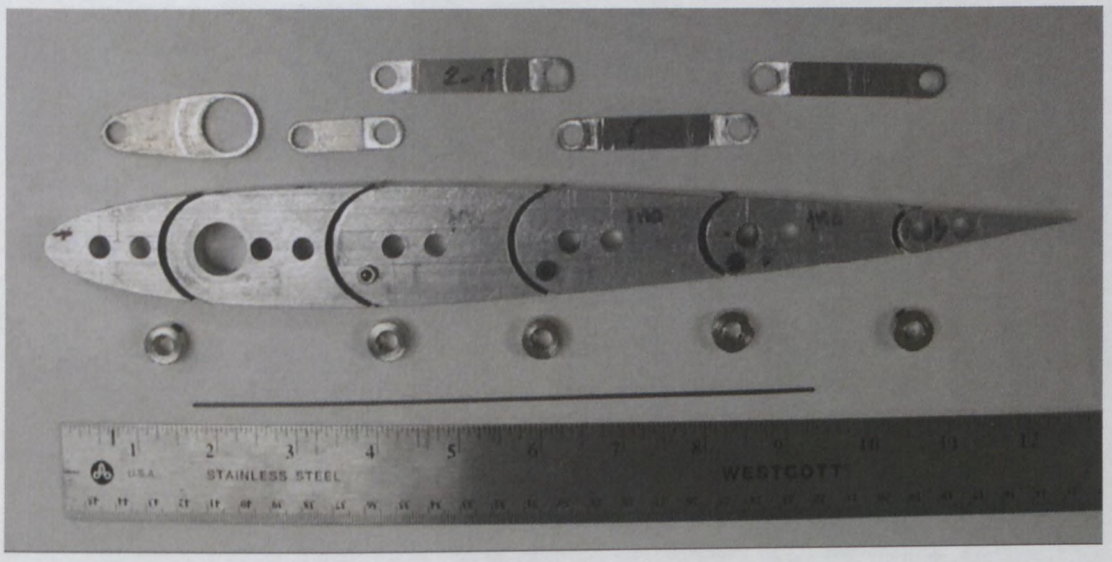

Figure 1.6: Cross section of the multi-section variable camber wing. (Poonsong, 2004)

The variable chordwise camber wing designed by Prasobchok Poonsong has the ablility to undergo an 8% camber change. The wind tunnel test results showed higher stall angle and higher lift-to-drag ratio compared to a rigid wing in camber, however complications were suffered due to the wing skin.

1.5.5 Variable sweep

Wing sweep is used to alleviate compressibility effects (Anderson J.D., 2008). Sweep increases the critical Mach number to delay the onset of drag divergence for a subsonic aircraft, and reduces the wave drag in supersonic flight. Sweep variation therefore allows for control over Mach number in subsonic flight, and also allows for stability control. (Anderson J.D., 2008)

Figure 1.7 illustrates how drag divergence is delayed for subsonic flight. When a sweep angle (Λ) is introduced to the wing, $M_\infty \cos\Lambda = Mn$ becomes the flow normal to the leading edge and sees the shape of the wing. The tangent component (Mt) does not contribute to the pressure variation. Therefore the Mach number on the wing is reduced by $\cos\Lambda$.

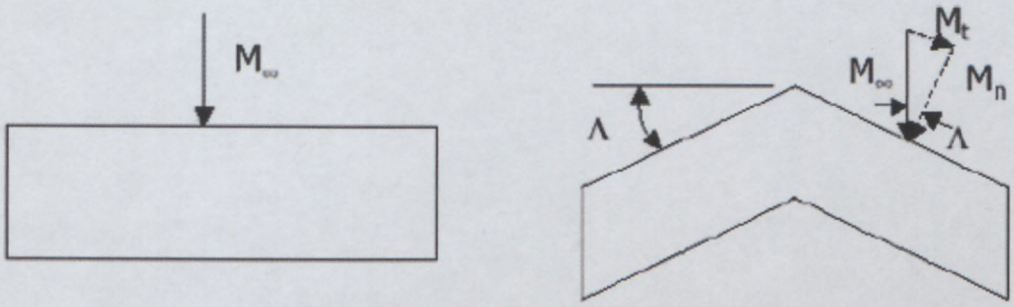

Figure 1.7: Compressibility effect of Mach <1. (Anderson J.D., 2008)

1.5.6 Variable spanwise camber

The Hyper Elliptic Cambered Span morphing wing (HECS) was designed by Dr Barry Lazos and developed by researchers at NASA Langley, and was modelled after a the wing configuration of a seagull in high-speed gliding flight (Lazos, 2005). It was developed for investigation into roll and yaw control (Manzo, 2006). The geometry of the wing is modeled by "a hyper-elliptic function in leading edge and trailing edge sweep and span-wise curvature". Manzo states that when the wing tips are furled, they act as modified winglets, limiting vortex roll-up from the lower to upper surface of the wing. In doing this it further increases the lift-to-drag ratio over a certain range of angle of attack.

As seen in figure 1.8, a hingeless, morphable panel located at the trailing edge is used for roll and pitch control while a continuous morphable wing tip controls roll and yaw.

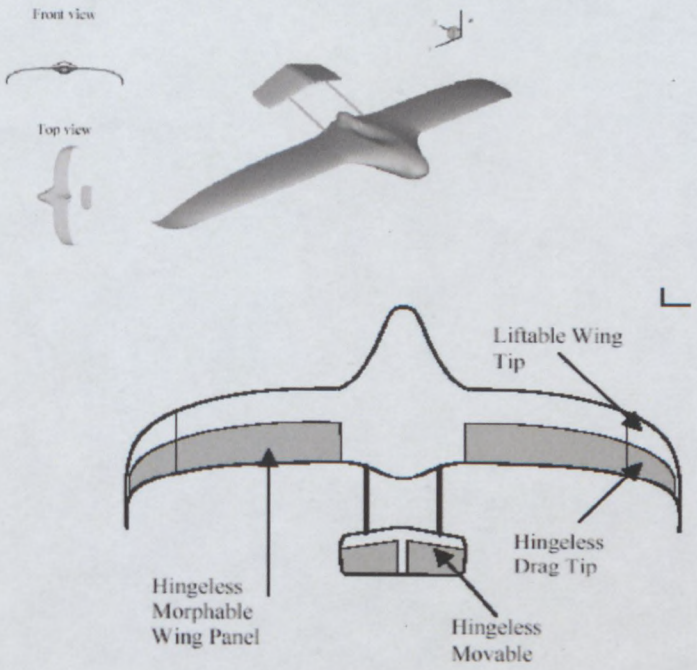

Figure 1.8: Hyper Elliptic morphable wing (Manzo, 2006)

1.5.7 Flexible wing morphing on MAVs.

Wing curling, wing twisting, multi-point wing shaping, leading edge twisting, variable gull wing angling, and wing tail folding are all methods of wing geometry variation used in micro air vehicles (MAV's). This type of morphing is being explored to optimize and enhance control of the aircraft during agile and aggressive manoeuvres (Lind et al). Application of flexible wings to MAVs help in flight stability and structural durability during gusty wind and unsteady aerodynamic conditions (Ifju et al, 2002).

Tests were conducted on these different wing morphing configurations at the Department of Mechanical and Aerospace Engineering, University of Florida by Lind, Abdulrahim, Boothe and Ifju. The following are the conclusions of their tests.

1.5.7.1 Wing curling

The morphing is done asymmetrically, so one wing is curled while the other remains undeflected, as shown in figure 1.9. The curling causes a greater angle of attack and angle of incidence on the wing, which results in more lift on the curled wing. This

causes a positive roll moment. There is some amount of pitch and yaw due to the asymmetric configuration.

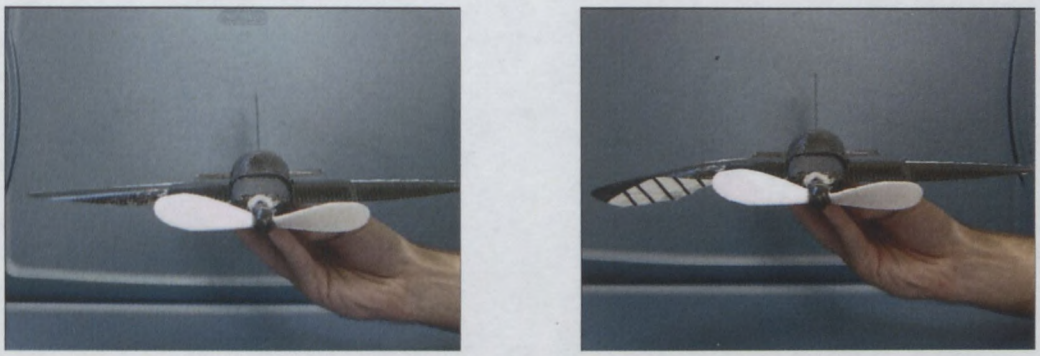

Figure 1.9: Front view showing undeflected wing (left) and morphed wing (right). (Lind et al)

Lind, Abdulrahim, Boothe and Ifju found that the wing curling produced satisfactory results in roll controllability throughout the airspeed range encountered during high-speed dives, landing or approach phases and cruise. The curling produced very good results in roll and turning, but failed in aggressive manoeuvres. Large incidence angles formed near the deformed area of the wing, because of wing deflection incurred by wing curling. This made control of the aircraft difficult through aggressive manoeuvres.

1.5.7.2 Wing twisting

Wing twisting exhibits highly desirable control characteristics in flight. It has extremely responsive roll control across a wide range of airspeeds. Lind et al found that the wing twisting remains effective at low speeds. At near level flight stall, it is still able to command a turn and recovery from turbulent disturbances. At higher speeds, the roll response is also effective, although the magnitude of the roll rate increases. A torque rod forces the wing to undergo a twisting deformation, by means of actuation by a servo. The torque rod configuration is shown in figure 1.10.

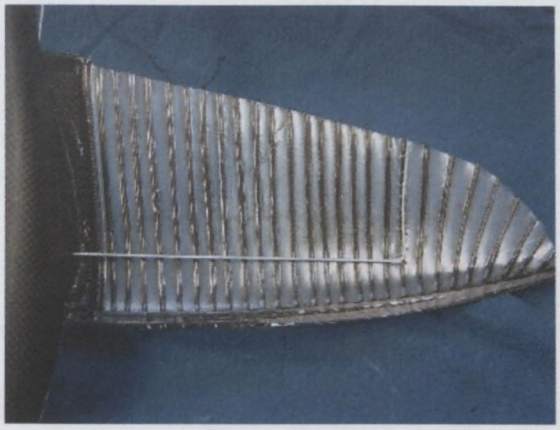

Figure 1.10: Twisting wing with torque rod. (Lind et al)

Little amounts of yaw are experienced when the aircraft, with twisting wing, was subjected to continuous rolling. Several complete rolls can be completed without an appreciable change in heading or pitch attitude.

1.5.7.3 Multi-point wing shaping

The multi-point wing-shaping aircraft is a method of increased control over the wing in wing twisting. Four rotating spars actuate the wing. These are attached to a flexible, extensible wing skin. The basic idea of this method is to have some control of the lift distribution over the wingspan. Each of the four rotating spars can be controlled independently, a variety of complex shapes to be achieved. Therefore this type of morphing can be useful for longitudinal control, longitudinal trim, minimum drag, maximum drag, or stall resilience in addition to commanding roll rate.

The results of this wing are similar to that of wing twisting, though roll rates and performance measures are considerably higher when the entire wing is actuated differentially (i.e. using both wingtips and midboard sections). Figure 1.11 shows the different stages of wing morphing of the aircraft.

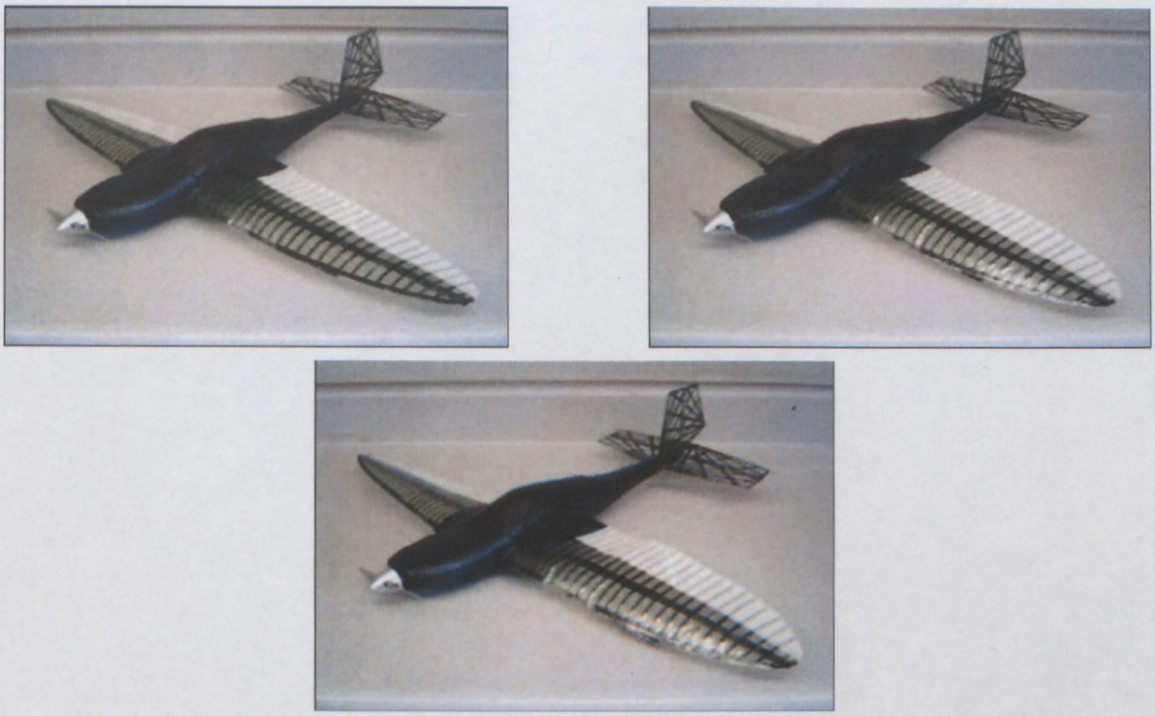

Figure 1.11: Wing shaping MAV showing neutral position (top right), wingtip morphing (top left), and full wing morphing (bottom). (Lind et al)

1.5.7.4 Leading edge twisting

Leading edge twisting is a type of morphing intended to reduce the coupling and saturation issues associated with the elevons. This is done by separating roll and pitch control into the wing and elevator surfaces respectively.

The only mount points for the wings are two pylons as shown in figure 1.12. The leading-edge morphing therefore generates a global twist over the wings. The resulting shape of the wing is shown in figure 1.13.

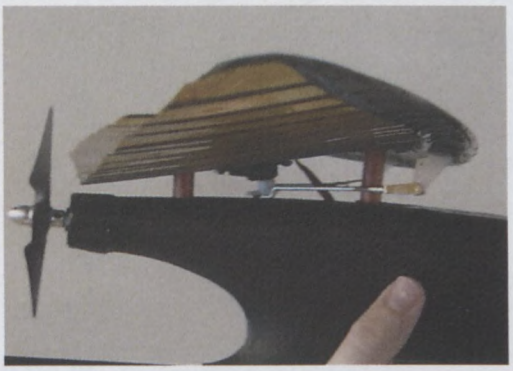

Figure 1.12: The wing mounted on two pylons. (Lind et al)

Axial rolls are easily performed with the morphing. Limited pitch or yaw divergence is shown throughout the roll. This indicates that the undesirable coupling associated with elevons has been reduced.

Figure 1.13: Front view of aircraft showing right hand morphing (left), left hand morphing (middle), and neutral position (right). (Lind et al)

1.5.7.5 Variable gull wing angling

This type of wing morphing changes the angle between the inboard and outboard wing sections in flight to vary performance capability.

Increasing the gull-wing angle in the positive direction causes the vehicle to become highly stable about the roll axis. It also decreases the glide angle considerably allowing the aircraft to descend at steep angles without increasing airspeed.

At negative gull-wing angles, the roll response is increased and the vehicle is generally more maneuverable. However, the stability about the roll axis decreases considerably. Negative gull wing angling may be best suited for aggressive, high-speed flight, provided a stabilizing controller is used to help prevent divergence. Figure 1.14 shows the gull-wing at different wing angles.

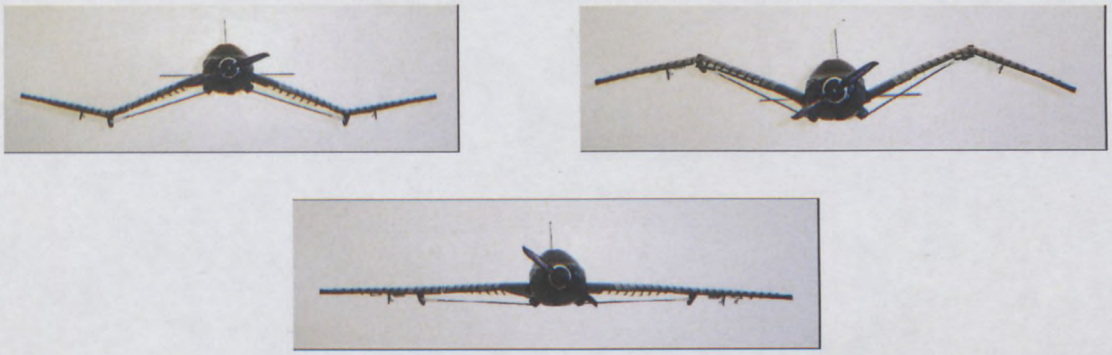

Figure 1.14: Negative gull wing (top right), positive gull wing (top left), and neutral position (bottom). (Lind et al)

1.5.8 Twisterons

A method of reducing the induced drag through spanwise circulation control on a planform wing was developed and published by Dr. W. F. Philips. This is done by implementing, either a geometric or aerodynamic twist in the wing, which is commonly known as "washout". (Philips, 2003)

Philips states that if the twist is implemented properly the induced drag can be minimized by up to 15%. Induced drag is +/- 50% of the total drag on a plane in cruise phase and 90% of the total drag in the landing phase.

However, if a fixed twist is implemented into the wing, the wing can only be optimised for one designed coefficient of lift or a comprise must be made for a range of coefficient of lift values for different mission phases.

This limitation can be avoided by employing full-span trailing-edge flaps that are able to twist along there length and produce a spanwise variation in zero lift angle of attack. These flaps are referred to as twisterons. They are able to deflect asymmetrically as well to produce moments for roll control.

Figure 1.15a and b show the twisterons in 0°. flap deflection with a washout set to reduce induced drag at coefficient of lift at 0.6, and 15°. flap deflection with a washout set to reduce induced drag at coefficient of lift at 1.4 respectively.

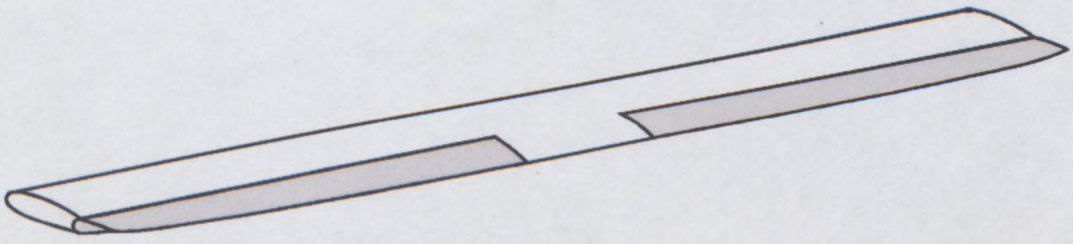

Figure 1.15a: Twisteron configuration with no flap deflection and washout set to minimize induced drag at CL = 0.6. (Philips, 2003)

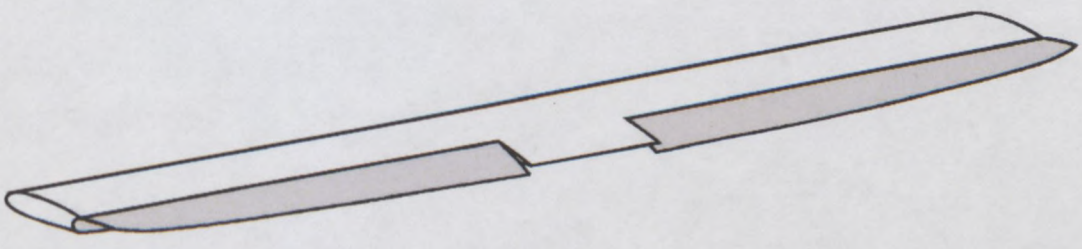

Figure 1.15b: Twisteron configuration with 15° flap deflection and washout set to minimize induced drag at C_L = 1.4. (Philips, 2003)

Philips, Alley and Goodrich, 2004 developed a more practical form of the lifting-line solution for finite wings that allow for wing planform, wing twist, control surface deflection and rolling rate to be accounted for separately. This form of the equation was used to predict the effects that the twisteron has on the induced drag experienced by the wing. (Philips, Alley &Goodrich, 2004)

1.5.9 Active Aeroelastic Wing

The active aeroelastic wing (AAW) developed by Pendleton et al, 2000 is, as described by them, a multidisciplinary and synergistic technology. It integrates air vehicle aerodynamics, active controls, and structures advanced technology together to maximize air vehicle performance. In using wing aeroelastic flexibility for a net benefit through the use of multi leading and trailing edge control surfaces, and taking advantage of thin, swept fighter wings with a high aspect ratio that can be aeroelastically deformed into shapes, these technologies allow for optimum performance of an aircraft equipped with these wings.

The AAW control surfaces promote favourable wing twist at higher dynamic pressures. The energy of the airstream is employed to twist the wing with very little control surface motion with the wing itself creating the control forces. The traditional wing control surfaces—trailing edge ailerons and the leading and trailing edge flaps—are used to provide the aerodynamic force needed to twist or "warp" the wing. (Pendleton et al, 2000)

The benefits of AAW technology are substantially increased control power, reduced aerodynamic drag, reduced manoeuvre loads, and reduced aircraft structural and takeoff gross weight. (Pendleton et al, 2000)

Figure 1.16: NASA's Active Aeroelastic Wing (AAW) F/A-18A research aircraft. (NASA, 2008)

Data obtained from the first flight phase of NASA's Active Aeroelastic Wing (AAW) F/A-18A research aircraft, shown in figure 1.16, was used to refine wing effectiveness models and design the AAW flight control laws. The second phase of research flights to demonstrate the AAW concept with effective control laws was set to begin in early 2004. (Pendleton, 2000)

NASA say the test aircraft has been modified with additional actuators, a split leading edge flap actuation system and thinner wing skins that will allow the outer wing panels to twist up to five degrees. Project engineers hope to obtain almost equivalent roll performance of production F/A-18s at transonic and supersonic speeds without using the horizontal stabilators and with smaller control surface deflections. (NASA, 2008)

AAW research could also enable thinner, higher aspect-ratio wings on future aircraft, which could result in reduced aerodynamic drag, allowing greater range or payload and improved fuel efficiency. (NASA, 2008)

1.5.10 The variform wing concept

The variform concept proposes storing the fuel in the wings of the aircraft and as the fuel reduces during flight the wings would slowly morph into a sleeker profile thus reducing drag and allowing less fuel to be consumed. This would then extend the aircrafts range and endurance. (Gano & Renaud, 2002)

When the bladder is filled the wing profile would look like the outer profile shown in figure 1.17, and when the bladder is empty the shape would look like the inner filled profile.

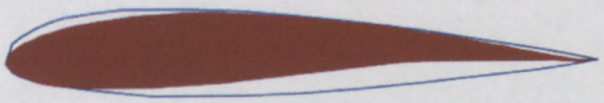

Figure 1.17: Variform wing concept. (Gano & Renaud, 2002)

One way of doing this, explained by Gano and Renaud, is to store the fuel in balloon like bladders that interact with the structure of the wing, as shown in figure 1.18.

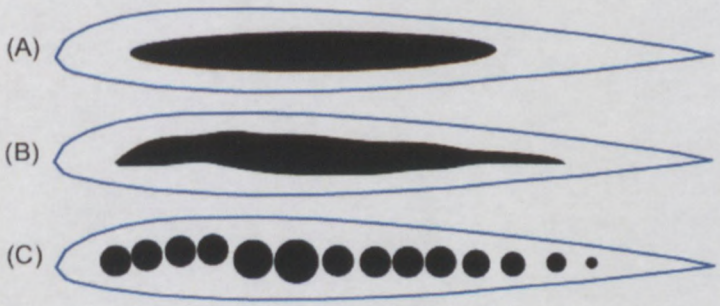

Figure 1.18: Possible fuel bladder configurations. (Gano & Renaud, 2002)

Gano and Renaud proclaim that a more complete model and analysis should still be completed to prove the actual potential of this concept. Also a suitable material that will allow for the deformation with the needed stiffness needs to be found.

1.5.11 Aft swept wing tips

The fastest swimming marine animals and the most supreme aerial animals have evolved over millions of years to adopt crescent-shaped or aft-swept tail fins and wing tips respectively to allow for the most efficient means of getting around. This was considered to be surprising as it is/was generally thought that wings with elliptical planforms produced the least induced drag and the most efficient aerodynamics. (Burkett, 1989)

This is because the lifting surface theory used to model unswept planar wings is not very reliable for swept wings, where the wake is modelled as a planar trailing vortex sheet. Swept wings produce non planar wakes and vortex roll ups on the free edges that are progressively become more dominant as the wing becomes more swept. An important characteristic of swept wings that is not taken into consideration by conventional lifting surface theories is that the wake on a swept wing has a tendency to calm and adopt a more freestream orientation. (Burkett, 1989)

Analyses of the effects of these wake non planarities showed that induced drag can be reduced significantly when a swept wing tip is used. Reductions of ±4% were found to be possible at moderate angles of attack. (Burkett, 1989)

1.5.12 Biologically inspired Fixed-wing configurations.

A study was performed on four biologically inspired fixed wing configurations, namely:

- The Gull wing, which was modelled after the wing of a sea gull in soaring flight. The wing, however, had a smaller aspect ratio and modifications had to be made to produce the desired wing configurations. (Lazos, 2005)

- The Shark wing, which was modelled after the pectoral, dorsal and caudal fins of the great white shark. (Lazos, 2005)
- The Wavy-leading-edge wing, which was a wing modelled with a sine wave curvature added to the leading edge. This was inspired by the bumps along the leading edge of the pectoral fin of a humpback whale. Studies showed that these irregularities enhanced maneuverability through delayed stall. (Lazos, 2005)
- The Hyper Eliptic Cambered Span (HECS) wing, which is discussed in section 1.2.6. (Lazos, 2005)

The performances of the wings were tested and compared to a baseline wing modeled with an elliptical leading edge and a straight trailing edge. This configuration was chosen as a baseline because numerous computational tests showed that this planform demonstrated the best induced drag factor efficiency than any other planform tested with an elliptic chord. (Lazos, 2005)

All of the wings had the same span and chord lengths.

Lazos states that the tests showed that in comparing inviscid span efficiency factors and lift-to-drag ratios, the Shark and the HECS wings performed better than the baseline wing, with the Shark wing performing the best. However, pitching-moment characteristics showed that the Shark wing would have a severe pitch recovery moment which would be detrimental in flight.

Lazos found that the HECS wing maintains an improvement over the baseline wing with suction side boundary layer tripping, however the Shark wing's performance falls below the baseline wing. Untripped boundary layer conditions show the baseline wing having the expected tip vortex pattern, and the Shark and HECS wings having a more complicated pattern with counter-rotating vortices at the wing tips of both wings. It is found that the flow for the baseline and HECS wings do not change dramatically when the suction side boundary layer is tripped. The Shark wing, however, experiences flow reversal on the suction side and thus flow degradation. (Lazos, 2005)

1.5.13 Variable camber compliant aircraft tail

Good, 2003 has developed a structural optimization program that can be used to optimize the topology of an aircraft tail section, which could ultimately lead to the design of a variable camber compliant tail. A variable camber tail eliminates the discontinuity between the airfoil and flap. The structural optimization program links a finite element program to an aerodynamic code and an optimization program. This allows for optimal structural design while taking aerodynamic factors in to place. (Good)

The variable camber compliant aircraft tail was developed using this program to maximize the trailing edge's tip deflection ability. Figure 1.19 shows how the program optimized the structural integrity of the trailing edge. (Good)

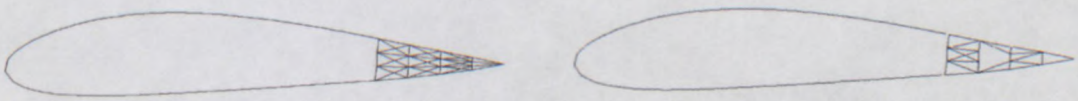

Figure 1.19: Tail section with excess beams in trailing edge (left), optimized trailing edge of tail section (right). (Good, 2003)

It was found that the trailing edge is able to provide a vertical deflection of ±4.27°, and undergoes a 0.9° deflection due to aerodynamic forces (Good, 2003). The trailing edge mechanism was then manufactured out of ABS plastic and using a CNC laser cutter (Good, 2003). The end result is shown in figure 1.20.

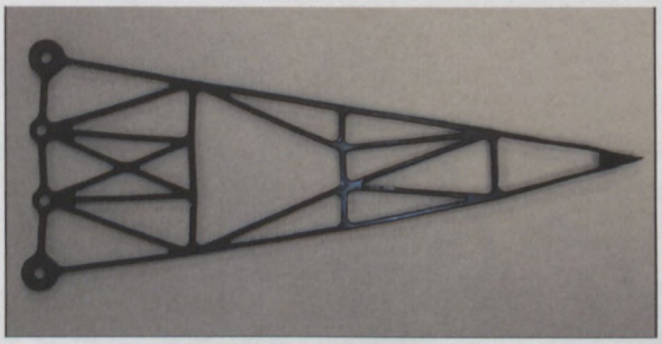

Figure 1.20: Manufactured trailing edge mechanism. (Good, 2003)

Good suggests that the program can also be used to design three dimensional compliant wings to have the ability to vary there camber or twist.

1.5.14 Numerical investigation into wing morphing on a Horten type swept wing.

The inspiration for this study came from the fact that tailless aircraft, with their supreme efficiency and low parasite drag, have no proper control mechanisms and therefore are forced to compromise there efficiency for control. The morphing ability of variable twist is to be introduced to the Horten wing and Vishwanathan, 2007 has conducted numerical research on the flow characteristics of the wing at various morphing stages and compared them to conventional wing geometries. The Horten wing is shown in figure 1.21.

Figure 1.21: The Horten-IV (Vishwanathan, 2007)

Three dimensional models of the conventional and morphed wing were simulated using a program called CMARC at various stages of flight, and the results were compared to actual wind tunnel data. CMARC produced results in a short time period and inexpensively, with its C_L predictions with in an error range of 7 – 23% for the morphing wing and 8 – 14% for the conventional wing. Drag predictions were poor as expected states Vishwanathan.

Vishwanathan found that the morphed wing had superior performance over the conventional wing for the conditions tested.

1.5.15 Current UAV designs

UAVs can be typically classed into five functional categories, namely target and decoy, reconnaissance, combat, research and development, and commercial and civil applications. (UAVs)

UAVs that fall into the target and decoy, and combat categories are usually equipped with wings that have low aspect ratios and are normally in a swept or delta configuration. They fly at high speeds, usually close to Mach Number, therefore use the swept configuration for control over Mach number and allowing for stability control. Low aspect ratio allows for high manoeuvrability and control at high speeds. The aircraft in these categories are normally judged and classed on their range ability, i.e. how far they can go on a tank of fuel. The differences between these two classes are that combat UAVs, or UCAVs, are typically equipped with ammunition and used in attack. Target and decoy UAVs are used for testing and to confuse the enemy respectively.

Figure 1.22: The Boeing X-45A demonstrator UCAV (List of unmanned aerial vehicles)

The Boeing X-45A demonstrator (figure 1.22) is a stealthy tailless combat UAV with a 45 degree swept wing configuration, and has a range of 600km. The ADM-20 Quail (figure 1.23a) is a decoy UAV with wings and tail that fold away for easy storage inside Bomber aircrafts. It had a range of 740km and a speed of 1045km/h. The BMQ-74 Chukar (figure 1.23b) is mainly used for training exercises. (Unmanned aerial vehicles)

Figure 1.23: a) ADM-20 Quail (left) used for decoy. b) BQM-74 Chukar (right) used as a target. (Unmanned aerial vehicles)

Commercial and civil, and reconnaissance classed UAVs are usually equipped with high aspect ratio wings that have a straight wing configuration. This is done to achieve high endurance, and long loiter intervals. These UAVs are typically used for surveillance and tactical intelligence; therefore need to be airborne for long periods of time to gain information. The differences between these two classes are that reconnaissance UAVs are used in war situations and are usually bigger. Commercial and civil UAVs are to be used in civilian skies; therefore there are safety concerns that restrict certain aspects in the design of these aircrafts. (List of unmanned aerial vehicles), (Unmanned aerial vehicles)

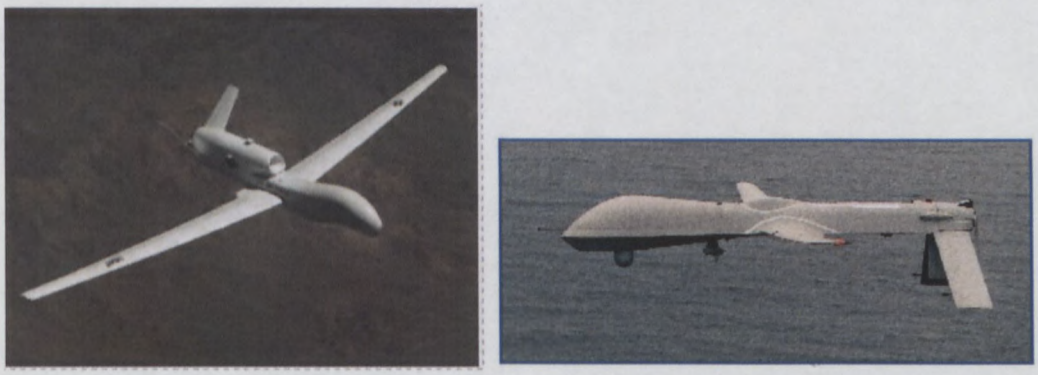

Figure 1.24: a) RQ-4 Global Hawk (left) and b) RQ-1 Predator (right) used for reconnaissance. (Unmanned aerial vehicles)

The RQ-4 Global Hawk (figure 1.24 a) and RQ-1 Predator (figure 1.24 b) are both long loiter reconnaissance UAV aircrafts. The Hawk has a length to wingspan ratio of 1: 2.62. It has an endurance of 34hrs and a cruise speed of 650km/h. The Predator has a ratio of 1: 1.6, an endurance of 24hrs and a cruise speed of 130km/h. (List of unmanned aerial vehicles), (Unmanned aerial vehicles)

The Aerostar (figure 1.25) is a tactical commercial UAV that can deliver high quality real time intelligence for law enforcement in a city. It has been developed in conjunction with the Israel traffic police, for monitoring of traffic offenders. It has a length to wing ratio of 1: 1.4, an endurance of 14hrs, a loiter speed of 31.8km/h, and a dash speed of 58.3km/h. (Aeronautics, 2007)

Figure 1.25: Aerostar UAV used for commercial and civil applications (Aeronautics, 2007)

The current UAV designs use mechanical technologies like ailerons, rudders, flaps, slots, slats and elevators for its control systems, as in figure 1.26. These exert forces around the aircrafts roll, pitch and yaw axes, and increase and decrease amounts of lift and drag experienced by the aircraft (Anderson J.D., 1999). However, these technologies are not seamless, and therefore produce unwanted amounts of drag. The geometry of these control systems creates adverse pressure gradients when activated and cause separation when put through a flow field.

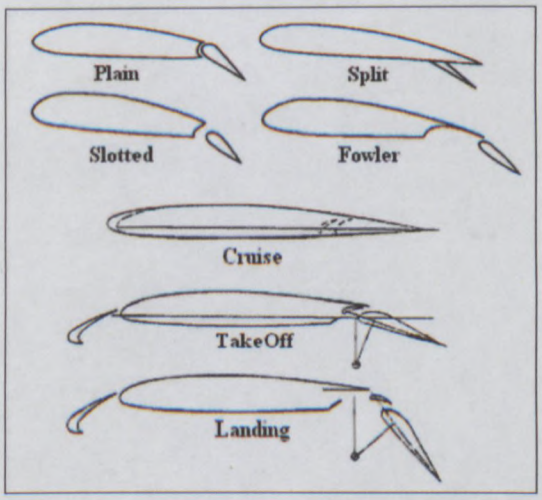

Figure 1.26: Several Types of Flaps and Typical double-slotted flap/ leading-edge slat high lift system. (Anderson J.D., 1999).

1.6 RELATION OF WORK TO LITERATURE SURVEY

The work discussed in this thesis is related to the increase in aerodynamic performance of a small to medium classed, high aspect ratio, high endurance unmanned aerial vehicle. This type of UAV, as discussed in section 1.4.15 paragraph 4, is designed to deliver surveillance and tactical intelligence in commercial and civil operational platforms.

The research discussed in this chapter has been done on similar platforms to achieve the same goal. Wing morphing is the common answer to achieving this goal. In section 1.4.2, Johnston el al proclaims that wing morphing can allow for less energy requirements than conventional vehicles that use conventional seamless control systems. The less energy spent, the higher the endurance. This lays down enough reason for the topic of wing morphing to be further researched.

The most important and defining characteristic of the commercial and civil type UAV is its high endurance capability. This is usually coupled with poor manoeuvrability, because of the high aspect ratio. Wing morphing is also a solution to this conundrum. The variable aspect ratio or span morphing wing discussed in section 1.4.3 is testament to this. The increase in manoeuvrability and performance, i.e. decrease in drag and increase in endurance, for such aircraft platforms are the aims in research conducted by researches such as Blondeau, Poonsong, Dr Lazos, Manzo, Lind et al, Pendleton et al, Gano, Renaud, Burkett, Good and Vishwanathan; who's works are all discussed above.

This thesis presents research work that could reduce power usage during takeoff and climb flight phases using wing morphing methods. This will allow more energy usage during the aircrafts operational flight phase, thus increasing the overall range and endurance of the aircraft. This work will greatly improve performance of the CPUT Adaptronics AMTL Technology Demonstrator. This work thus falls in well with contributions made by the above mentioned authors.

CHAPTER 2

In this chapter the details of takeoff and climb are discussed. This is followed by a discussion on the current high lift devices used on the CPUT UAV Technology Demonstrator and on the proposed variable angle of incidence high lift method. A description of the analysis process is then given where by the CAD models and the developed protocol for the analyses are discussed. The finite volume CFD package, EFD.Lab is mentioned and the analysis inputs for the takeoff and climb analyses are then discussed.

2.1 TAKEOFF

The ground roll (S_g), as shown in figure 2.1, is the distance taken for the aircraft to go from zero velocity to lift off velocity (V_{LO}). The length of which is determined by the aircrafts ability to reach its specific lift off velocity (V_{LO}), which is usually $1.2V_{stall}$. If V_{stall} decreases, then S_g would decrease. This would allow for less time during ground roll and less power expenditure during takeoff.

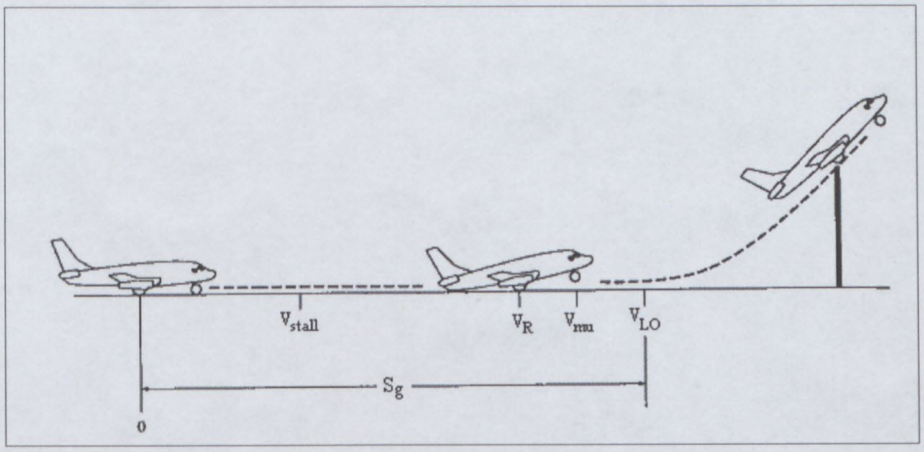

Figure 2.1: Critical takeoff velocities and ground roll for an aircraft during takeoff. (J.D. Anderson, 1999)

Therefore, a shorter S_g during takeoff would improve the performance and flight characteristics of the CPUT Adaptronics AMTL Technology Demonstrator.

The following is an equation to determine the ground roll,

$$S_g = \frac{(V_{LO}^2)(W/g)}{2\{T - [D+R]_{av}\}} \qquad \text{(J.D. Anderson, 2008)} \qquad (1)$$

where,

$$V_{LO} = 1.2V_{stall} = 1.2\sqrt{\frac{2W}{\rho_\infty S(CL)_{\max}}} \qquad \text{(J.D. Anderson, 2008)} \qquad (2)$$

Therefore substituting equation (2) into equation (1) we get,

$$S_g = \frac{1.44W^2}{g\rho_\infty S(CL)_{\max}\{T - [D+R]_{av}\}} \qquad \text{(J.D. Anderson, 1999)} \qquad (3)$$

Where W is the weight, S is the wing surface area, $(CL)_{max}$ is the maximum lift coefficient during ground roll and T, D and R are the thrust, drag and rolling friction respectively.

To illustrate some important physical and design parameters of takeoff, an assumption, that D and R are much smaller than T and therefore can be ignored, is made (J.D. Anderson, 2008). For simplicity, equation (4) thus offers a reasonable approximated expression for determining S_g, (J.D. Anderson, 2008)

$$S_g \approx \frac{1.44(W/S)}{g\rho_\infty (CL)_{\max}(T/W)} \qquad \text{(J.D. Anderson, 1999)} \qquad (4)$$

The design parameters that are important for ground roll during takeoff, clearly illustrated in equation (4), are wing loading (W/S), the maximum lift during takeoff ($(CL)_{max}$) which is limited by the tail clearance from the ground, and thrust-to-weight ratio (T/W).

From equation (4) we note that S_g decreases as W/S decreases and as T/W and $(C_L)_{max}$ are increased. As W, T and S are fixed in the design of the Technology demonstrator, we look towards $(C_L)_{max}$ for optimization. Notice that an increase in $(C_L)_{max}$ will decrease S_g and V_{LO}.

An increase in the overall lift generation during the ground roll would increase the value of $(C_L)_{max}$ during takeoff. However, a high amount of drag attributed to the increase in lift would severely degrade the takeoff conditions. An increase in drag would account for more power usage of the aircraft's engine and increase S_g. The power required for an unaccelerated flight phase is given as

$$P_r = \sqrt{\frac{2W^3 C_D^2}{\rho_\infty S C_L^3}} \propto \frac{1}{C_L^{3/2}/C_D} \qquad \text{(J.D. Anderson, 2008)} \qquad (5)$$

The bar graphs in figure 2.2 compare the relative percentages of different components of drag for a typical subsonic aircraft. The wing, body, empennage, engine installation, interference, leaks, undercarriage and flaps contribute to the drag that stems from friction and pressure drag due to flow separation. This is the zero-lift parasite drag and constitutes for most of the drag during cruise conditions.

Drag due to lift, also known as lift-dependent drag, constitutes for the majority of the drag during takeoff and climb conditions. This element of drag stems from the induced drag and the increase in parasite drag due to the increase of the angle of attack from the zero lift. Induced drag accounts for most of the drag due to lift in these conditions due to its high lift coefficient during takeoff and climb.

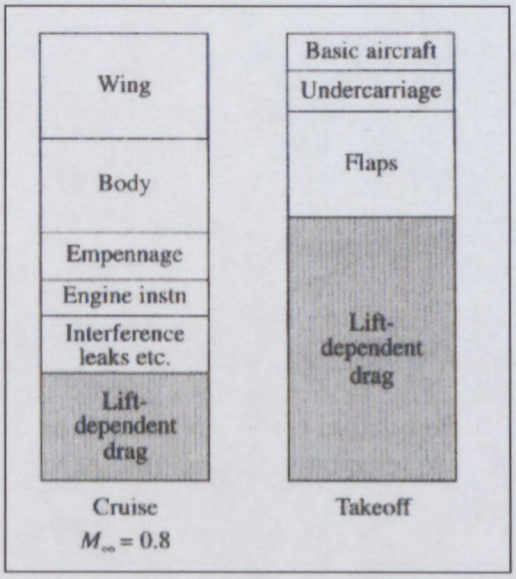

Figure 2.2: Comparison of cruise and takeoff drag for generic subsonic transport. (J.D. Anderson, 2007)

We observe the equation for drag

$$D = \frac{1}{2}\rho_\infty V_\infty^2 S C_D \qquad \text{(J.D. Anderson, 2008)} \qquad (6)$$

and the conventional drag polar equation for an aircraft,

$$C_D = C_{D,0} + K C_L^{\ 2} \qquad \text{(J.D. Anderson, 2008)} \qquad (7)$$

where C_D is the total drag coefficient, $C_{D,0}$ is the zero-lift parasite drag coefficient, and KC_L^2 is the drag due to lift.

During the ground roll the induced drag is reduced due to the proximity of the wings to the ground thus inhibiting the effect of downwash. This is known as the ground effect.

Hence, the coefficient of drag for ground roll (equation (7)) becomes

$$C_D = C_{D,0} + (k_1 + Gk_3)C_L^2 \qquad \text{(J.D. Anderson, 2008)} \qquad (8)$$

where

$$G = \frac{(16h/b)^2}{1+(16h/b)^2} \qquad \text{(J.D. Anderson, 2008)} \qquad (9)$$

h is the height above the ground and b is the wingspan.

Observing equation (6), the total drag (D) is reduced by reducing C_D and/or V_∞, this in turn reduces S_g.

2.2 CLIMB

We consider steady climb along a straight inclined path, with a zero bank angle and assuming the thrust line is in the direction of flight as shown in figure 2.3.

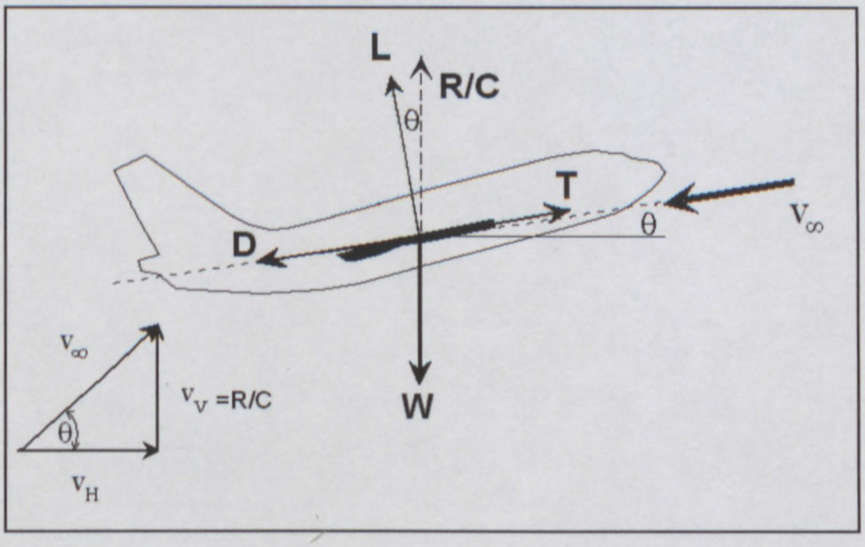

Figure 2.3: Velocity and force vectors in climbing flight. (J.D. Anderson, 2008)

The rate of climb (R/C) is a performance parameter used to judge the aircrafts ability to ascend. R/C increases as the power required to climb ($P_r = DV_\infty$) decreases.

Therefore, a decrease in the power required to climb will improve the performance and flight characteristics of the CPUT Technology demonstrator.

The CPUT Technology Demonstrator is a small UAV with a wingspan of about 2.5m and has a climb angle (θ) of less than 15 degrees. The small climb angle allows the assumption that $L = W$. In cases where the climb angle is 20 degrees and above, L is usually smaller than W. T supports a component of the weight, which in this case is small and neglible. (Fillipone, 2006; J.D. Anderson, 2008)

With the above assumptions in mind we can calculate the R/C from:

$$R/C = \frac{TV_\infty - DV_\infty}{W} = \frac{TV_\infty}{W} - \frac{C_D}{C_L^{3/2}}\sqrt{\frac{2}{\rho_\infty}\frac{W}{S}} \quad \text{(Fillipone, 2006)} \qquad (10)$$

Where,

$TV_\infty - DV_\infty = excess\ power$ (Fillipone, 2006; J.D. Anderson, 2008) (11)

As stated above; T, W and S are fixed in design of the Technology demonstrator. Therefore we look towards $C_L^{3/2}/C_D$ for optimization.

We can see from equation (10) that,

$$P_r \propto \frac{1}{C_L^{3/2}/C_D} \qquad \text{(Fillipone,2006)} \qquad (12)$$

Therefore, a maximum value for $C_L^{3/2}/C_D$ corresponds to a minimum power requirement and a maximum R/C.

Equation (10) can be rewritten as

$$R/C = \frac{TV_\infty}{W} - V_\infty\left[\frac{1}{2}\rho_\infty V_\infty^{\,2}\left(\frac{W}{S}\right)^{-1}C_{D,0} + \frac{1}{2}\rho_\infty V_\infty^{\,2}\left(\frac{W}{S}\right)^{-1}KC_L^{\,2}\right] \quad \text{(J.D. Anderson, 1999)} \qquad (13)$$

where the zero lift parasite drag and drag due to lift are clearly illustrated in the two terms inside the brackets. As the power available (TV_∞) is a fixed design parameter

for the aircraft, a decrease in these two elements of drag would decrease the P_r and thus increase *R/C.*

Induced drag constitutes for most of the drag due to lift, while drag due to lift constitutes for most of the total drag during climb. Induced drag occurs when the effective angle of attack of the local flow in the vicinity of the wing is lessened due to an induced angle of attack brought about by the effect of downwash as represented in figure 2.4. This reduces the effective lift and increases V_{stall}. (J.D. Anderson, 2007)

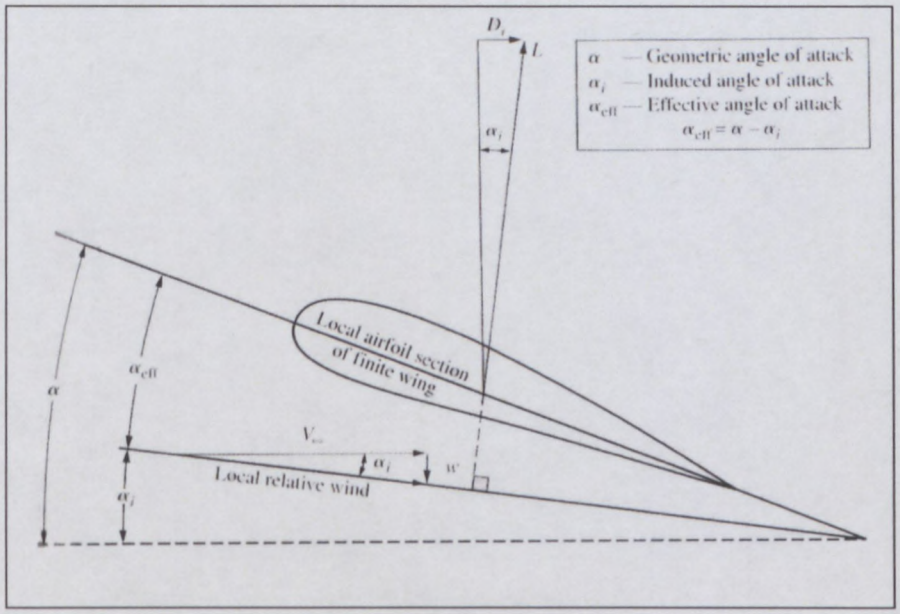

Figure 2.4: The effect of downwash on the local flow of an airfoil section of a finite wing. (J.D. Anderson, 2007)

Slightly reducing the angle of attack of the wing itself during climb could lessen the downwash effect, therefore decreasing the induced drag and the drag due to change in angle of attack from zero lift, thus decreasing the drag due to lift and increasing *R/C.*

2.3 HIGH LIFT DEVICES

2.3.1 Plain flap

Plain trailing edge flaps are used on the CPUT Technology Demonstrator and are formed by hinging the trailing edge part of the wing section about a point as shown in figure 2.5. (Abbot & Doenhoff, 1959) These flaps also serve as ailerons. Abbot and Doenhoff suggest that for effective use as a high lift device the flap deflection should not exceed 10 to 15 degrees. (Abbot & Doenhoff, 1959)

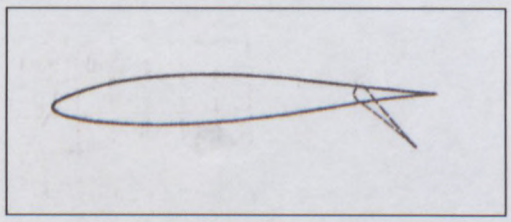

Figure 2.5: Plain flap or aileron (Abbot & Doenhoff, 1959)

High lift devices such as plain flaps increase the lift experienced by the wing by effectively increasing the camber. In a sense one could say that this virtually increases the angle of attack of the airfoil section and thus lift is increased, as illustrated in figure 2.6. (J.D. Anderson, 2008)

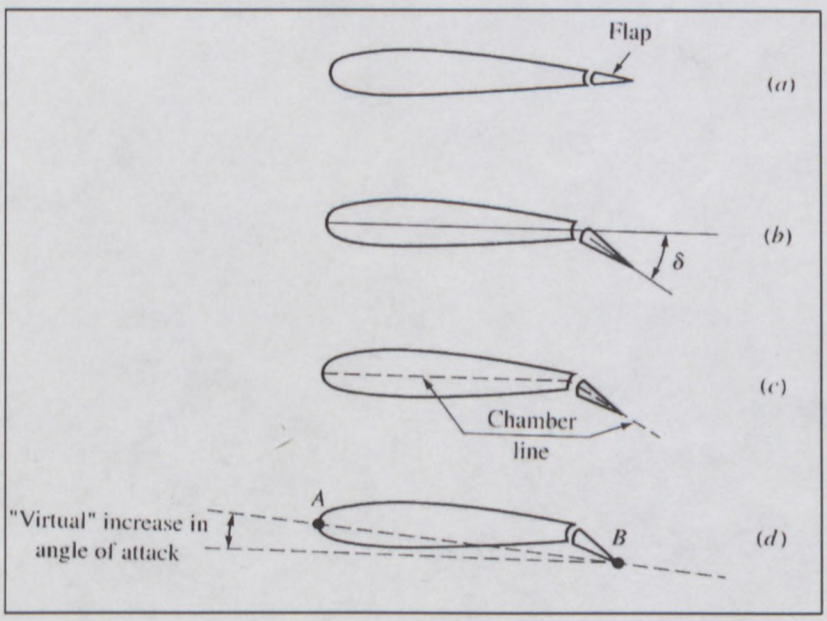

Figure 2.6: Effective increase in camber and virtual increase in angle of attack causes the increase in lift. (J.D. Anderson, 2008)

Flaps however are not seamless and therefore cause discontinuities in the wing surface which leads to parasitic drag. A positive flap deflection, giving it the ability of

a high lift device, allows the flow over the flap to separate thus causing large amounts of drag and degrading the flight conditions. (Abbot & Doenhoff)

2.3.2 Seamless variable angle of incidence wing

A variable angle of incidence morphing wing has the ability to seamlessly change the angle of incidence of the wing while at any orientation, either increasing or decreasing the amount of lift experienced on the wing by either increasing or decreasing the angle of incidence of the wing. The wing surface is seamless and the actuation of the wing as a control surface allows little adverse gradients in geometry, therefore less drag is experienced.

The sVAI wing has the ability to increase or decrease its geometrical angle of attack during takeoff and climb to increase the maximum lift experienced during ground roll or decrease the drag during climb.

2.4 ANALYSIS

Working CAD models for the sVAI wing concept and Conventional wing (which is currently being used on the Technology Demonstrator) were developed. These models were analyzed using numerical software and the results compared to determine which wing has superior flight characteristics during the takeoff and climbing flight phases.

The analyses intend to show an increase in aircraft performance from the sVAI system, as compared to the Conventional control surface system. This chapter begins with the development of the working CAD models, Analyses protocol and ends with Analyses input.

2.4.1 Working CAD models

CAD models of the sVAI concept wing and conventional wing were developed on the CAD software package Solidworks® to numerically analyze and compare aerodynamic performances of the wings. The conventional wing was designed along with the entire Technology Demonstrator model during the developmental stages of the aircraft. The sVAI wing is a modification of the conventional wing, where a flexing section was introduced to the model

2.4.1.1 The Conventional (CON) wing

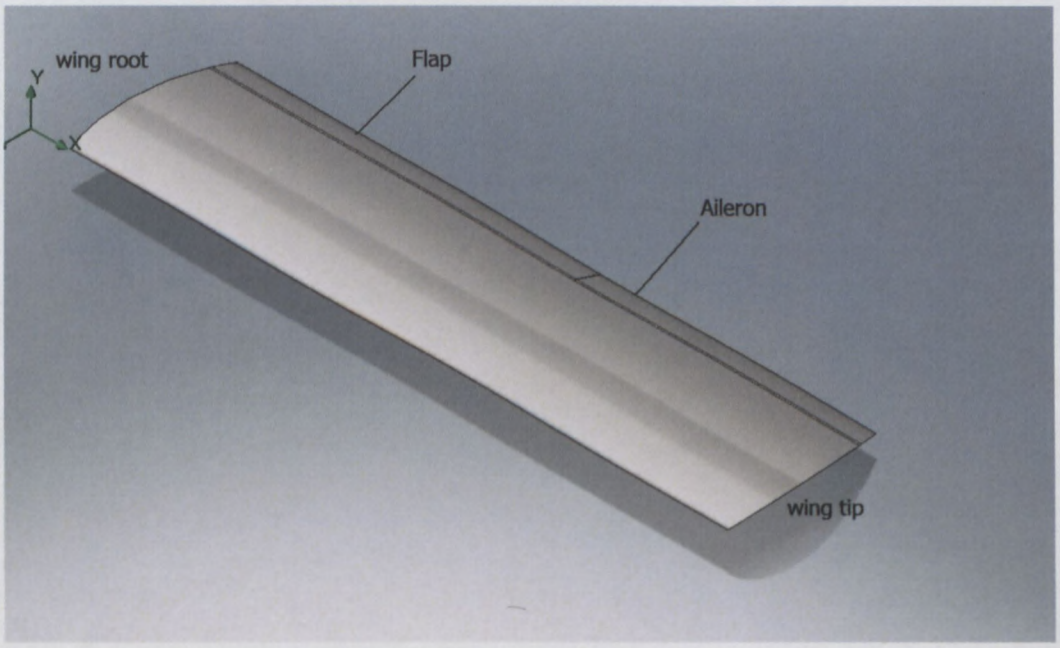

Figure 2.7: Conventional wing

The conventional (CON) wing, as seen in figure 2.7, has a length 1.215m and a chord of 0.296m. The Technology Demonstrator has an aspect ratio (*AR*) of 8, a wingspan (*b*) of 2.43m and a wing area (*S*) of 0.72m^2. The airfoil profile of the wing is an Ah79100b profile.

The wing is equipped with an aileron and plain flap that can be deployed simultaneously for maximum effectiveness (see figure 2.7). The act of deploying these control surfaces is referred to as "flap" throughout this thesis.

2.4.1.2 The Seamless Variable Angle of Incidence (sVAI) wing

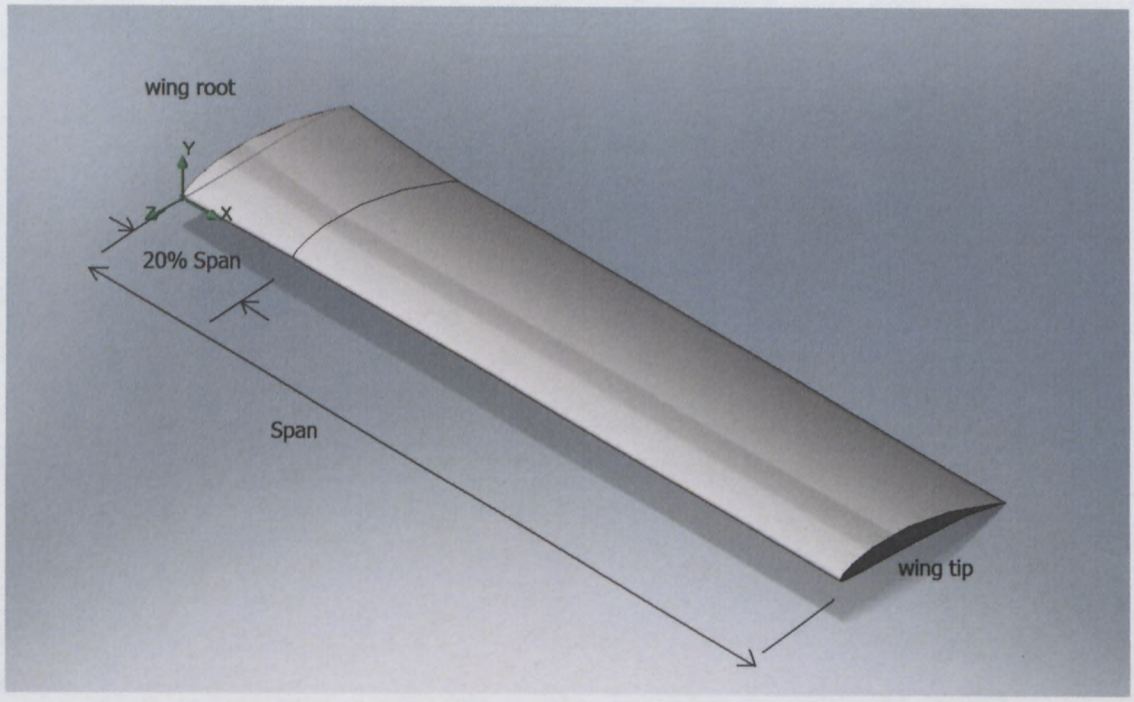

Figure 2.8: The sVAI wing concept

The sVAI wing, as seen in figure 2.8, has the same dimensions and profile as the conventional wing. The flap and aileron have been removed and a flexible section of about 20% of the span has been introduced at the wing root end. A length of 20% of the wing was chosen for this first prototype for reasons of ease of manufacturing and structural integrity. Further studies need to be done on the aerodynamics and structural strength for different size flexible sections.

The flexible section of the wing was modeled using the loft feature tool available in the CAD package. The loft function adds virtual material between two or more profiles. By creating a loft between two wing profiles that are at different angles to each other and a finite distance apart, one creates a solid body that changes its geometrical angle of attack at each plane from the first profile to the last creating a twist as it extrudes. This is shown below in figure 2.9.

The act of increasing or decreasing the angle of incidence of the sVAI is referred to as "twisting" throughout this research.

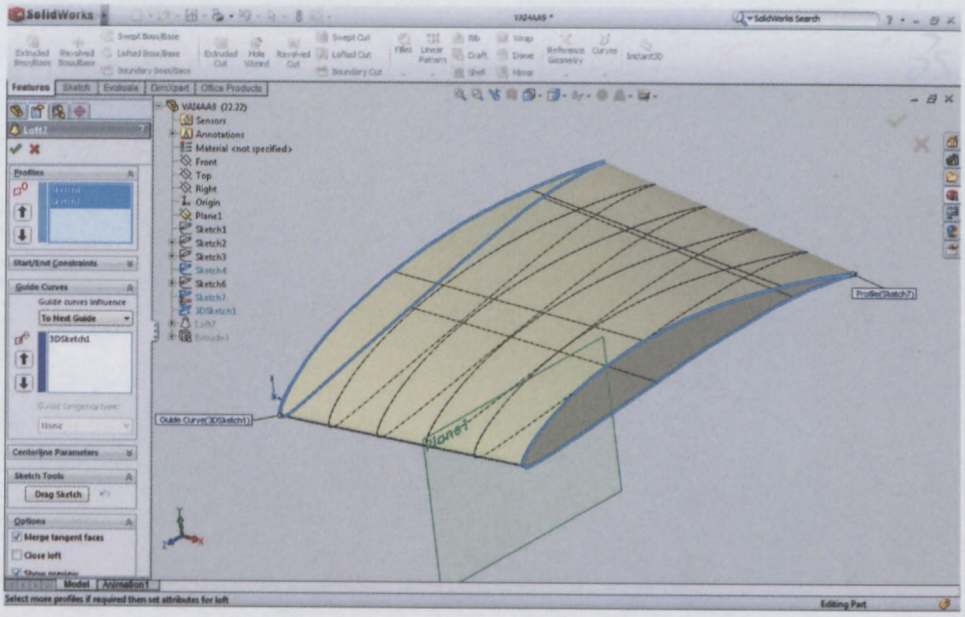

Figure 2.9: A snapshot of the development of the twisting section for the CAD model in Solidworks®.

2.4.2 Analyses Protocol

The aerodynamic performances of the two wings are compared through the simulated flight phases of takeoff and climb.

2.4.2.1 Takeoff phase of flight

A takeoff simulation protocol was developed to predict the amount of lift that is and could be generated by the CON and sVAI wing in different configurations while on level ground. The CON wing has a maximum flap deflection of 15° and the sVAI wing has a maximum twist of 8°. The 8° max twist was decided upon because the stall angle of the airfoil section (ah79100b) used for Technology Demonstrator is ±18°, and the climb angle is around 8° (angle of attack = 5° + incidence angle = 3°), which is the maximum angle of attack to be used by the vehicle during any phase of flight.

A benchmark was set with analyses run of the CON wing without any use of its control surfaces. The wing was set at an angle of incidence of 3°, as it is on the actual CPUT Technology Demonstrator at a 0° angle of attack (α). The maximum α

allowed by the tail clearance of the Technology demonstrator during the rotational phase in takeoff is 5°.

V_{stall} is obtained for the CON wing at α = 0°. $V_{LO} = 1.2V_{stall}$. V_{LO} is then applied to the wing at α = 0° to obtain a value for $(CL)_{max}$ and drag (D).

The same analysis protocol was run on the CON wing with flap deflection ranging up to the maximum deflection of 15°. The protocol was run on the sVAI wing this time with a twist deflection ranging up to 8°. Values for V_{stall}, V_{LO}, $(CL)_{max}$ and D are obtained for each configuration.

The values of $(CL)_{max}$ and D are then used in equation (3) (repeated below) to determine the ground roll (S_g) of each configuration.

$$S_g = \frac{1.44W^2}{g\rho_\infty S(CL)_{\max}\{T - [D+R]_{av}\}} \qquad (3)$$

ρ_∞ was taken at sea-level, T is the actual thrust available from the Technology demonstrator's power plant, and $R = \mu_r(W - L)$

An increase in $(CL)_{max}$ was predicted as the flap and twist angles increase, however an increase in drag was also predicted. The value for $C_L^{3/2}/C_D$ for each configuration was obtained to determine the power usage.

The performance results of each wing configuration were then compared against each other to obtain the most efficient configuration for takeoff.

2.4.2.2 Climb phase of flight

A climb simulation protocol was constructed to predict the rate of climb performance of the CON and sVAI wings in different configurations during climb phase orientation. The assumption was made that the CON wing has a maximum positive flap deflection of 20° and maximum negative flap deflection of -5°, and the sVAI wing has a maximum positive twist of 8° and a maximum negative twist of -5°.

A benchmark was set with analyses run of the CON wing without any use of its control surfaces. The CPUT Technology Demonstrator climbs at full throttle and an assumption that V_{climb} falls in the range between 16.667m/s and 33.33m/s was made. Values of lift (L) vs angle of attack (α) at V_{climb} were obtained and plotted. The $C_L^{3/2}/C_D$ values at V_{climb} were obtained and plotted against α. The α relating to the value for $C_L^{3/2}/C_{D,max}$, i.e. α_{climb}, was obtained.

The same protocol was run on the CON wing with flap deflections ranging from max negative to max positive and the sVAI wing with twist deflection ranging from max negative to max positive. Values for $C_L^{3/2}/C_{D,max}$ and α_{climb} were obtained for each configuration.

The values for $C_L^{3/2}/C_{D,max}$ were then used in equation (10) (repeated below) to determine the maximum rate of climb (R/C_{max}) for each configuration. The quicker R/C is the more efficient the climb.

$$R/C = \frac{TV_{climb}}{W} - \frac{C_D}{C_L^{3/2}}\sqrt{\frac{2}{\rho_\infty}\frac{W}{S}} \qquad (10)$$

An increase in $C_L^{3/2}/C_{D,max}$ was predicted as the flap and twist angles decrease slightly past zero to decrease the drag due to lift. Too much negative flap or twist could retard the lift and increase drag, which may severely degrade flight conditions.

The performance results of each wing configuration were compared against each other to obtain the most efficient configuration for climb.

2.5 ENGINEERING FLUID DYNAMICS (EFD)

Computers these days play a major role in aircraft design. CAD embedded fluid flow simulation software have redefined the design process by allowing for effective design optimization with little cost and less time. (Anderson J.D, 1995)

Engineering Fluid Dynamics (EFD lab) is the computational fluid dynamics (CFD) package used in this research to run analyses. Figure 2.10 shows velocity profile and pressure plot images extracted from EFD during the design stages of the CPUT Technology Demonstrator. EFD was used to optimize the wing, tail and nosecone designs.

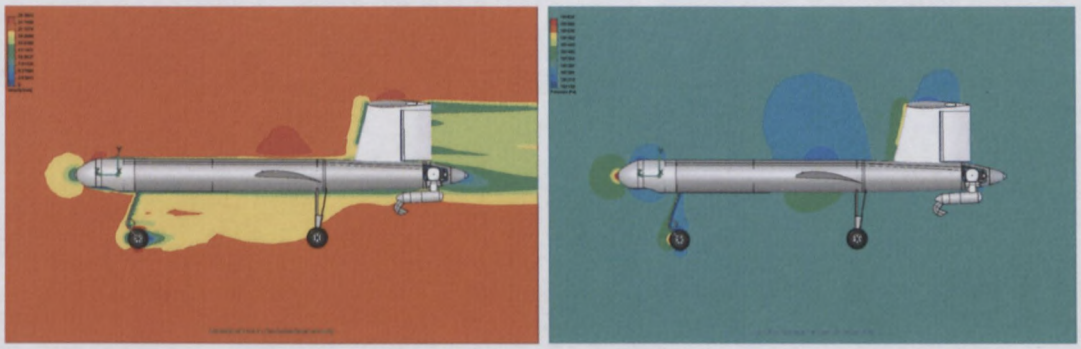

Figure 2.10: Velocity profile (left) and pressure plot (right) of the Technology Demonstator during its design phase.

CFD codes solve fluid flow problems by solving numerical algorithms. Commercial CFD packages include sophisticated user interfaces to make the inputting of parameters and the examining results easier. Therefore CFD packages contain three main elements i.e. pre-processor, solver and post processor. (Versteeg & Malalasekera, 2007)

Pre-processor inputs include:

- Definition of the computational domain.
- Generation of a mesh of control volumes.
- Selection of the physical and chemical phenomena to be modelled.
- Definition of fluid properties.
- Specifications of appropriate boundary conditions. (Versteeg and Malalasekera, 2007)

The accuracy of the output depends on the number of control volumes (cells) in a mesh. The number of cells depicts not only the accuracy, but also the calculation time and cost as well. Optimal meshes are therefore not uniform, allowing a finer mesh (more cells) where large variations in flow patterns occur, and a coarser mesh (less cells) where little to no variations occur. (Versteeg and Malalasekera, 2007)

The solver uses numerical methods to perform the following steps:

- Approximation of the unknown flow variables.
- Discretization of the approximations into the governing flow equations, followed by mathematical manipulations.
- Solution of algebraic equations. (Versteeg and Malalasekera, 2007)

Solvers use one of three distinct streams of numerical solution techniques i.e. finite difference, finite element and spectral methods (Versteeg & Malalasekera, 2007). EFD and other main commercially available code use the finite volume technique, which stems from the finite difference method. Versteeg and Malalasekera (2007) state that this technique is the "most well established and thoroughly validated general purpose CFD technique". (Versteeg and Malalasekera, 2007)

In the post-processing one is allowed to perform the following tasks:

- Domain geometry and grid display
- Vector plots
- 2D and 3D surface plots
- Flow trajectory plots
- Particle tracking
- Contour plotting. (Versteeg and Malalasekera, 2007)

The huge amount of developmental work on the post-processing in CFD packages have made it easier to do analyses and processing of results. Visualisation tools help on the education front as well as aid in new research topics.

EFD.Lab is a full-featured general purpose CAD-embedded finite volume fluid flow and heat transfer simulation tool that encompasses the following features:

- Rectangular adaptive meshing (manual or automatic refinement).
- Partial cells technology to accurately simulate near wall boundary conditions.
- Laminar, transitional and turbulent flow regimes, all automatically and within the same model.
- Turbulent flow modelled using the Favre-Averaged Navier-Stokes equation.
- Automatic convergence control

EFD was developed by Flomerics, who are world-leading developers of engineering simulation software and services for analysis of fluid flow, heat transfer and electromagnetic radiation. Flomerics' software is designed to be embedded deeply into the design process and used by mainstream design engineers, not just by analysis specialists.

2.5.1 Rectangular adaptive meshing

EFD calculations are performed in a rectangular parallelepiped-shaped computational domain whose boundaries are orthogonal to the axes of the Cartesian Global coordinate system. A computational mesh splits the computational domain with a set of planes orthogonal to the Cartesian Global Coordinate System's axes to form rectangular parallelepipeds called cells. The resulting mesh consists of cells of the following three types (shown in figure 2.11):

- Fluid cells are the cells located entirely in the fluid
- Solid cells are the cells located entirely in the solid
- Partial cells are the cells which are partly in the solid and partly in the fluid. For each partial cell the following information is kept: coordinates of intersections of the cell edges with the solid surface and normal to the solid surface within the cell.

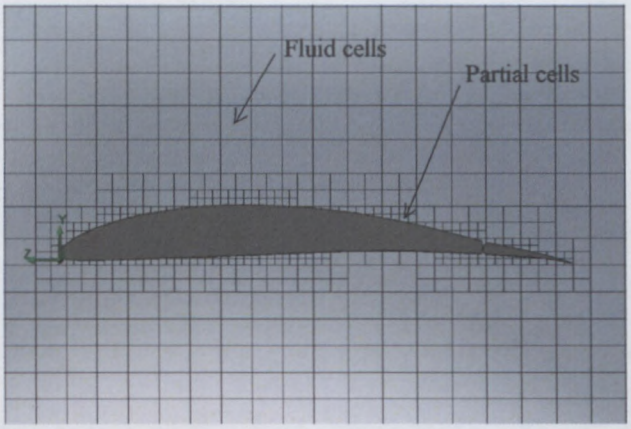

Figure 2.11: Mesh cell types.

The mesh is constructed in the following steps:

- Construction of basic mesh taking into account the control planes and respective values of cell number and cell size ratios.
- Resolving of the interface between substances, including refinement of the basic mesh at the solid/fluid and solid/solid boundaries to resolve the relatively small solid features and solid/solid interface, tolerance and curvature refinement of the mesh at a solid/fluid, solid/porous and fluid/porous boundaries to resolve the interface curvature.
- Narrow channels refinement, which is the refinement of the mesh in narrow channels taking into account the respective user-specified settings.
- Refinement of all fluid, and or solid, and or partial mesh cells up to the user-specified level.
- Mesh conservation. i.e. a set of control procedures, including check for the difference in area of cell facets common for the adjacent cells of different levels.

2.5.2 Favre-Averaged Navier-Stokes equations

EFD uses the Favre-Averaged Navier-Stokes equations to solve turbulent flow problems. The following is a derivation of these equations.

$$\frac{\partial \rho}{\partial t} + \frac{\partial}{\partial x_j}\left[\rho u_j\right] = 0 \tag{14}$$

$$\frac{\partial}{\partial t}\left[\rho u_i\right] + \frac{\partial}{\partial x_j}\left[\rho u_i u_j + p\delta ij - \tau_{ji}\right] = 0 \tag{15}$$

$$\frac{\partial}{\partial t}\left[\rho e_0\right] + \frac{\partial}{\partial x_j}\left[\rho u_j e_0 + u_j p + q_j - u_i \tau_{ij}\right] = 0 \tag{16}$$

(Anderson J.D, 1995 , CFD Online, 2005)

Above are the instantaneous equations for continuity, momentum and energy for a compressible fluid, respectively.

The viscous stress (for a Newtonian fluid and assuming Stokes law for mono-atomic gases), the heat flux (from Fourier's law) and the total energy are respectively defined by:

$$\tau_{ij} = 2\mu S_{ij}^{*} \tag{17}$$

$$q_j = -\lambda \frac{\partial T}{\partial x_j} \tag{18}$$

$$e_0 \equiv e + \frac{u_k u_k}{2} \tag{19}$$

(CFD Online, 2005)

In some engineering applications, for real cases, these instantaneous equations present very chaotic solutions for turbulent flow. Therefore averaging is introduced. (CFD Online, 2005)

Allowing z to be any dependent variable, one can define two types of averaging of z, namely:

- Reynolds averaging (classical time averaging)

$$\bar{z} \equiv \frac{1}{T}\int_{T} z(t)dt \tag{20}$$

$$z' \equiv z - \bar{z} \tag{21}$$

- Favre averaging (density weighted averaging)

$$\tilde{z} \equiv \frac{\overline{\rho z}}{\bar{\rho}} \quad \text{(CFD Online, 2005)} \tag{22}$$

$$z'' \equiv z - \tilde{z} \quad \text{(CFD Online, 2005)} \tag{23}$$

Note that $\overline{z'} = 0$, but $\overline{z''} \neq 0$ for the above equations. (CFD Online, 2005)

Therefore as stated on CFD Online (2005), by time-averaging the instantaneous equations one can obtain an average form of the governing equations, as shown below.

$$\frac{\partial \bar{\rho}}{\partial t} + \frac{\partial}{\partial x_j}\left[\overline{\rho}\tilde{u}_j\right] = 0 \tag{24}$$

$$\frac{\partial}{\partial t}\left[\overline{\rho}\tilde{u}_i\right] + \frac{\partial}{\partial x_j}\left[\overline{\rho}\tilde{u}_i\tilde{u}_j + \bar{p}\delta ij + \overline{\rho u_i'' u_j''} - \overline{\tau_{ji}}\right] = 0 \tag{25}$$

$$\frac{\partial}{\partial t}\left[\overline{\rho}\tilde{e}_0\right] + \frac{\partial}{\partial x_j}\left[\overline{\rho}\tilde{u}_j\tilde{e}_0 + \tilde{u}_j\bar{p} + \overline{u_j'' p} + \overline{\rho u_j'' e_0''} + \bar{q}_j - \overline{u_i \tau_{ij}}\right] = 0 \tag{26}$$

The density averaged total energy $\tilde{e}_0$ is defined by:

$$\tilde{e}_0 \equiv \tilde{e} + \frac{\tilde{u}_k\tilde{u}_k}{2} + k \tag{27}$$

k is given as the turbulent energy and is defined as:

$$k \equiv \frac{u_k'' u_k''}{2} \tag{28}$$

Equations 11, 12 and 13 are the Favre-averaged Navier-Stokes equations, with $\bar{\rho}$, $\bar{u}_i$ and $\tilde{e}_0$ being the primary solution variables. (CFD Online, 2005)

2.5.3 Experimental vs EFD

The following is a comparison, done by the author, between results obtained on EFD and results obtained through experiment to observe the accuracy of the EFD results.

NACA 4412

The NACA profile was put under analysis using the following parameters:

- Chord length – 1m

Reynolds number - 10^6

- Angle of attack – 13.5°
- Total number of mesh cells – 26 790.

Figure 2.12 shows the resultant velocity profile and figure 2.13 shows the EFD results versus the theory data of the NACA 4412 profile.

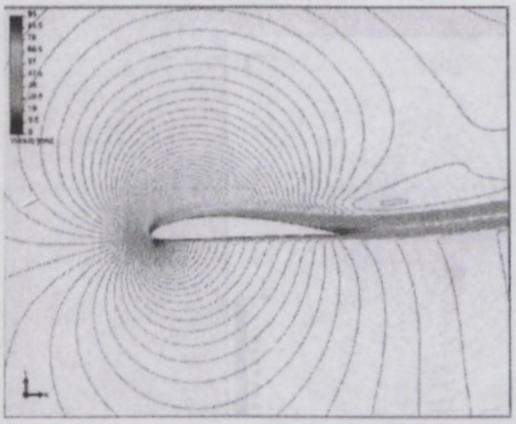

Figure 2.12: Velocity profile of the NACA 4412 airfoil

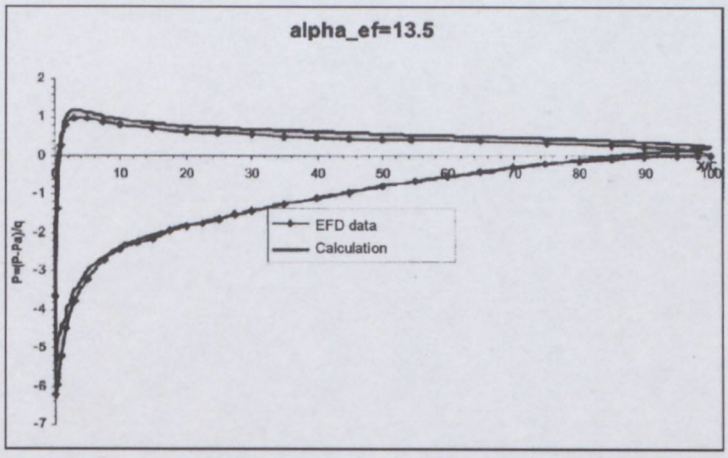

Figure 2.13: EFD data vs calculation theory of the pressure distribution of the NACA 4412 obtained from Esteq.

NACA 66 2 415

The NACA profile was put under analysis using the following parameters:

- Chord length – 1m

Reynolds number – 6×10^6

- Velocity – 89m/s
- Total number of mesh cells – +/- 40 000

Figure 2.14 shows the resultant pressure profile and figure 2.15 shows the EFD results versus the experimental data of the NACA 66 2 415 profile.

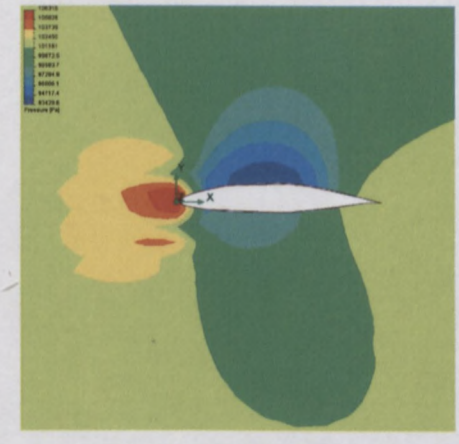

Figure 2.14: Pressure profile of the NACA 66 2 415

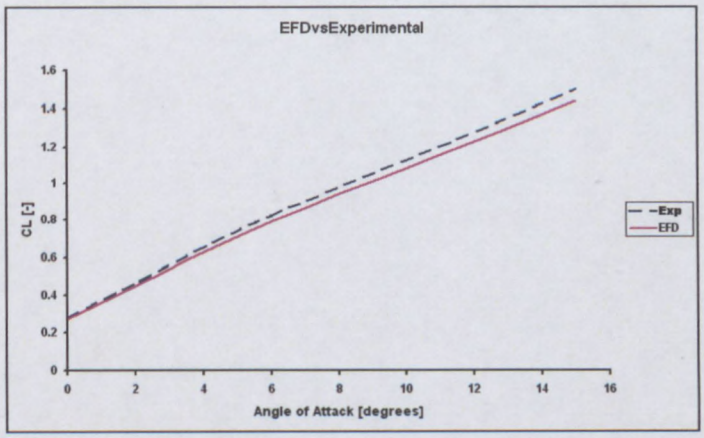

Figure 2.15: EFD data vs experimental data from Abbot and Doenhoff (1959) of the NACA 66 2 415.

The comparison showed that EFD produced accurate results that could be confidently used in the design process.

2.6 Analyses input

The following conditions were set for the analyses run on the CAD embedded finite volume CFD software package Engineering Fluid Dynamics (EFD.Lab).

a) Analysis type

An external flow case wa setup for each wing model as we're investigating the effects of flow over a body.

The flow was setup as a finite compressible flow regime.

Fluid - Air

Physical features

Heat conduction in solids: Off

No conjugate heat transfer problems considered.

Time dependent: Off

A default time step was automatically chosen by the program.

Gravitational effects: Off

Gravitational effects are ignored.

Flow type: Laminar and turbulent

The flow over the body was predicted to have laminar, transitional and turbulent flow regimes.

High Mach number flow: Off

The flow velocity does not reach Mach number in any of the analyses.

Humidity: Off

Relative humidity is ignored.

Default roughness: 0 micrometer

A smooth wall was chosen as default

Default wall conditions: Adiabatic wall

A heat insulated wall with a skin friction surface was chosen as default for the model.

Ambient conditions

Thermodynamic parameters Static Pressure: 101325 Pa

Temperature: 293.2 K

Ambient conditions at sea-level

Velocity parameters Velocity vector

Velocity in X direction: 0 m/s

Velocity in Y direction: 0 m/s

Velocity in Z direction: $-V_{\infty}$ m/s

Due to the models orientation the Global Z coordinate points in the opposite direction to the flow stream velocity.

Turbulence parameters Turbulence intensity and length

Intensity: 0.1 %

Length: 0.000875492637 m

EFD.Lab default turbulent parameter values were used as they are typical for wind tunnel testing.

Computational Domain

The minimum size for a computational domain for an external flow regime (as defined by Esteq) is:

1 x chord length from leading edge

2 x chord length from trailing edge

1 x chord length from the chord upwards and downwards respectively.

1 x chord length from the wing tip.

The origin for this specific model was set at (0.075, 0, 0) from the wing root, leading edge chord.

With this in mind the following dimensions were set for the computational domains:

X min	0.075 m
X max	1.5099999999 m
Y min	-0.512519807 m
Y max	0.578336244 m
Z min	-1.12615105 m
Z max	0.458940164 m

Figure 2.16 shows the size of the computational domain created.

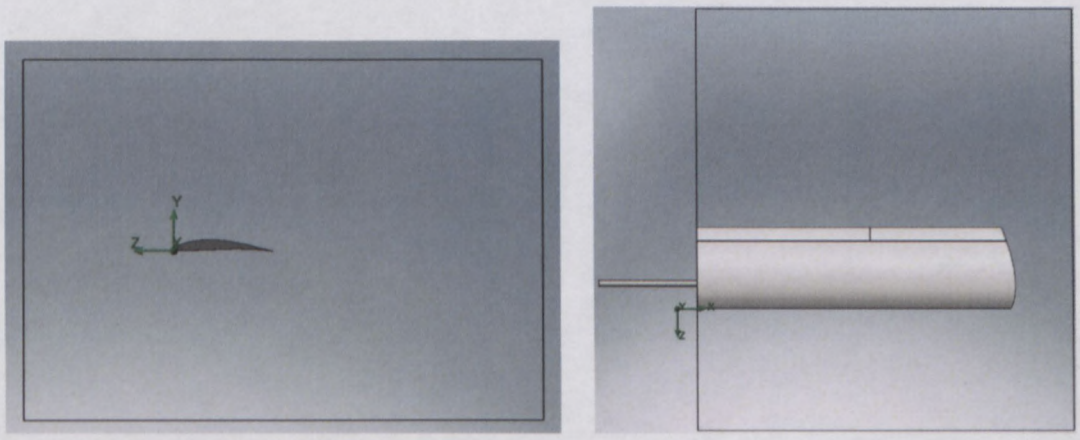

Figure 2.16: The computational domain seen in the right view (above left) and top view (above right).

Initial Mesh Settings

Automatic initial mesh: Off

Basic Mesh Dimensions

Number of cells in X	32
Number of cells in Y	40
Number of cells in Z	59

A mesh refinement of level 3 was set for the partial cells.

Figure 2.17 illustrates the basic mesh set up with partial cell refinement of level 3.

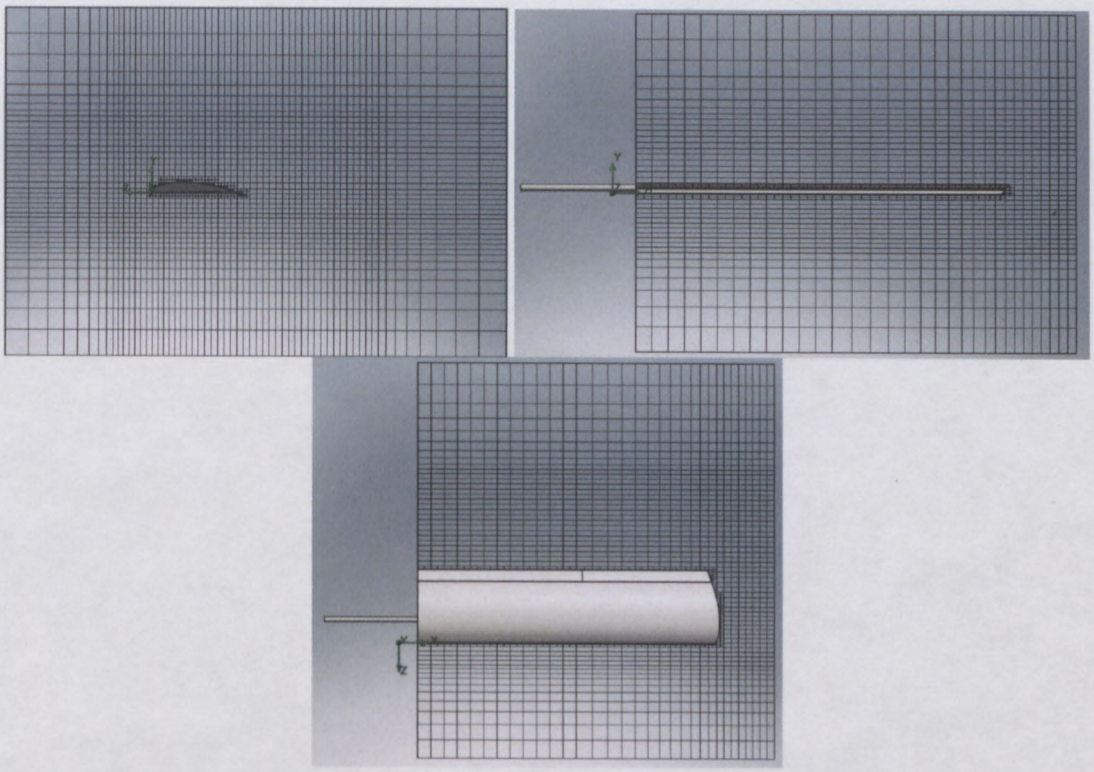

Figure 2.17: The right, front and top views of the initial mesh with level 2 partial cell refinement.

CHAPTER 3

In this chapter the results of the analyses are plotted, tabulated and discussed. The chapters in this section begin with the Results at Takeoff, followed by Climb.

3.1 RESULTS

Analyses were run on the CON and sVAI wings for takeoff and climb scenarios. Each wing was arranged at angles of attack ranging from 0° to 10°. The CON wing has a flap deflection ranging from -5° to 20°, while the sVAI wing has a twist deflection ranging from -5° to 8°. These deflections were applied at each angle of attack thus creating a range of wing configurations. For takeoff, the necessary wing configurations were run through a series of velocities ranging from 10m/s to 33.33m/s. For climb the necessary wing configurations were run through a series of velocities ranging from 16.667m/s to 33.33m/s.

The results of these can be found in Appendix I and are discussed below.

3.1.1 Takeoff

Figures 3.1 and 3.2 below illustrates plots of lift vs velocity for $\alpha = 0^{\circ}$ (with an incidence angle of 3°) for the CON and sVAI wing designs.

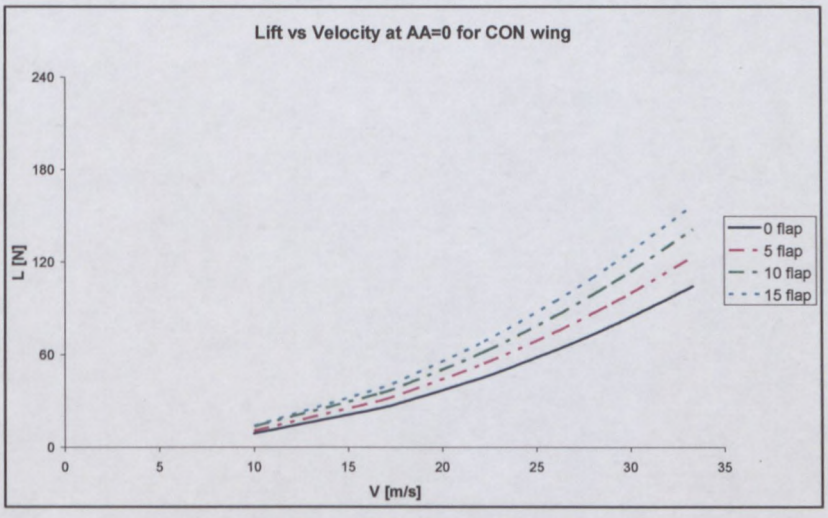

Figure 3.1: Lift vs velocity curves for angle of attack of 0 degrees for the CON wing.

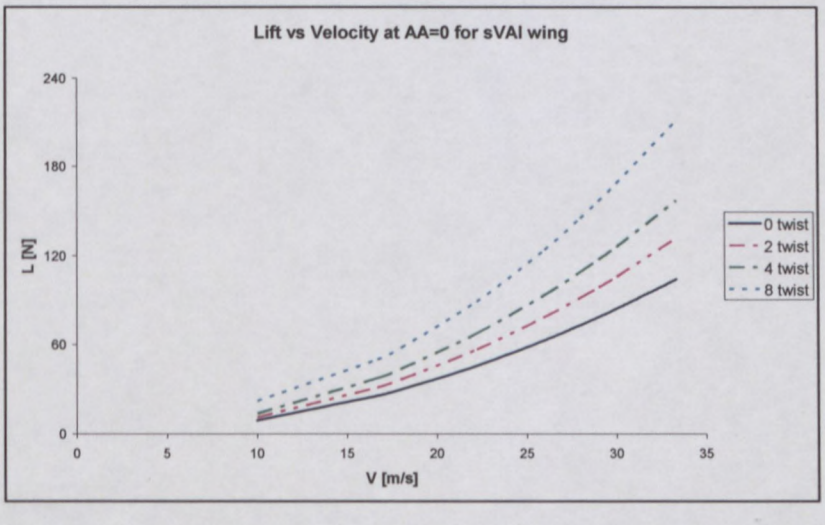

Figure 3.2: Lift vs velocity curves for angle of attack of 0 degrees for the sVAI wing.

The Gross Take Off Weight (GTOW) of the Technology Demonstrator is approximately 12kg. The amount of L on one wing of the Technology demonstrator to allow liftoff is therefore taken as 60N.

To obtain values for S_g equation (1) (repeated below) is used,

$$S_g = \frac{(V_{LO}^2)W}{2g\{T - [D+R]_{av}\}} \qquad (1)$$

where, T = 61N for the CPUT Technology Demonstrator, $R = \mu_r(W - L)$, and μ_r is the coefficient of rolling friction which is taken as 0.04 for a dry concrete surface (J.D. Anderson, 2008), the drag (D) is the total drag with ground effect included in the summation. Equation (9) for ground effect is repeated below,

$$G = \frac{(16h/b)^2}{1+(16h/b)^2} \tag{9}$$

where h and b are measured off the CPUT Technology Demonstrator and are 0.32m and 1.215m respectively.

Table 3.1 shows the results taken from the analyses shown in the above graphs. V_{stall} is found at $L \leq W$, $C_{L,(\max)} = 2W/\rho_\infty V_{stall}^2 S$ and V_{LO} = 1.2 V_{stall}.

Table 3.2 shows the values of the power usage ($C_L^{3/2}$ / C_D) of each wing configuration at V_{LO}, where α = 0° respectively. The higher $C_L^{3/2}$ / C_D is the less power is required for the flight phase. The values for P_r are obtained by using equation (5) (repeated below).

$$P_r = \sqrt{\frac{2W^3 C_D^2}{\rho_\infty S C_L^3}} \propto \frac{1}{C_L^{3/2}/C_D} \tag{5}$$

0° flaps/twist configuration is the standard takeoff configuration for the CON wing on the CPUT Technology Demonstrator.

	L (N)	V_{stall} (m/s)	Cl_{max}	V_{LO} (m/s)	S_g (m)
0 flaps/twist	60	25.39	0.43340512	30.468	54.2223
5 flaps (CON)	60	23.32	0.5131869	27.984	46.1237
10 flaps (CON)	60	21.88	0.58282592	26.256	41.21509
15 flaps (CON)	60	20.792	0.64649101	24.9504	37.98204
twist 2 (sVAI)	60	22.81	0.54207804	27.372	44.17628
twist 4 (sVAI)	60	20.981	0.63975702	25.1772	37.49989
twist 8 (sVAI)	60	18.32	0.83440197	21.984	29.77866

Table 3.1: Results for V_{stall} and V_{LO} at α = 0°

	$C_{L(max)}$	C_D	$C_L^{3/2} / C_D$	$P_r(W)$
0 flaps/twist	0.43340512	0.04847896	5.895406	169.4339
5 flaps (CON)	0.5131869	0.06003207	6.144495	162.5653
10 flaps (CON)	0.58282592	0.07336955	6.086917	164.1031
15 flaps (CON)	0.64649101	0.08890013	5.854151	170.628
twist 2 (sVAI)	0.54207804	0.06309466	6.247219	159.8922
twist 4 (sVAI)	0.63975702	0.07582774	6.67957	149.5428
twist 8 (sVAI)	0.83440197	0.11920608	6.382346	156.507

Table 3.2: Results for $C_L^{3/2} / C_D$ and Power required at $\alpha = 0^\circ$

For $\alpha = 0^\circ$, the sVAI wing at a maximum twist of 8° has a V_{stall} of 27.8% less than that of the 0° twist configuration. The S_g at 0° twist is reduced by 45% when maximum twist is applied. The $C_{L,(max)}$ of the 0° twist configuration is increased by 47.9% with maximum twist, but is coupled with an increase in drag of 59%, though the power required is reduced by 7.6%.

The CON wing with 0° flap has a decrease in V_{stall} of 18% when a maximum flap of 15° is applied. The maximum flaps produce a S_g distance of 30% less than that of 0° flap configuration. An increase in $C_{L,(max)}$ of 33% is coupled with an increase in drag of 45% for 0° flap when maximum flap is introduced, which also leads to 0.7% more power required.

The least power required for takeoff was obtained with the sVAI wing at 4° twist, with 11.7% less power required than that of 0° twist configuration. $C_{L,(max)}$, and C_D for 0° twist increase by 32% and 36%, and V_{stall} and S_g decrease by 17% and 31%, respectively when a 4° twist is applied.

Figure 3.3 shows pressure plots of the CON wing at 5° flap and the sVAI wing at 4° twist. 5° flaps produced the best results for the conventional wing configuration during the takeoff flight phase. It is clearly seen in figure 3.3 that the sVAI wing at 4° produces a lower pressure on the upper half and a higher pressure on the lower half of the wing section than the CON wing at 5° flap does. This is because of the actual increase in angle of attack of the wing, rather than the virtual increase of the angle of attack by increase in camber.

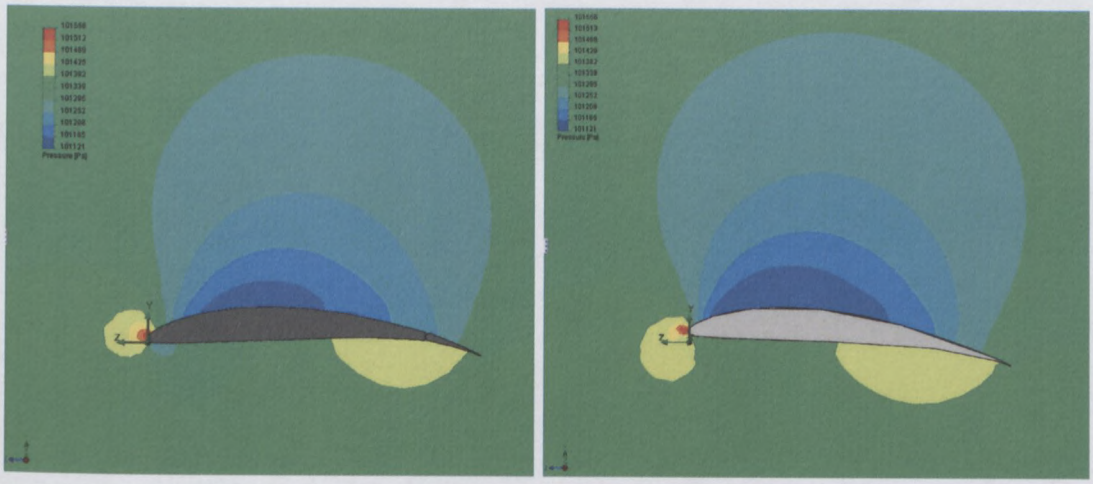

Figure 3.3: Pressure plot of CON wing with 5° flap (left) and sVAI wing with 4°twist (right).

3.1.2 Climb

α_{climb} (the climb angle) is found at maximum $C_L^{3/2}/C_D$. For the conventional wing at 0 deflection, α_{climb} was found at 8° (not considering any incidence angle) for different values of velocity ranging from 16.667m/s to 33.33m/s, as shown in figure 3.5. At α_{climb} = 8° flap and twist deflections are applied to see if any improvement in the flight performance can be achieved. The values for the rate of climb (R/C) were obtained using equation (10), repeated below,

$$R/C = \frac{TV_{climb}}{W} - \frac{C_D}{C_L^{3/2}}\sqrt{\frac{2}{\rho_\infty}\frac{W}{S}} \qquad (10)$$

where, T =50N, W=120N, ρ_∞ = 1.2kg/m^3, V_{climb} = 22.22m/s and S = 0.72m^2

The results show that introducing a flap and twist angle to the wing at α_{climb} = 8° reduces the drag when a negative deflection is applied. However, this also degrades the lift. This trend is seen for velocities ranging from 16.667m/s to 33.33m/s, as shown in Appendix I. It can also be seen in these results that the closer the negative flap or twist deflection is to the maximum negative the more the drag, and directly proportionately, the lift is reduced. Therefore, the results represented in table 3.3 and discussed below are for V_{climb} at 22.22m/s only, and at -2° flap and twist.

	CL	CD	$CL^{3/2}$ / CD	R/C (m/s)
0° Deflection	0.68	0.079	7.098004621	6.910255591
-2° Twist	0.59097	0.068	6.680948705	6.763677649
-2° Flap	0.63	0.073	6.849958874	6.825228701

Table 3.3: Results at α_{climb} for V_{climb} =22.22m/s.

The sVAI wing with a negative twist of 2° produces a CD that is ±14% less than that of the wing with 0° twist, as seen on figure 3.6. It also produces a CL that is ±13% less than at 0° twist, as seen on figure 3.7. The CON wing with a negative flap deflection of 2° produces a CD and CL of ±7.5% and ±7.3% less than 0° flap deflection as seen on figures 3.6 and 3.7, respectively. These produce $CL^{3/2}$/ CD values of ±3.5% and ±6% less than at 0° deflection for the CON wing with flap and the sVAI wing at twist, respectively. This is shown in figure 3.8. Therefore, the R/C of the wing at 0° flap/twist is ±2% and ±1.2% more than that of the wing at negative 2° twist and flap, respectively.

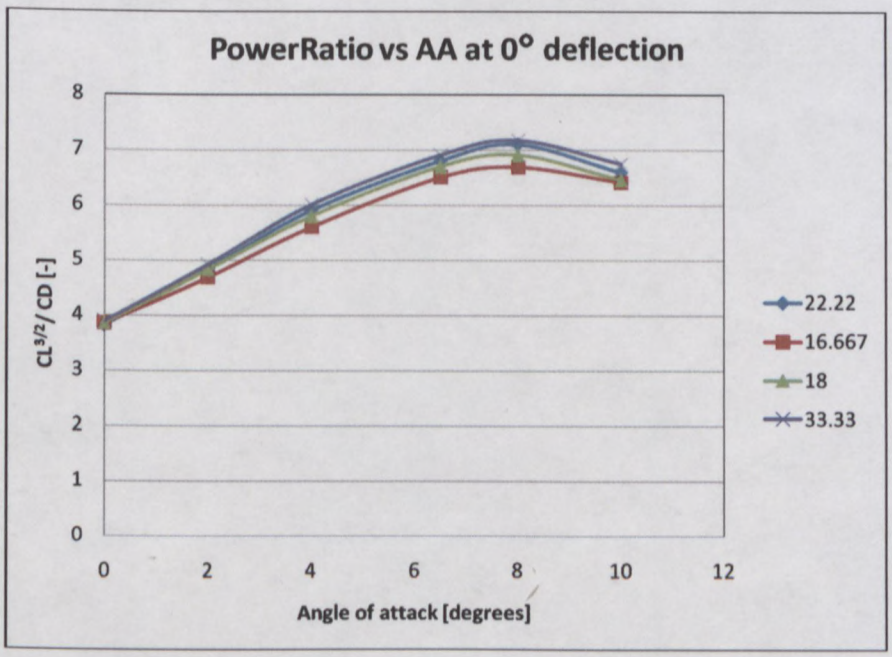

Figure 3.4: Power ratio vs angle of attack for different velocities

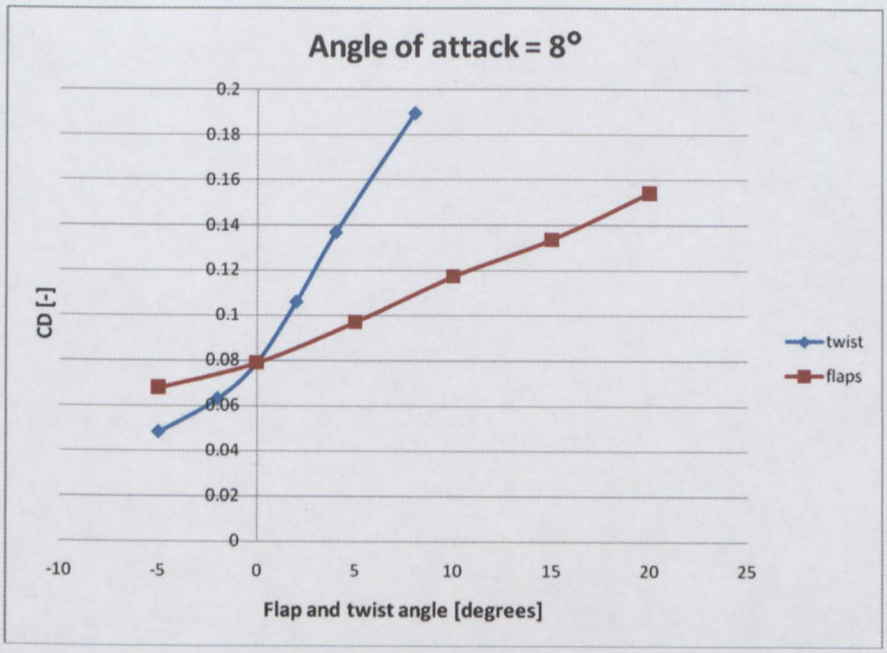

Figure 3.5: Drag vs deflection angle for 22.22m/s

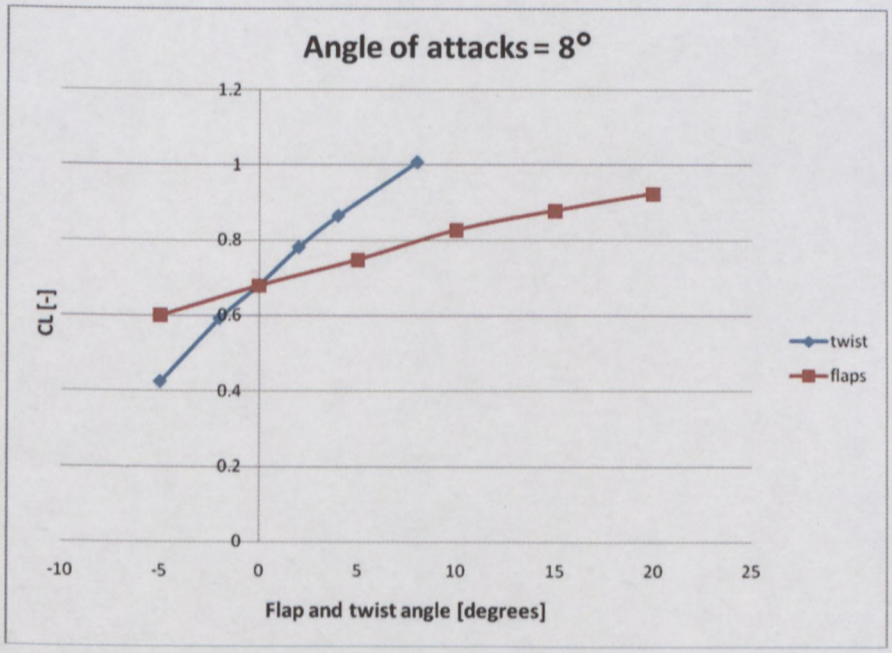

Figure 3.6: Lift vs deflection angle for 22.22m/s

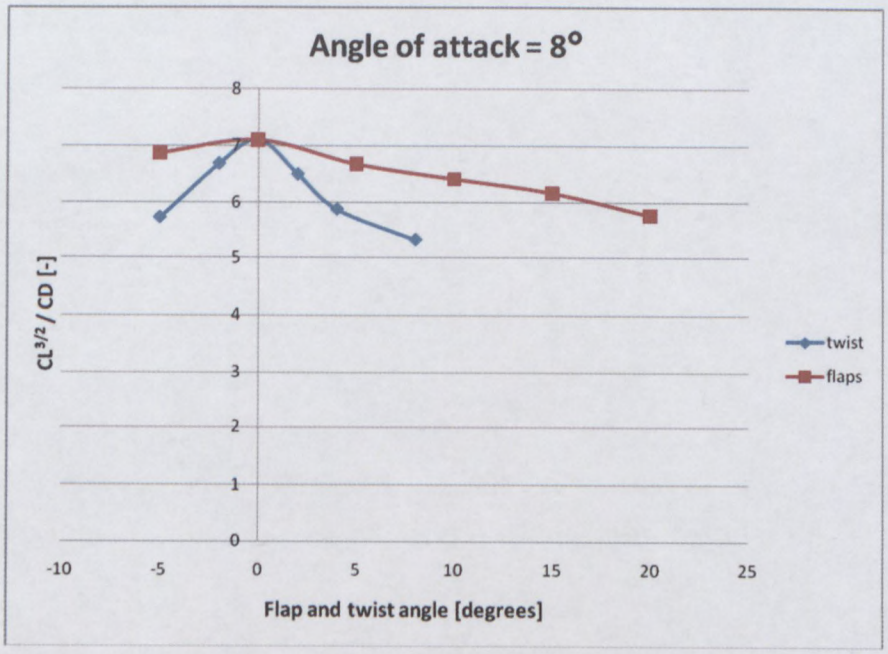

Figure 3.7: Power ratio vs deflection angle at 22.22m/s

3.1.3 Discussion of results

3.1.3.1 Takeoff

- During the takeoff flight phase protocol, the sVAI wing produced superior results to the conventional wing configuration.
- The sVAI wing at 4° twist produced the best results, while the CON wing at 5° flaps had the best results for the conventional configuration.
- The power required to lift off is reduced by ±12% when a 4° twist is applied to the wing, where as a 5° flap deflection reduces the power required by only ±4%.
- The velocity needed to lift off is reduced by ±17% with a 4° twist, as compared to a ±7% reduction by the CON wing with 5° flap, thus allowing for a quicker time to complete the takeoff phase.
- The ground roll distance for a conventional wing is reduced by ±31% when a 4° twist is applied, thus allowing less distance to lift off.

3.1.3.2 Climb

- During the climb flight phase protocol, the sVAI wing is able to reduce its drag by ±14% when applying a negative twist of 2°.
- Proportionally the lift is also reduced due to the decrease in angle of attack of the wing, thus reducing $CL^{3/2}/CD$ and in turn increasing the power required to climb. The climb performance is therefore not increased.

3.1.3.3 Endurance

The sVAI wing increases $CL^{3/2}/CD$ thus allowing for less ground roll, power and time required for lift off during the takeoff phase of flight than conventional wing configurations. An increase in $CL^{3/2}/CD$ also increases the endurance (E) as shown in equation 29 below.

$$E = \frac{\eta}{c_f}\frac{CL^{3/2}}{CD}\sqrt{2\rho_\infty S}\left(\frac{1}{\sqrt{W_1}} - \frac{1}{\sqrt{W_0}}\right) \qquad \text{(Blondeau, 2004)} \quad (29)$$

CHAPTER 4

In this chapter the manufacturing of the sVAI wing is discussed. A description of the design and manufacturing of the wing moulds, the wing, the flexible section and the fuselage test rig is given.

4.1 DESIGN AND MANUFACTURING OF THE sVAI WING

The sVAI wing concept design used in the CFD analyses of the wing was modeled using Solidworks®. The twisting section of the wing was modeled using the loft feature tool available in the CAD package as discussed in chapter 2. The twisting concept was developed and conceptualized so that a sVAI wing prototype could be manufactured.

One can envision a concept that consists of a discretized extruded finite body consisting of wing profile elements that have the ability to have different geometrical angles of attack respectively, thus creating a sense of wing deformation or morphing. Figure 4.1 shows the conceptualization of this vision, modeled in Solidworks®.

The detailed drawings for the prototype can be found in Appendix II.

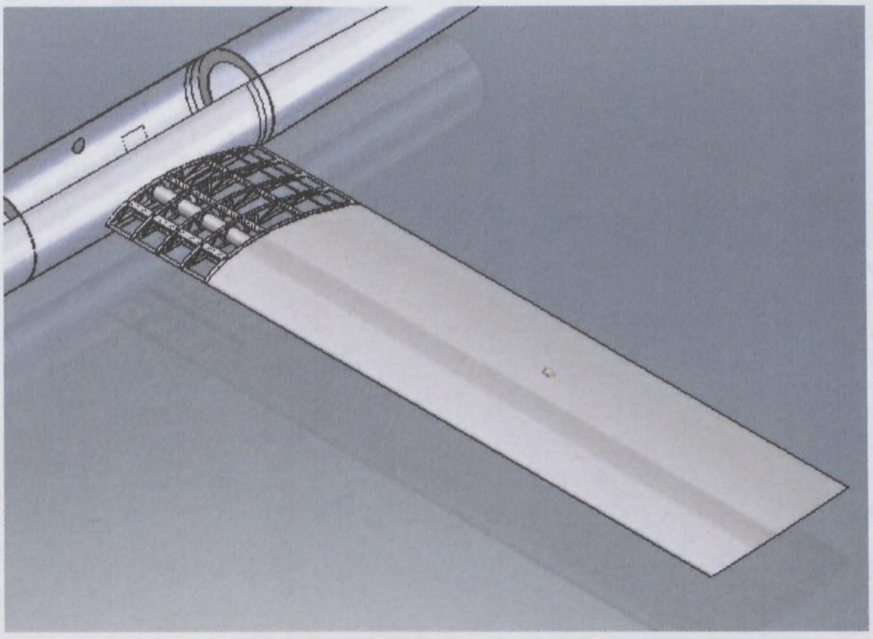

Figure 4.1: Design of sVAI wing to be manufactured.

The design consists of a series of wing profiles equispaced from each other, separated and supported by spacer beams. A flexible skin covers this system.

The prototype was developed and manufactured at the CPUT AMTL using only available manufacturing technologies at the CPUT Mechanical Engineering Department.

4.1.1 Wing mould manufacturing

A mould of the wing was designed and then grown using the three dimensional Zprinter 310 plus by Zcorp, shown in figure 4.2.

Figure 4.2: Zcorp 3D printer.

The first step in the main wing mould manufacturing process was making a three dimensional model of the wing shape as shown in figure 4.3. This was done using the 3D CAD design package, Solidworks.

Negatives of the upper and lower halves of the wing shape were designed as shown in figure 4.4. The mould model was then divided into 16 individual pieces (refer to figure 4.5) to be grown individually on the 3D printer, because of the maximum manufacturing size of 203 x 254 x 203 mm that printer allows. The individual mould piece designs were then refined, strengthened, excess material removed and fastener points located for assembly.

The mould designs were then saved as STL-(standard triangular language) files, which are used by software of the Zprinter.

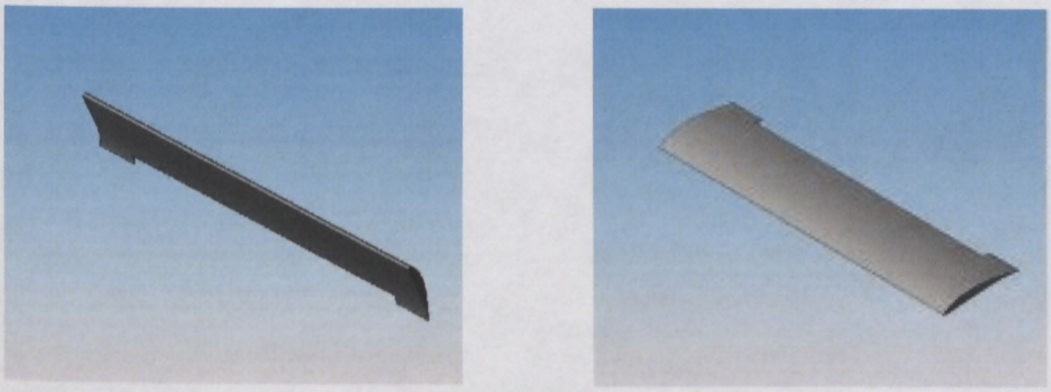

Figure 4.3: CAD models of the initial wing design.

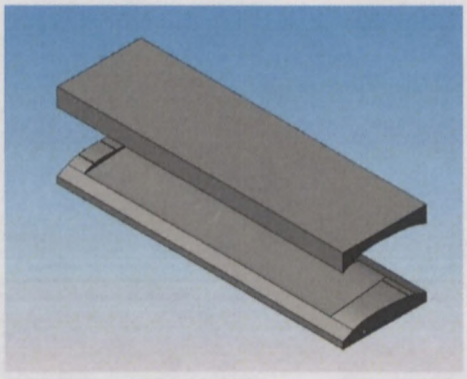

Figure 4.4: Wing negatives for mould design.

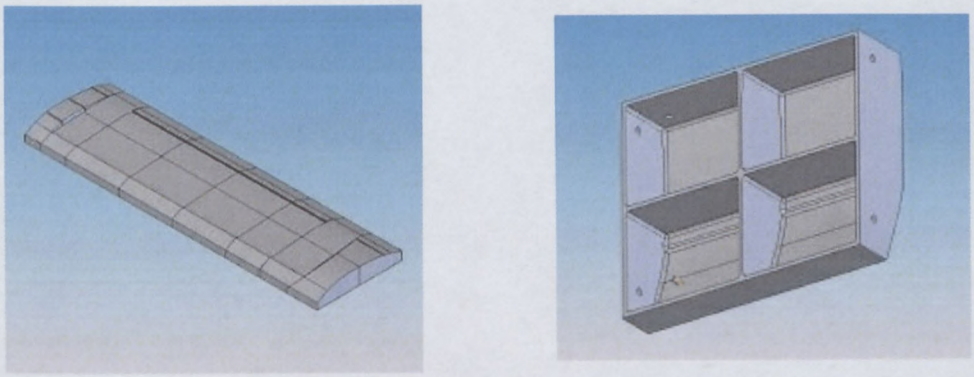

Figure 4.5: Wing mould divided into 16 pieces (left), one of the individual mould pieces (right).

Z Corp 3D Printers use a powder-binder technology invented at and patented by the Massachusetts Institute of Technology to create parts directly from digital data. First, the 3D Printer spreads a thin layer of powder called OZP130. Second, an ink-jet print head prints a binder called ZB58 in the cross-section of the part being created. Next, the build piston drops down, making room for the next layer, and the process is repeated. Once the part is finished, it is surrounded and supported by loose powder, which is then shaken loose. The materials used were all made by the Z Corporation ®.

Figure 4.6 shows the finished mould part just after printing. Excess powder is then removed in a vacuum chamber, and the part is placed in an oven to remove moisture.

Figure 4.6: Mould part removed from 3D printer.

The part was then dipped in cyano acrylade (superglue) to strengthen, and then put back in the oven to speed the curing process. After curing was complete the parts were assembled with nuts and bolts, and the mould then treated and finished to remove all irregularities and to allow for a smooth surface finish, as shown in figure 4.7.

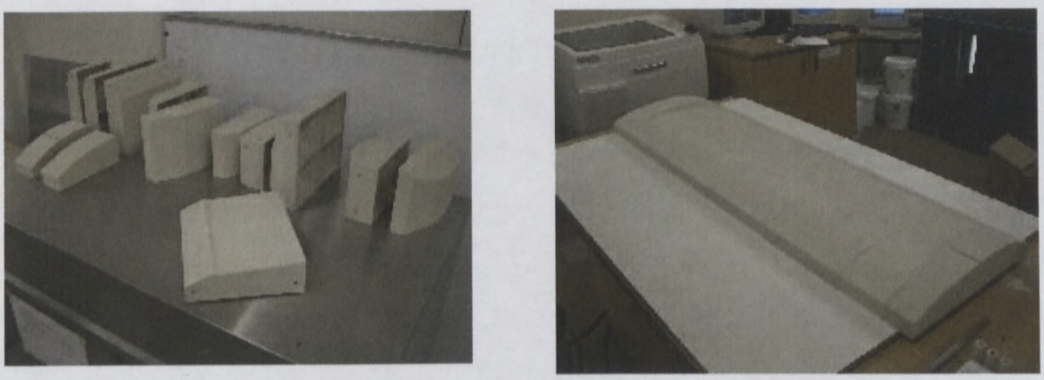

Figure 4.7: The completed mould parts (left), the assembled mould half (right).

4.1.2 Manufacturing of the wing

The wing was made by applying fibre glass and resin to the two mould halves and allowing the process to cure. A release agent was firstly applied to the moulds to allow the wing shells to be removed from the mould after curing takes place.

The wing was manufactured using three glass fibre layers that consist of one 2 ounce and two 4 ounce fibre glass layers, two strips of balsa wood and five carbon fibre ribbons.

The resin used for the layup process was AMT Epoxy resin AMPREG 22, which is mixed with AMT AMPREG 22 slow hardener to accelerate the curing process of the resin. A mixing ratio of 100:28 was used.

The three fibre glass layers were cut to fit the mould. The resin was then applied to the fibre glass layers one at a time using hand layup methods as shown in figure 4.8, making sure that there were no air bubbles during the process. The carbon fibre ribbons were then layed longitudinally on the wing to support bending stresses. The balsa strips were then added to the mid section and at the trailing end of the wing. (refer to figure 4.9)

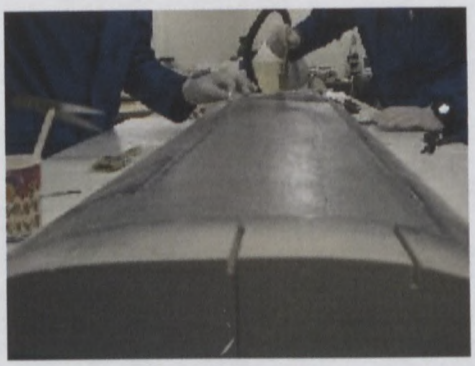

Figure 4.8: Hand layup of the wing half.

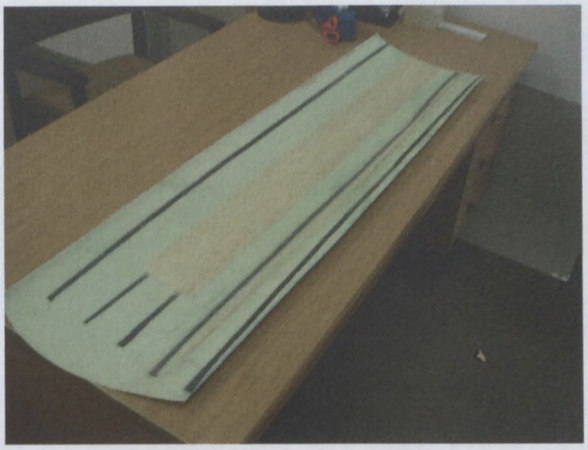

Figure 4.9: The top wing half.

The wing halves were then left in the mould and allowed to cure at room temperature.

A 240mm section of both wing halves at the root ends were then cut off, giving way for the flexible section to be introduced.

Figure 4.10: Wing spar sleeve on bottom half of the wing.

A fibre glass pipe was layed up using one layer of 6 ounce cloth. After curing the pipe was joined to the lower half of the wing acting as a sleeve for the wing spar, as shown in figure 4.10. The pipe was fitted to the wing at the ¼ chord location of the wing profile. This was done to have the maximum lift at $\alpha = 0°$ acting on the centre of the wing spar.

The wing spar was then inserted into the sleeve and fixed inside it to avoid any rotation of the spar, as shown in figure 4.11.

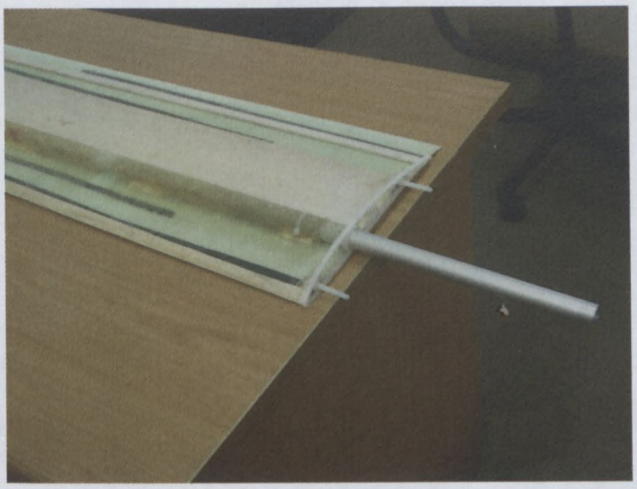

Figure 4.11: Bottom half of the wing with the aluminium wing spar fixed.

4.1.3 Manufacturing of the flexible section

The flexible section consists of a fixed number of airfoil sections (longarines) that are equally spaced and each have the ability to change their geometrical angle of attack individually.

The longarines and spacer beams of the flexing part were all manufactured on a 3 dimensional plastic printer called the Stratasys dimension modeler as shown in figure 4.12.

Figure 4.12: The Stratasys SST dimension modeler.

The longarines and spacer beams were first designed on the CAD program Solidworks®. The longarine sections, shown in figure 4.13, were designed with snap in grooves at the leading edge, top surface front and rear, bottom surface front and rear, and trailing edge. These are there to locate the different spacer beams that form part of the flexing section.

There are three types of spacer beams namely, the leading edge, mid section and trailing edge spacer beams, shown in figures 4.14. There are four mid section beams that are located in the top and bottom grooves.

Figure 4.13: Longarine design.

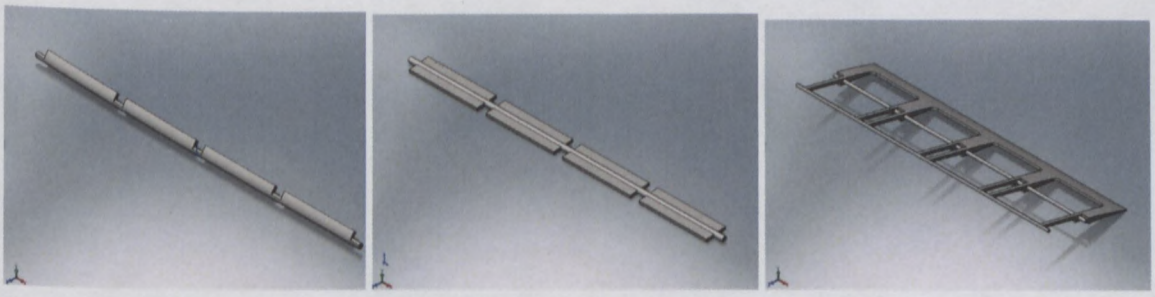

Figure 4.14: Leading edge (left), mid section (center), and trailing edge (right) spacer beams.

The longarine also has a 21mm diameter location for the wing spar which is placed at the ¼ chord position.

Figure 4.15 shows the assembly of the flexing section.

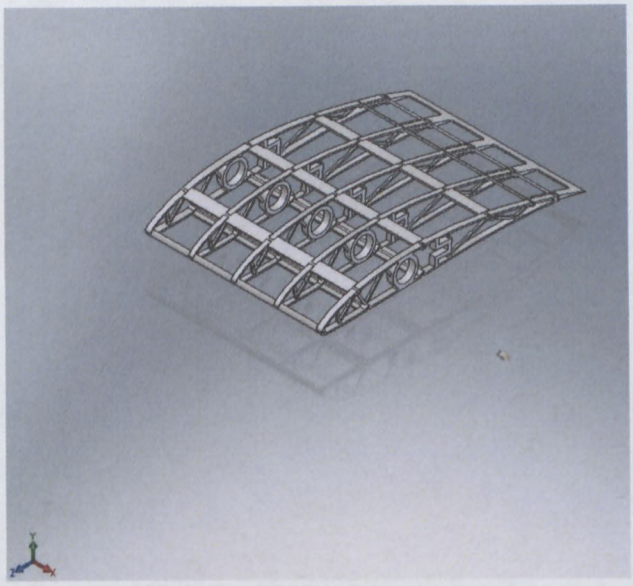

Figure 4.15: Flexing section assembly

The CAD models were then sent to the Dimension printer for manufacturing. The Dimension modeler works with Catalyst®EX software that works behind the scenes (like a printer driver) to orient the design for the most efficient build and generate the necessary support structures. Inside the Dimension printer's build envelope the dual-tipped extrusion head deposits liquefied model and support material following precise paths calculated by CatalystEX. Parts are built layer-by-layer from the bottom up. The printer builds models out of ABS*plus* thermoplastic material. (Impac Systems Engineering, 2009)

The ABS*plus* thermoplastic is set as soon as the printing is done; there is no waiting for the model to cure. Soluble support material dissolves away in a waterbased solution and breakaway supports simply snap off. The model is then ready for use or finishing. (Impac Systems Engineering, 2009)

Figure 4.16 shows the finished longarines and spacer beams after the printing is completed. The finished parts are then assembled, as shown in figure 4.17.

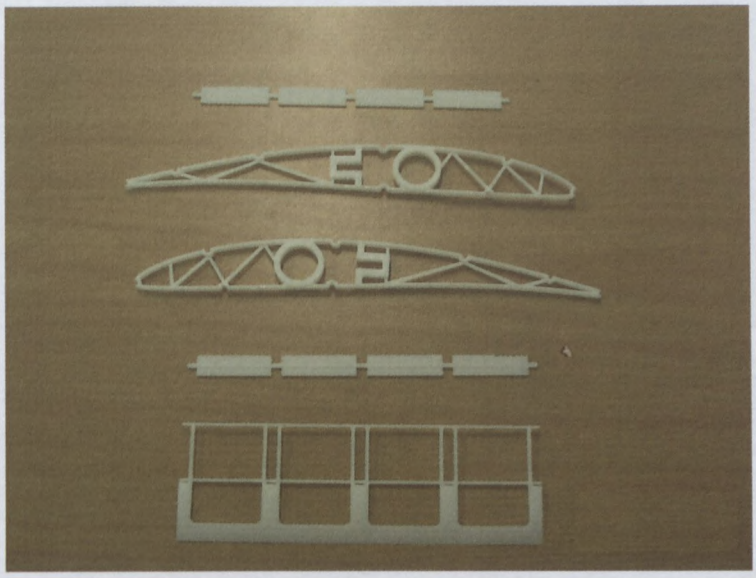

Figure 4.16: Finished printed ABS parts.

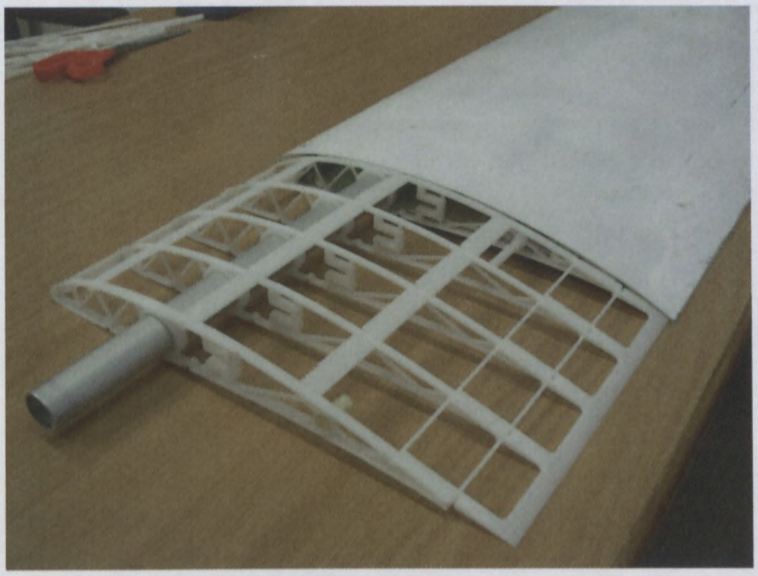

Figure 4.17: Assembled twisting section frame.

The twisting section needed a suitable skin to cover it. It was envisioned that the skin should have a high degree of flexibility and be capable of returning to its original state with little or no elongation. A thermo plastic skin was tested on the flexing section and it is found that the plastic has poor elastic capabilities, as shown in figure 4.18. Surface irregularities that will severely degrade flight conditions form in the skin when deformation is applied.

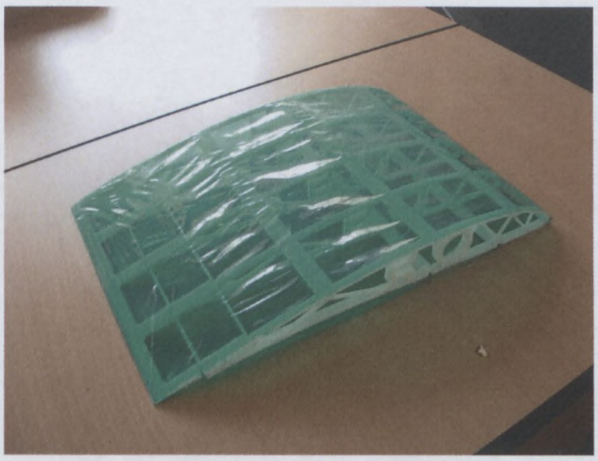

Figure 4.18: Twisting section with a thermo plastic skin.

Elastomers and rubber materials are characterized by their high degree of flexibility and elasticity (high reversible elongation or resilience). (Globalspec, 2009). Liquid latex is pre-vulcanised natural rubber latex that only requires drying to give a strong elastic film.

It was then decided to manufacture a skin out of a latex solution, as latex has excellent stretching properties. A liquid latex solution called Mouldtex was used. The latex was poured out onto a clean dry surface and cured in room temperature while exposed to air. A release agent was sprayed onto the surface before the latex was poured to ensure easy removal of the skin after curing.

It was decided to manufacture two skin halves, as was done with the main section of the wing. The flexible section's size was measured out on the clean and dry surface and a perimeter was put out on the measured area to contain the latex solution within.

After the first attempt it was discovered that the surface must be level during curing for an even thickness distribution of the latex skin. The latex has a thick viscosity and slow curing time which allows the solution to creep down slope if there is a gradient and causes irregular skin thickness, as shown in figure 4.19.

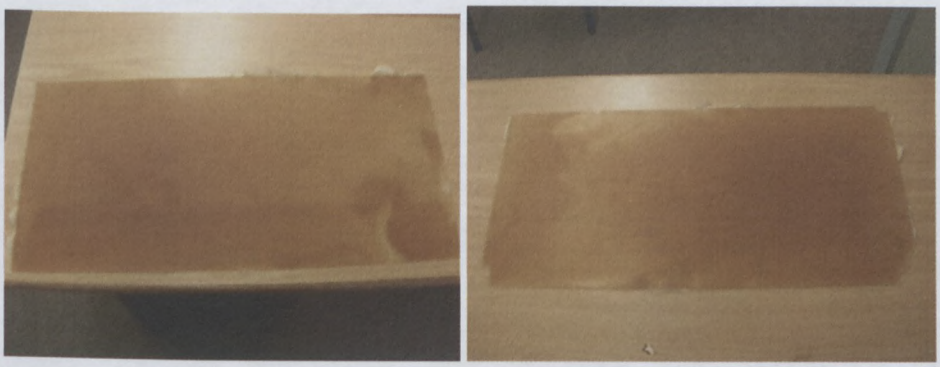

Figure 4.19: Irregular skin thicknesses caused by creeping of the latex.

After a few attempts a preferred method for developing the skin was found, and a few latex skins as shown in figure 4.20 were developed from this method.

Figure 4.20: A preferred solution for the skin.

The skin then had to be bonded to the twisting frame. Many tests were run on different resins ranging from epoxies, PVC and contact adhesives to find the best bonding solution as its difficult to bond rubber to plastic. In conjunction with cleaning and treating the rubber skins before bonding, a viable resin was found for testing purposes.

After the resin was applied and the skin attached to the frame the twisting section was complete, as shown in figure 4.21.

Figure 4.21: Completed flexing section.

4.1.4 Design and manufacturing of the fuselage test rig

A test rig for the wing was designed and manufactured to test the deformation capabilities of the sVAI wing. A proposed design for the actuation mechanism, as shown in figure 4.22, was modeled in Solidworks®. The design shows a lever, housed on a platform, which is attached to the wing spar. The lever arm is attached to a servo, recessed onto a separate platform, via a stay. The wing deformation is achieved by the servo producing a rotational force on the wing spar via the stays through the lever arm. The design of the lever was later simplified to reduce the weight and manufacturing time of the actuation mechanism, as shown in figure 4.23.

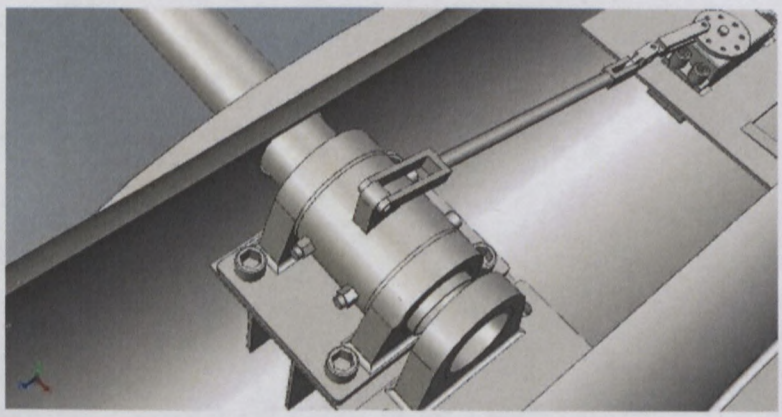

Figure 4.22: The actuation mechanism design.

Figure 4.23: Modified lever arm.

A dummy fuselage was manufactured using the same specifications as the Technology Demonstrator's fuselage. A carbon fiber bush was manufactured to house the wing spar at the ¼ chord position.

The modified lever arm was manufactured out of 16mm thick aluminium. An electrical discharge wire cut machine (EDM Wire Cut), as shown in figure 4.24, was used to cut the part out of the aluminium block. An EDM Hole popper was first used to pop holes for the EDM wire cutter to thread the wire through. A CNC program for the wire cutting process was written on Feature CAM.

The completed lever arm is shown in figure 4.25.

Figure 4.24: EDM wire cut machine (left), EDM hole popper(right)

Figure 4.25: Manufactured lever arm with stay attached.

A balsa wood platform was inserted into the fuselage to house the servo. The platform was placed so that the servo is raised to such a height as to ensure that the stay from the lever arm is horizontal. Once the platform was inserted the fuselage rig was ready for assembly.

The intricate parts for the sVAI wing actuation mechanism are shown in figure 4.26. They consist of the flexible section (left), servo motor (top center), wing locator pin (bottom center), lever arm and stay (top right), lever screw (mid right) and wing attachment screws (bottom right).

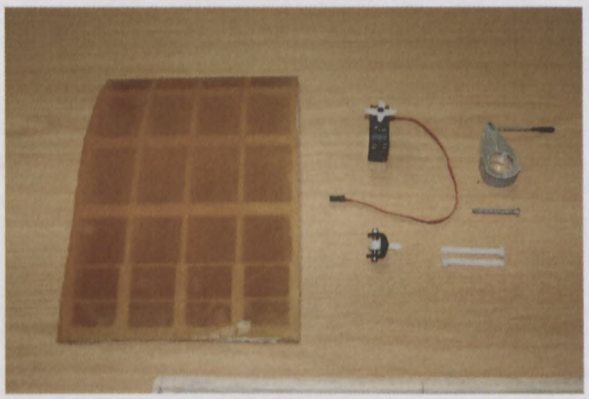

Figure 4.26: Actuation mechanism parts

The wing locator pin is used to locate the wing at its angle of incidence, the lever screw fixes the wing spar and lever arm together and the wing attachment screws are used to attach the flexible wing section to the main wing.

Figure 4.27 shows the assembled twisting mechanism and figure 4.28 shows the entire assembled test rig.

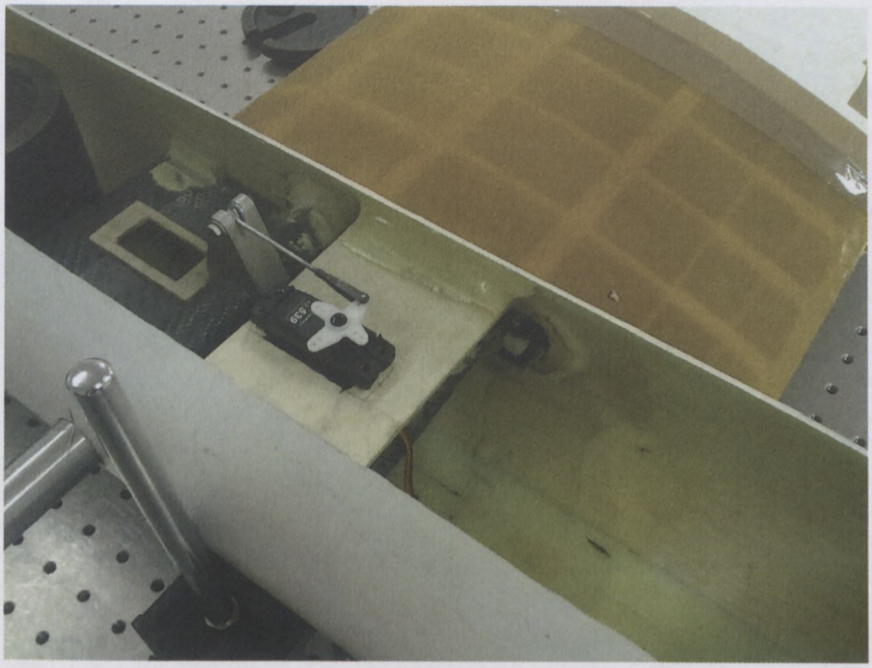

Figure 4.27: The assembled actuation mechanism.

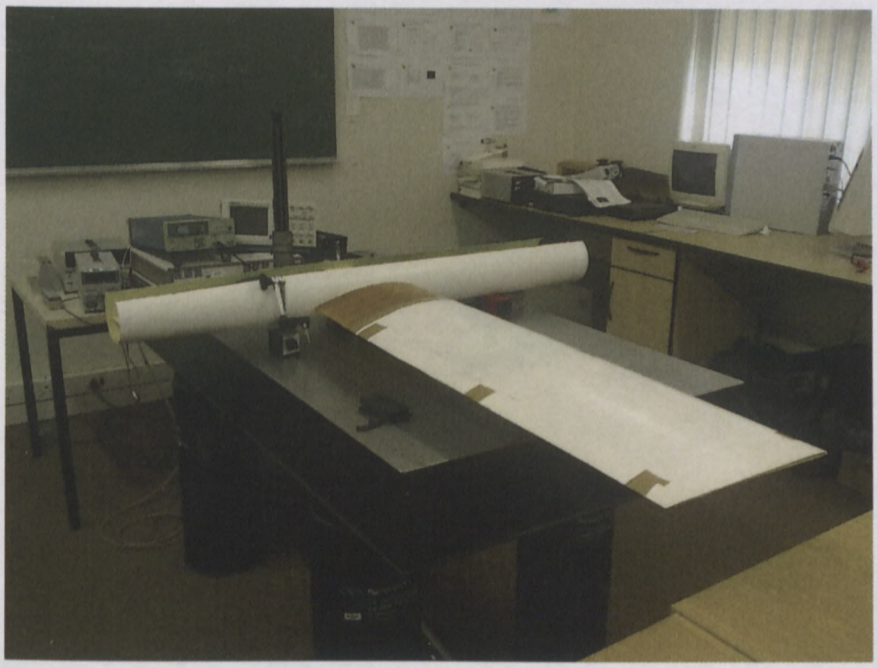

Figure 4.28: The assembled test rig.

CHAPTER 5

This chapter discusses the scanning of the manufactured prototype, the conversion of the scan to 3D solid model, and the comparison between the scan and CAD models. The difference between the models is briefly discussed.

5.1 SCANNING

The twisting concept was conceptualized and modeled on Solidworks® using the loft function as a means of representing the twisting deformation. This is represented in the above left inset in figure 5.1. CFD analyses were run on this model to prove its aerodynamic prowess in performance over the conventional wing. The concept was then further designed and developed on Solidworks® for manufacturing, as shown in the above right inset in figure 5.1. Using this CAD model, the prototype represented in the below inset in figure 5.1 was built.

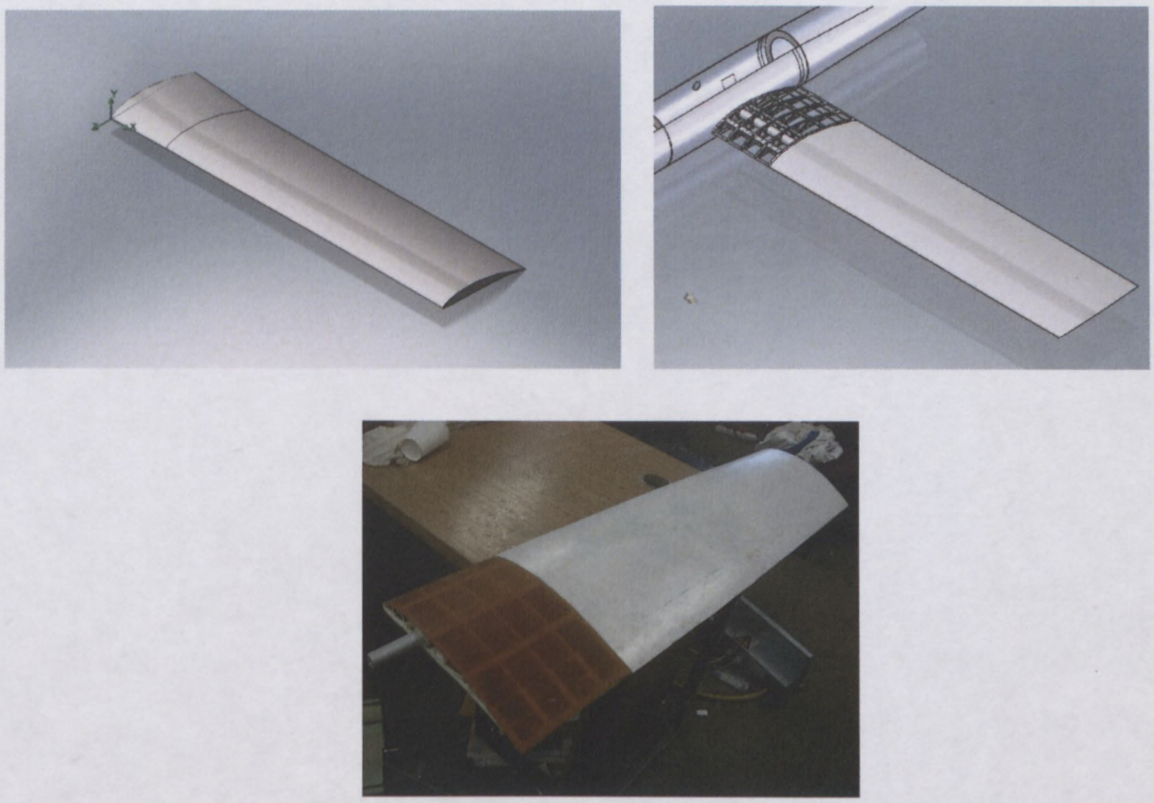

Figure 5.1: Twisting concept evolution. Above left, CAD model of conceptualization used in analysis. Above right, design and development of concept. Bottom, manufactured concept.

It was found that the maximum twist deflection of the prototype is 5° in the positive direction, and 9° in the negative direction. Figure 5.2 shows the prototype in twisting action, from maximum positive, through neutral (zero twist), to maximum negative.

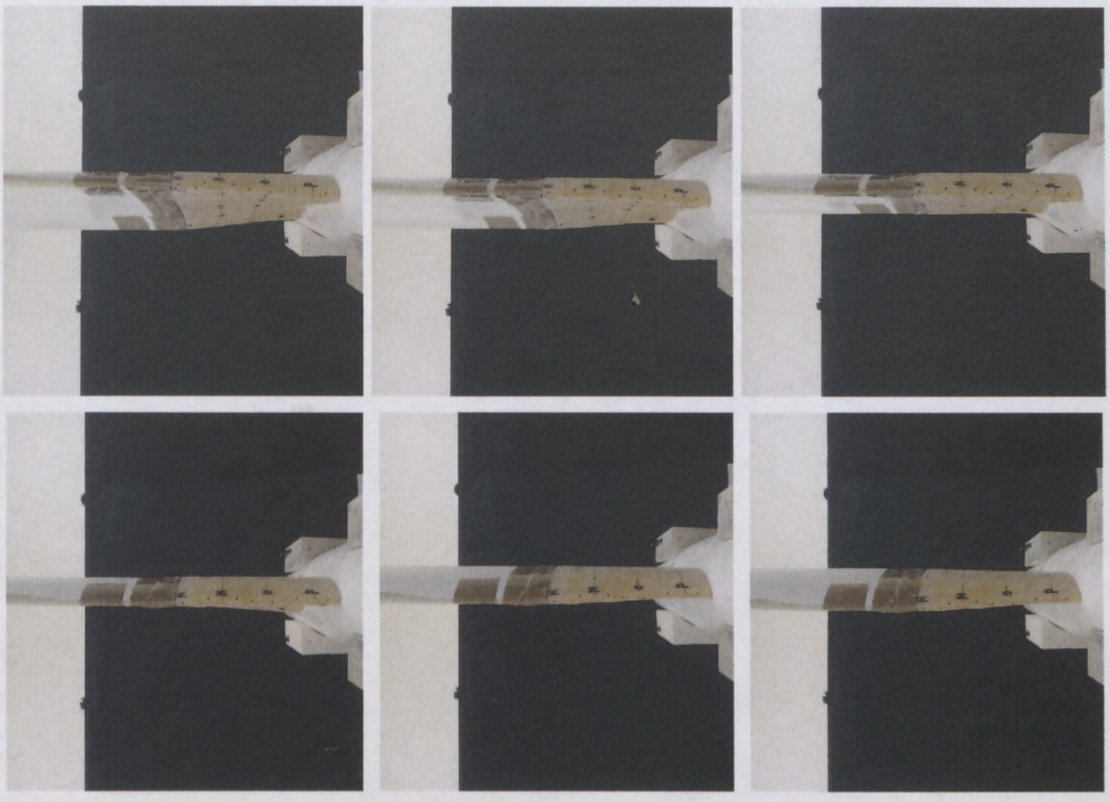

Figure 5.2: Twisting action of prototype, from max positive to max negative.

The next step was to show that the deformation characteristics of the prototype are the same as with the CFD model. This was done by making 3D scans of the prototype, converting them to CAD files and then making the comparisons. A Konica Minolta VI9i Scanner, as shown in figure 5.3, is used for the 3D scanning. This system can provide accurate 3D measurements, and perform shape evaluations and quality inspections of a product or prototype.

The wing prototype was setup into three different morphing stages namely, maximum positive, zero twist and maximum negative.

Figure 5.3: Minolta non contact 3D digitizer

The Polygon Editing Tool (PET) software was used in conjunction with the camera to produce the 3D scans. The PET enables one to control the camera and easily scan, polygonize, edit and convert scanned data into any one of several common data formats. These formats include STL, DXF, wavefront, WRL and point cloud ASCII format. PET also provides functions for data alignment, data merging, smoothing, uniform data reduction, texture blending, polygon check and adaptive data reduction. (Konica Minolta. Polygon Editing Tool, 2009)

The wing was positioned vertically, with wing tip facing the ceiling. Extra light was brought into the room to help the camera to focus and capture maximum data. A black background screen was also used to aid in this. A medium focus lens was used on the camera as it was easier to focus on larger components that are placed close by. The camera was then allowed to focus and then the image was captured. The wing was allowed to rotate while the camera is stationery to allow scans of the entire twisting section to be taken. This is done to ensure the camera is always able to focus and the light balance remains virtually the same. Once the camera focuses, the laser scans the model and the image data is shown on the PET software.

Figure 5.4 shows the PET software during scanning. Control of the scanning is done using the file import digitizer window at the bottom of the screen, while scanned data progress is monitored in the top two windows.

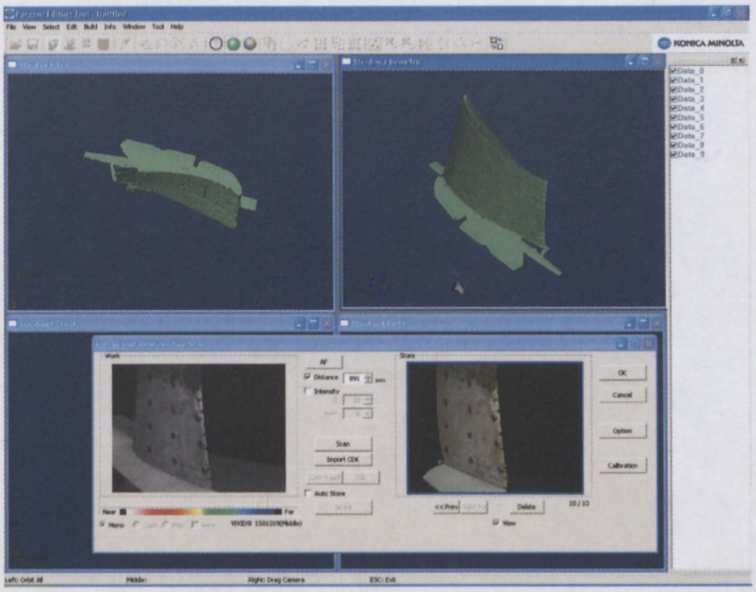

Figure 5.4: Screenshot of the Polygon Editing Tool during scans.

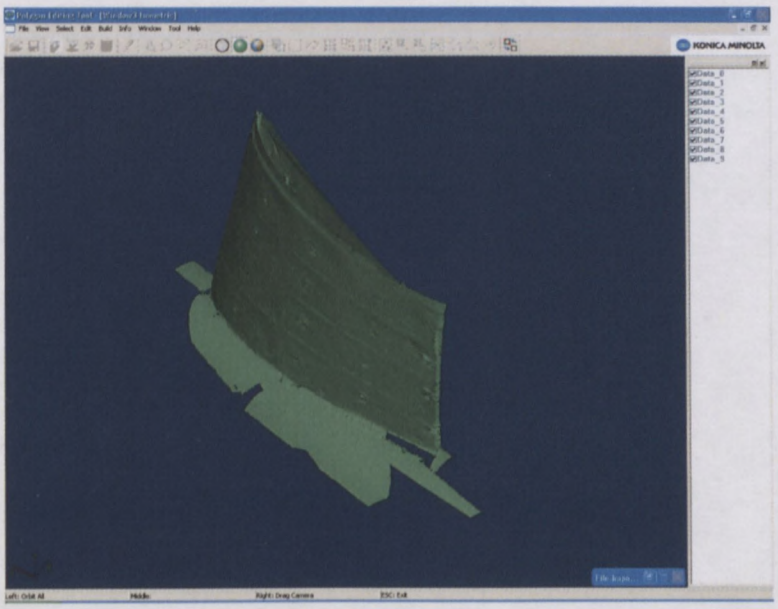

Figure 5.5: Screenshot of PET with completed scan.

Each image is stored as a data file. At the end of the scanning all the data files are amalgamated to form one completed 3D scan, as shown above in figure 5.5.

5.2 CONVERT SCAN TO 3 DIMENSIONAL SOLID BODY

The scanned file was saved as a WRL file and then imported into Solidworks®. The file was thus imported as a point cloud as shown in figure 5.6.

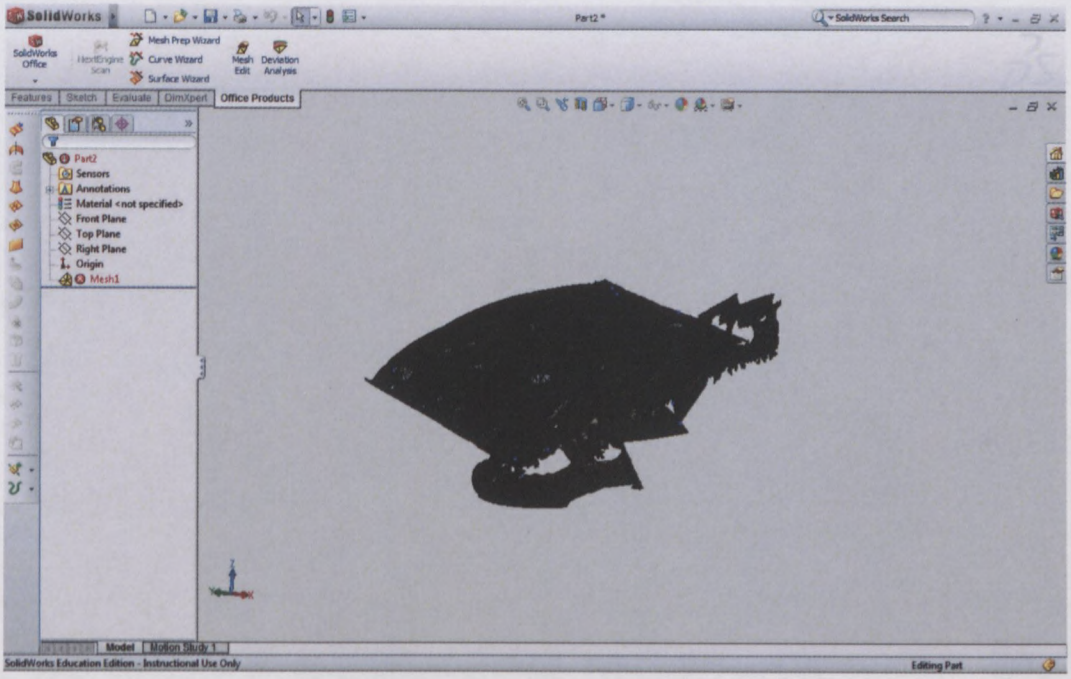

Figure 5.6: Scan in point cloud format

In order to create a solid model from the scan, the point cloud was simplified and reduced to form an efficient mesh. The resulting mesh was used to create a surface body that will be knitted together and sealed for the final conversion to a complete solid body.

5.2.1 Mesh Simplification

Firstly the point cloud was simplified to create an efficient mesh. All extraneous data was removed and the scan is tidied up, as shown in the before and after screenshots in figure 5.7.

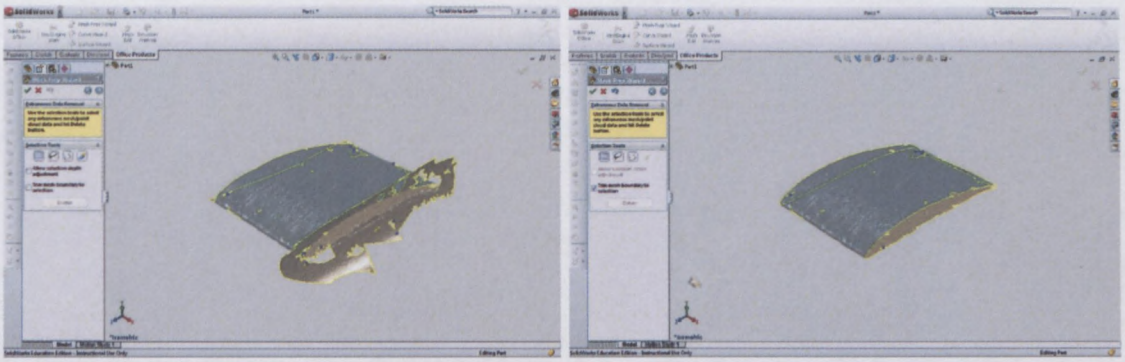

Figure 5.7: Left, before extraneous data removal. Right, after extraneous data removal.

The mesh was then simplified and reduced by reducing the number of vertices in the mesh feature. This results in a simpler and smaller file size, thus increasing model mesh efficiency. Figure 5.8 shows the scan before and after mesh reduction and simplification.

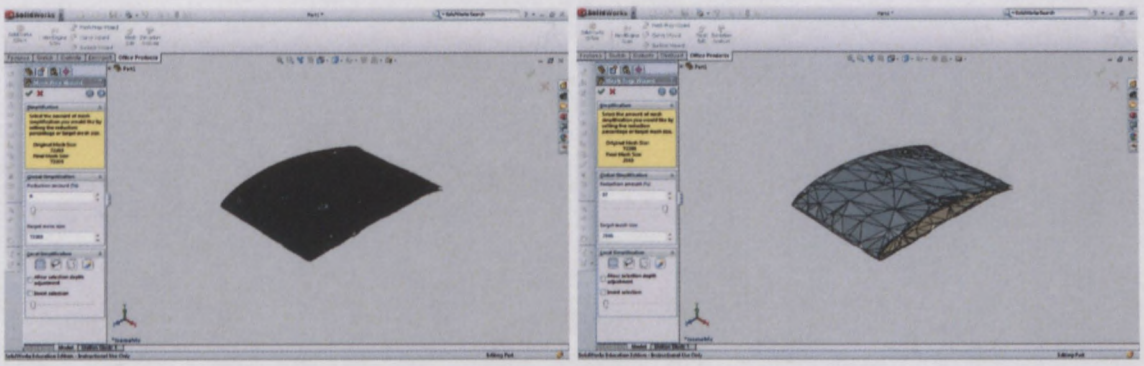

Figure 5.8: Left, before mesh reduction. Right, after mesh reduction.

After the boundary edges are smoothed (as shown in figure 5.9) and all holes are automatically filled the mesh is then prepared, shown in figure 5.10.

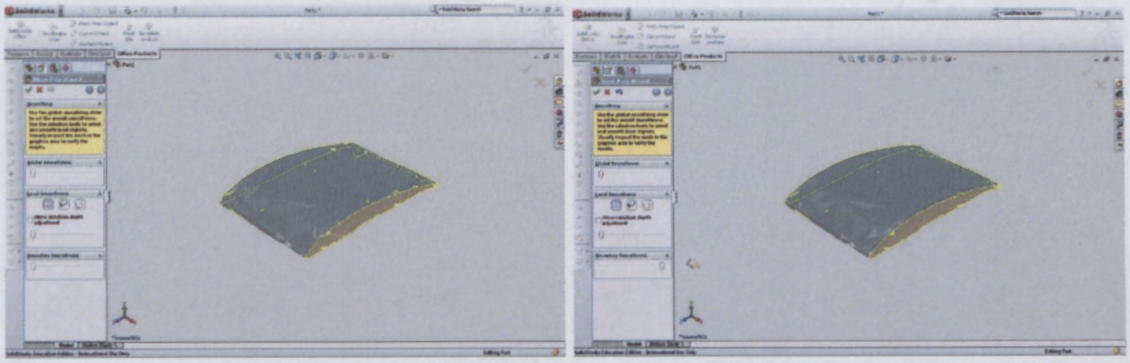

Figure 5.9: Left, before smoothing. Right, after smoothing

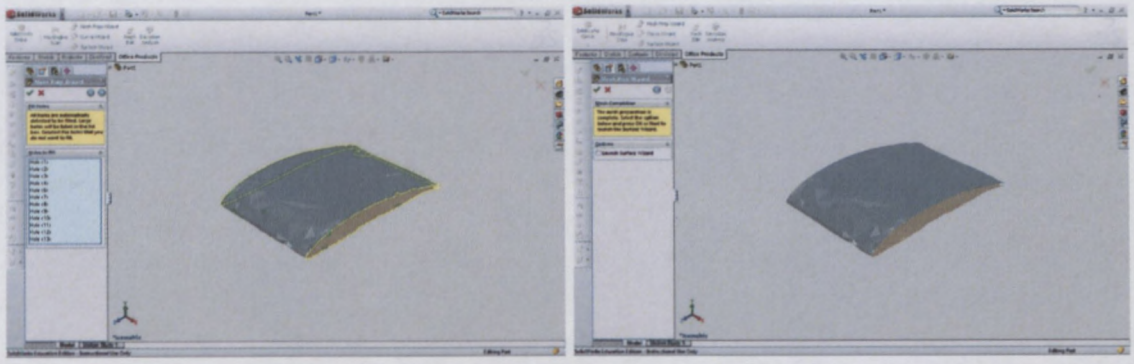

Figure 5.10: Left, unwanted holes are filled. Right, mesh is prepared.

5.2.2 Surface creation

Surfaces were created using the mesh. Automatic surface creation was used and according to the quality and quantity of the mesh a certain amount of surfaces was created as shown in figure 5.11. The finer the mesh the more surfaces are created.

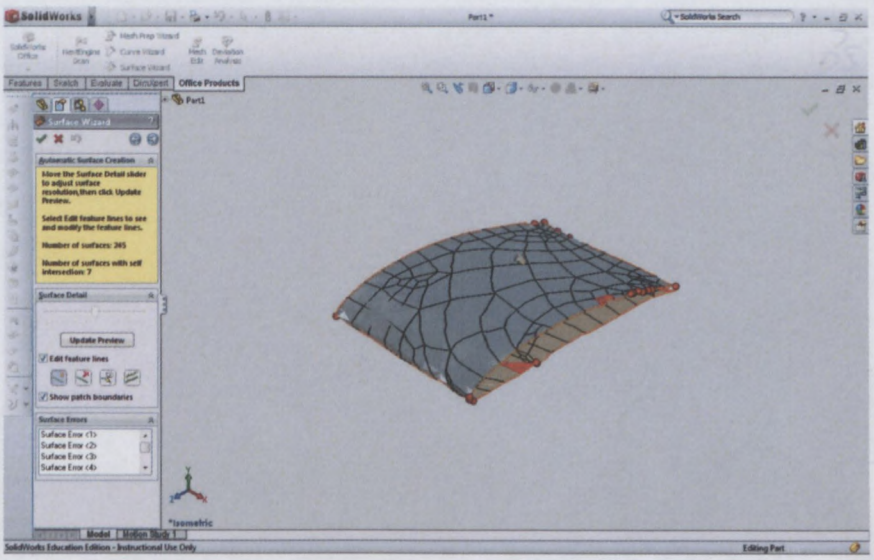

Figure 5.11: Automatic surface creation.

Errors in the form of self intersecting surfaces occur because of the topographical features of this scanned model, as shown in figure 5.12. These errors need to be corrected for the healthy production of an enclosed water tight surface body. If the error cannot be corrected the surfaces involved in the error are deleted.

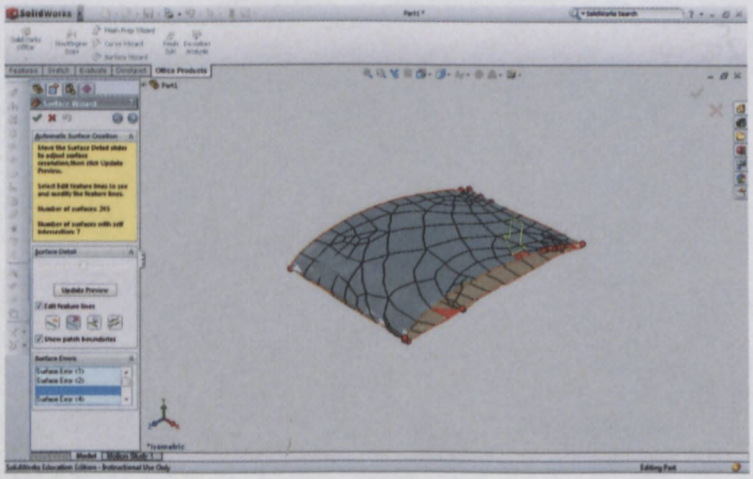

Figure 5.12: Self intersecting surface errors

The editing of feature lines can correct these errors and extract more desirable surfaces. Feature lines are lines that form the boundaries between regions on a body. These are indicated by the orange lines. The red dots represent the end of the feature lines and the black lines show patch boundaries. The red mesh lines show where the self intersecting surfaces are. These can be seen in figures 5.12 and 5.13.

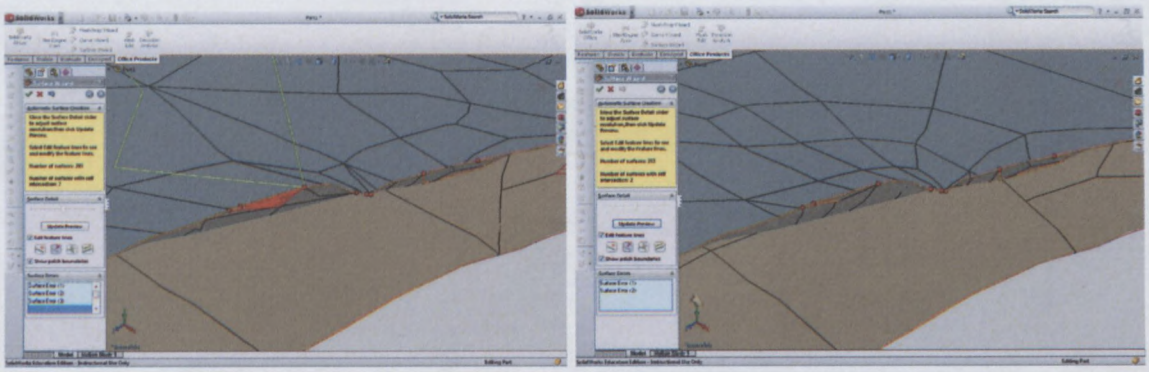

Figure 5.13: Surface error reparation by editing feature lines. Left, before feature line deletion. Right, after feature line deletion.

To correct these surface errors one can edit the feature lines by adding, deleting, moving or relaxing a feature line. Figure 5.13 shows the deletion of a feature line that corrected a surface intersection, thus reducing the amount of surface errors.

Surface errors that could not be resolved are removed by deleting the surfaces that intersect, as shown in figure 5.14. These surfaces are remodeled using sketching and surface modeling techniques.

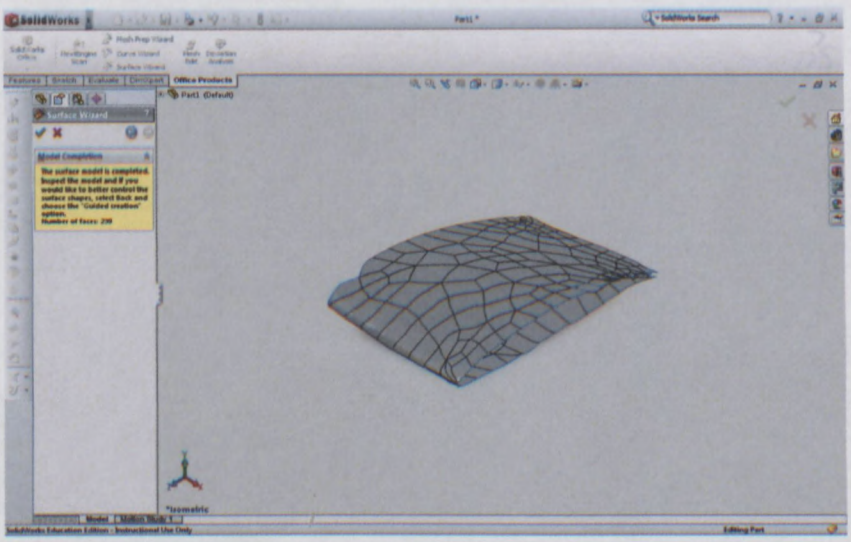

Figure 5.14: Surface errors are deleted.

5.2.3 Forming a solid body

The mesh was then converted to a surface body which is to be converted to a solid body. Solidworks® distinguishes between a solid and a surface by the following rule; every edge is the boundary between two faces in a solid and one face in a surface. Therefore a solid will have a thickness, while a surface is infinitely thin.

Joining surface bodies at their edges to enclose a volume will produce a solid body. This is the idea when approaching surface modeling of a scan. The surface body needs to be enclosed and made water tight for a solid body to be produced from it. Planar surfaces were added to each side and trailing edge of the scan, as shown in the left inset of figure 5.15. Surfaces that were deleted due to errors were also remodeled using the surface patch feature, as shown in the right inset of figure 5.15. This was done by selecting the edges that enclose the gap and applying surface patch and boundary repair.

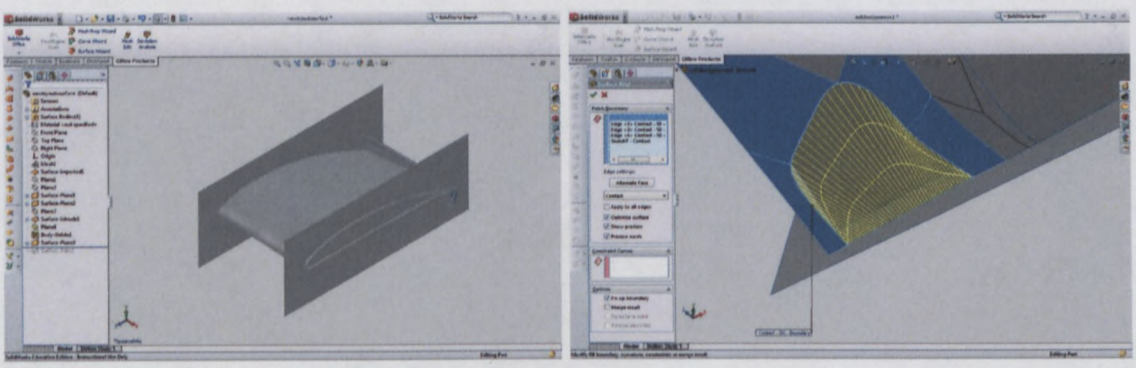

Figure 5.15: Surface modeling. Left, planar surfaces are created to close up the model. Right, patch surface feature is used to fill in gaps where surfaces were deleted.

After all the gaps were filled and the volume completely enclosed, the surface trim tool was used to trim all the rough edges of the scan using the planar surfaces as a trimming tool. The scan was then used as a trimming tool to trim the planar surfaces to fit the scan geometry. The surface knit feature, allowing solid body creation, was then used to knit all the surfaces together and form a solid from the original scan, as shown in figure 5.16.

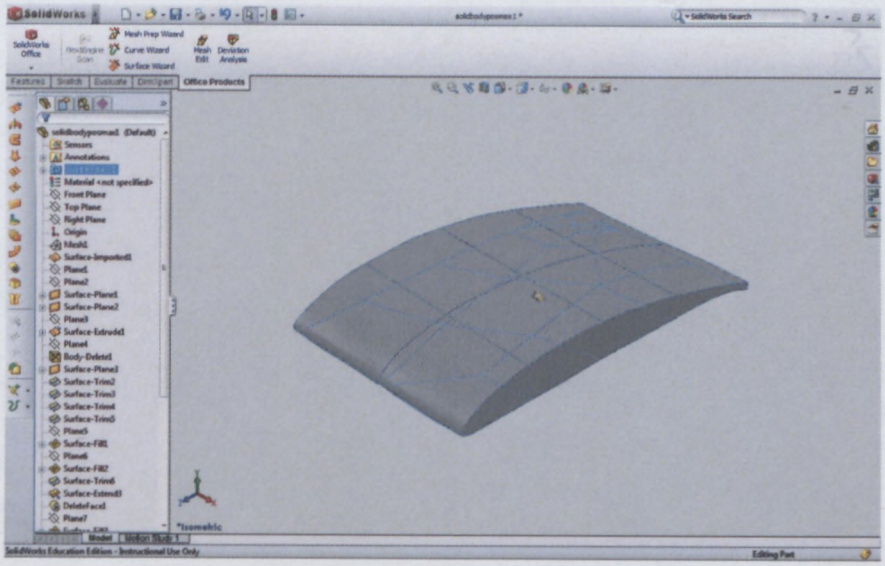

Figure 5.16: The scan as a solid body.

5.3 CAD AND SCAN COMPARISON

The conversion made it possible to compare the scan as a solid body to the initial CAD model used for the analyses of the sVAI wing. The flexible section of the prototype of the sVAI wing should produce similar geometrical characteristics as the CAD model does during morphing.

Scans were taken of the wing at maximum positive and negative, and at 0°. These now 3 dimensional CAD files are super imposed on to the initial CAD model at 5°, -9° and 0° respectively. These are shown in figures 5.17, 5.18 and 5.19.

The red profile is the scanned model while the blue profile is the CAD model.

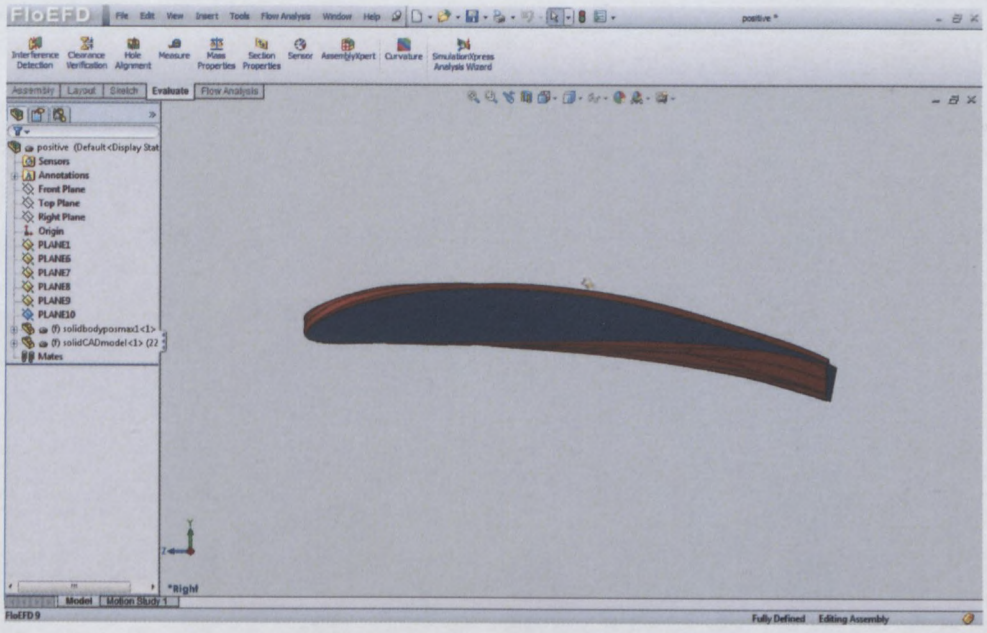

Figure 5.17: Superimposed wings at 5° angle of twist.

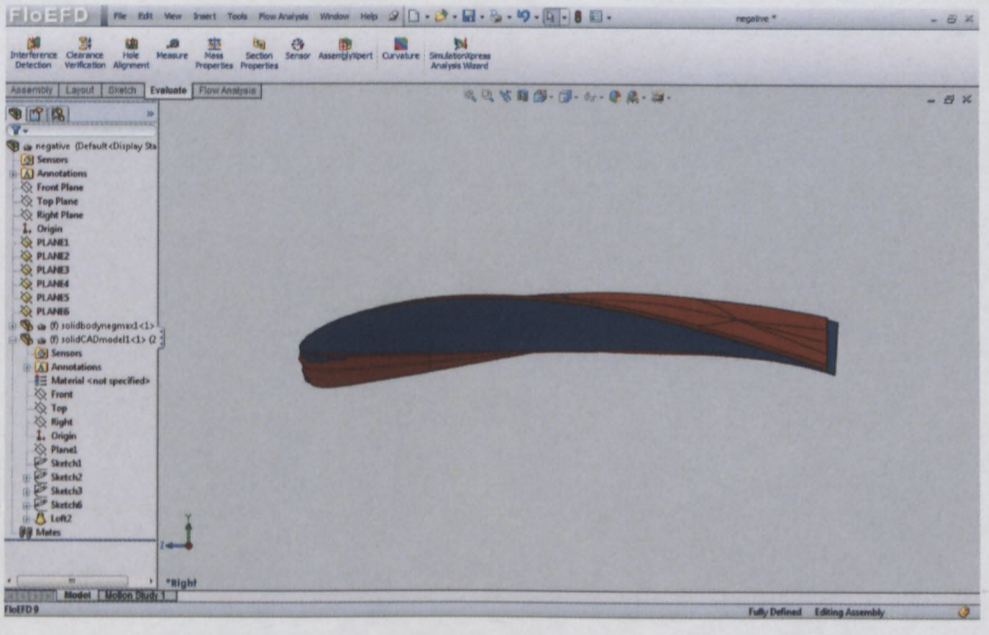

Figure 5.18: Superimposed wings at -9° angle of twist.

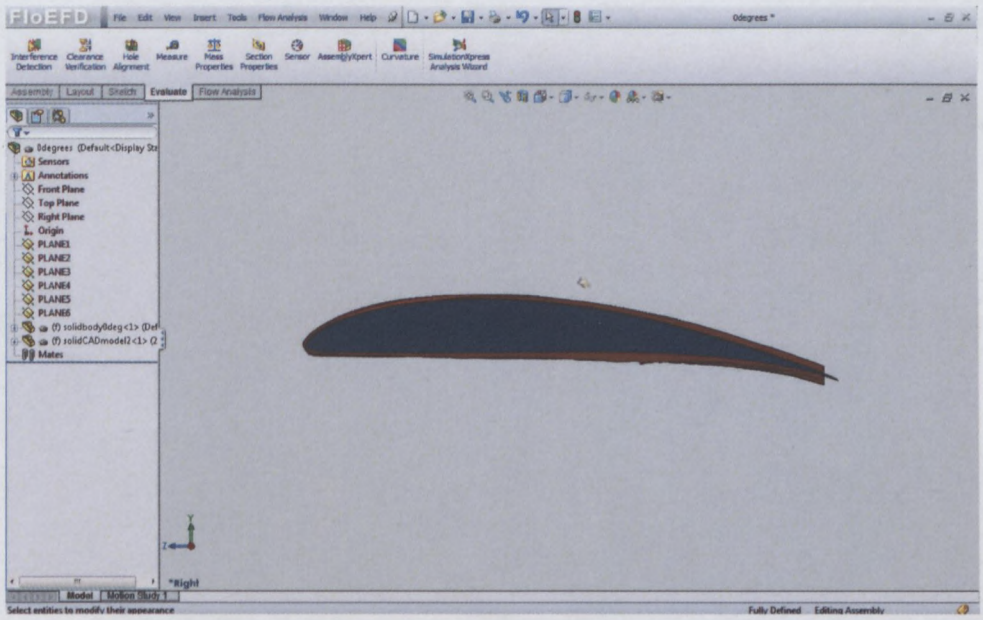

Figure 5.19: Superimposed wings at 0° twist.

From the images above it was seen that there were certain differences between the models. The chord length of the CAD model is slightly more than that of the scan model, because extraneous data at the trailing edge was removed to enable scan to 3D conversion. The thickness of the scan model is also more than that of the CAD model, because of the flexible skin. The values can be seen in table 5.1.

	CAD	SCAN
CHORD (mm)	301	296
THICKNESS (mm)	30.5	34.5
AREA (m^2)	5.80E-03	6.50E-03

Table 5.1: CAD and scan profile comparison.

From the above data it can be seen that the CAD model's chord is ±2% more than the scan model, while its thickness and area are ±11% and ±10% less respectively.

The difference between twisting deformation was tested. The wing sections are divided into six planes equidistant from each other for both maximum positive and

negative models. The planes were set at ±36mm from each other. At each plane the profile geometrical angle of the wing sections are compared to each other.

The geometrical angle of attack was measured off the angle of the chord line of each profile. The chord line was taken from the most forward point of the leading edge to the most aft point of the trailing edge of each wing section on each plane.

The difference obtained between the geometrical angles of attack of the wing sections of the CAD and scanned models is expressed as a percentage, using the CAD model as the benchmark. This was done for all the planes of each wing section individually. The overall percentage difference of the deformation was then obtained by calculating the average difference throughout the wing section for max positive and negative models respectively, by using the standard average equation shown below,

$$Average = \frac{1}{n}\sum_{i=1}^{n} a_i \qquad \text{(Hardy et al.,1988)} \qquad (30)$$

where, the sum of a_i divided by the number of terms (n) gives you the average.

Figure 5.20 shows the superimposed wing sections at maximum positive (5° twist), while figure 5.21 shows the profile comparisons at the different planes. The CAD model is the blue inner profile and the scanned model is the red outer profile. From figure 5.20 one can see that there is little difference in the topography between the two wing section models during twisting.

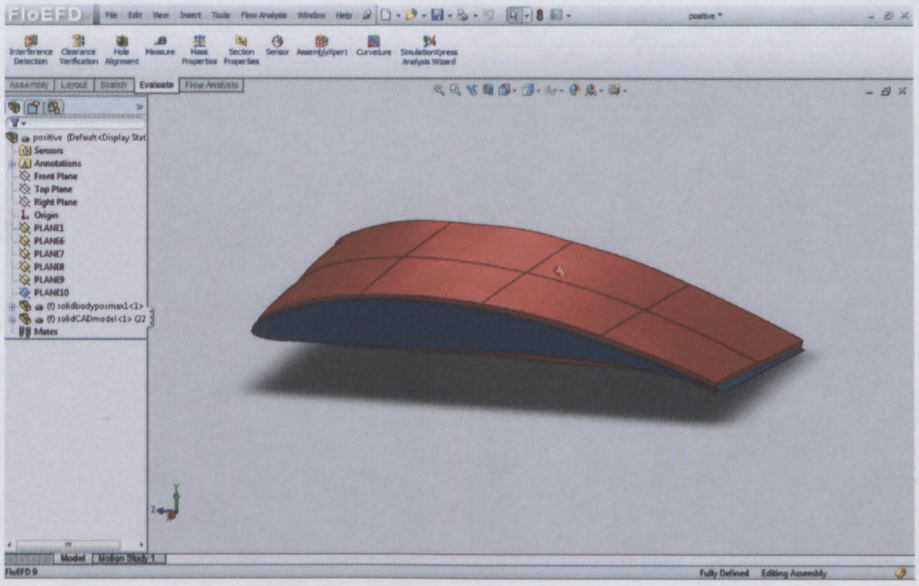

Figure 5.20: 3 dimensional view of the wing sections at 5° twist.

Figure 5.21: Geometrical angles of attack of the flexible section for 5° twist at the different planes. Top left, 3°. Top center, 4°. Top right, 5°. Bottom left, 6°. Bottom center, 7°. Bottom right, 8°.

The top left inset in figure 5.21 is a sectioned view of the models from the wing root end and both are set at an incidence angle of 3°. The geometrical angle of attack of the profiles increase from top left to right and then bottom left to right. The bottom right inset is the profile at maximum positive twist, which is 5° from the incidence angle. The CAD model's geometrical angle of attack is 3°, 4°, 5°, 6°, 7° and 8° for each sectioned profile. The scanned model's geometrical angle of attack was then compared at each sectioned profile to that of the CAD model.

The scanned model's geometrical angle of attack was found to be equal at 3°, 2% less at 4°, equal at 5°, 1.6% more at 6°, 0.6% more at 7° and 3% less at 8°, compared to the CAD model for maximum positive twist. This gave an average geometrical difference of 1.2% for positive twisting.

Figure 5.22 shows the superimposed wing sections at maximum negative (-6° twist), while figure 5.23 shows the profile comparisons at the different planes. The CAD model is the blue inner profile and the scanned model is the red outer profile. Figure 5.22 shows a little but clear difference in the topography between the two models during twisting.

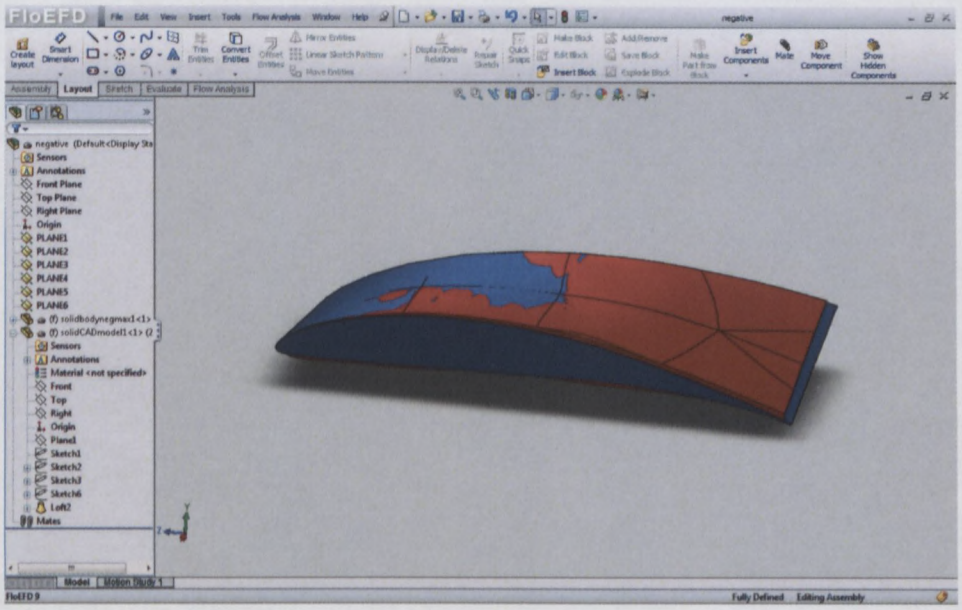

Figure 5.22: 3 dimensional view of the wing sections at -9° twist.

Figure 5.23: Geometrical angles of attack of the flexible section for -9° twist at the different planes. Top left, 3°. Top center, 0.9°. Top right, -0.9°. Bottom left, -2.5°. Bottom center, -4.5°. Bottom right, -6°.

The top left inset in figure 5.23 is a sectioned view of the models from the wing root end and both are set at an incidence angle of 3°. The geometrical angle of attack of the profiles decrease from top left to right and then bottom left to right. The bottom right inset is the profile at maximum negative twist, which is -9° from the incidence angle. The CAD model's geometrical angle of attack is 3°, 0.9°, -0.9°, -2.5°, -4.5° and -6° for each sectioned profile. The scanned model's geometrical angle of attack was then also compared at each sectioned profile to that of the CAD model.

The scanned model's geometrical angle of attack was found to be equal and 3°, 2% less at 0.9°, 2.3% less at -0.9°, 4.6% less at -2.5°, 3.3% less at -4.5° and 5.3% less at -6°, compared to the CAD model for maximum negative twist. This gave an average geometrical difference of 3% negative twisting.

The geometrical deformation of the manufactured sVAI wing prototype is very similar to the sVAI wing CAD model used for the analyses. The use of longerines and spacer beams in the manufacturing and assembly of the twisting section allows for controlled and seamless twisting as in the CAD model. The choice of a latex skin to cover the twisting section is a good one as it picks up little to no topographical irregularities during twisting. Therefore, one can assume that equipping a small to medium unmanned aircraft with an sVAI wing will improve the flight performance of the aircraft as shown by the analyses on the CAD model.

CHAPTER 6

The conclusions are discussed in this chapter.

The primary objective of this study was to develop a seamless wing morphing concept that could increase the takeoff and climb performances of the CPUT Adaptronics AMTL Technology Demonstrator and to study its effects on the overall performance of the aircraft. A seamless variable angle of incidence (sVAI) morphing wing was thus conceptualized for its ability to increase lift and decrease drag by seamlessly altering its angle of incidence as a control surface system. In order to achieve the primary objective, the following sub-objectives were achieved.

- An investigation of the effects that the sVAI wing could have on the takeoff phase of flight of the vehicle was completed. 3D CAD models of the conventional (CON) wing and sVAI conceptualization were modeled on Solidworks®. These models were then put under analyses using the CFD

program Engineering Fluid Dynamics (EFD). The wings were set at an angle of 3°, representing the angle of incidence that wings are set at on the aircraft, during the takeoff simulations and run at velocities ranging from 10m/s to 33.33m/s. The results from the takeoff analyses showed that the sVAI wing at a positive twist angle of 4° has a superior wing performance than the wing at 0° twist and the CON wing at all angles of flap. The stall velocity (V_{stall}) and ground roll (S_g) for the 0° deflection wing was decreased by 17% and 31%, respectively when a positive twist of 4° is applied. The performance is greatly increased due to the fact that the aircraft would be able to increase its lift during ground roll. A conventional aircrafts inability to do this is the reason for its high energy expenditure during takeoff.

- An investigation of the effects that the sVAI wing could have on the climb phase of flight of the vehicle was completed. 3D CAD models of the CON wing and sVAI concept were modeled on Solidworks® and put under analyses using EFD. The wings were set at a climb angle of 8° and run at velocities ranging from 16.667m/s to 33.33m/s. The results from the climb analyses showed that the sVAI model at a negative twist angle of 2° produced ±14% less drag than the wing at 0° deflection, but also reduced the lift by ±13%. Because of the small twisting section, the twisting action behaves a lot like changing the angle of attack of the entire wing. This makes it very difficult to reduce drag without reducing lift as changing the angle of attack of the entire wing directly impacts the lift and drag experienced by the entire aircraft.

- An investigation of the effects that the sVAI wing could have on the power consumption of the vehicle during the takeoff flight phase was completed. The results obtained from the takeoff analyses show that the sVAI wing with a 4° twist asks for ±11.7% less power than the wing at 0° deflection and ±13% less power than the CON wing at maximum flap. The sVAI concept therefore reduces the power consumption during the takeoff phase of flight, because it's able to increase its lift with less coupling to critical drag thus increasing its L/D and $C_L^{3/2}/C_D$ values.

- An investigation of the effects that the sVAI wing could have on the power consumption of the vehicle during the climb flight phase was completed. The results obtained from the climb analyses showed that the wing with 0° deflection had the most efficient power consumption. Even though the sVAI wing was able to have the largest drag reduction during climb, the reduction of lift affected the power consumption by reducing the $C_L^{3/2}/C_D$ value and therefore degraded the rate of climb.

- An investigation of the effects that the sVAI wing could have on the overall range and endurance and overall flight performance of the vehicle was completed. The sVAI concept produced the shortest S_g during takeoff with the least power expenditure. Its aerodynamics however did not increase the climbing performance. However, the sVAI could allow an aircraft to takeoff within a shorter distance with little power expenditure and reach its operational ceiling in a shorter time. The sVAI concept therefore reduces the power and fuel consumption during the takeoff phase of flight by increasing its L/D and $C_L^{3/2}/C_D$ values. This would extend the overall range and endurance of the aircraft and therefore, increase the overall flight performance of the vehicle.

- The manufacturing of the sVAI wing fitting the specifications of the CPUT Adaptronics AMTL Technology Demonstrator was accomplished. The sVAI concept prototype was designed and developed on Solidworks®. The sVAI wing was manufactured at the CPUT AMTL using only CPUT manufacturing facilities. A wing mould was manufactured using a powder-binder 3D printer and a wing shell was then layed up in the mould using fiber glass and carbon fibre with balsa wood strips for strengthening. An ABS plastic 3D printer was used to grow the wing sections and spacer beams that make up the twisting section. A wing skin made of latex was produced, for its excellent stretching and resilient properties, and fitted onto the assembled twisting section. Difficulty was found in trying to bond the latex rubber to the ABS plastic parts. A temporary solution was found to keep the structure intact, but its integrity is very doubtful.

The actuation system consists of a servo motor attached to a lever arm, which was manufactured by a CNC wire cutter. The servo motor experienced difficulty in actuating because of the weight of the wing. The weight caused the wing to sag increasing friction between the wing spar and wing spar sleeve located on the test rig making it harder for the servo motor to overcome the weight.

- The fitting of the sVAI wing to a test rig to determine its morphing ability and thus make predictions about the flight performance of the actual vehicle was achieved. The sVAI wing was actuated via remote and the degree of deformation was measured by taking 3D scans of the model. Point clouds were imported into Solidworks® and then converted to a 3D model that allowed one to compare it against the CAD analysis model. The comparison showed a very close exactness of the models' geometrical and topographical deformation when twisted. The scanned maximum positive twisting deflection model had an average geometrical difference across the twisting section of 1.2% as compared to the CAD model, while the maximum negative had a difference of 3%. This could allow one to predict that the flight trends found numerically would be the performance characteristics in flight.

In conclusion, this thesis has presented the conceptualization, design, development and manufacturing of a seamless morphing wing that could increase the aerodynamic performance of the CPUT Adaptronics AMTL UAV Technology Demonstrator, and possibly other similar platforms.

CHAPTER 7

This chapter discusses the recommendations made.

A few recommendations were made regarding the research. These are listed below.

- A method to enable less lift loss during the negative twisting to aid in the climb performance should be found. A longer twisting section or alternate twisting section placed at the wing tip that allows for a more gradual change of geometrical angle of attack of the wing sections could allow this. The wing tip would be at a lesser angle compared to the rest of the wing, allowing lift to be generated at the mid to wing root end and drag to be reduced via washout. This will enable the wing to produce more excess power, thus increasing its rate of climb.

- During the manufacturing process an alternate method of bonding the flexible latex skin to the plastic frame should be developed. The adhesive used will not suffice as it performs poorly in the bonding of rubber to plastic.

- Actuation of the wing was found to be difficult due to the weight of the wing. A recommendation to overcome this is to use less material during manufacturing of the wing resulting in less weight. Also a thinner latex skin should be used, allowing for easier actuation by the servo motor and less weight on the wing. One could also replace the servo motor for a stronger one.

Much is still to be done to improve the seamless variable angle of incidence concept and fit it to an aircraft for flight testing. Further design work to allow for two twisting wings to fit on a fuselage is to be done. The actuation system must be improved to be able to actuate both wings independently, thus allowing differential lift and effective roll control. The structural integrity of the entire wing system must be improved and tested to able to withstand forces during flight.

APPENDIX I

EFD RESULTS

COEFFICIENT OF LIFT (CL) VS FLAP AND TWIST ANGLE

V=16.667m/s

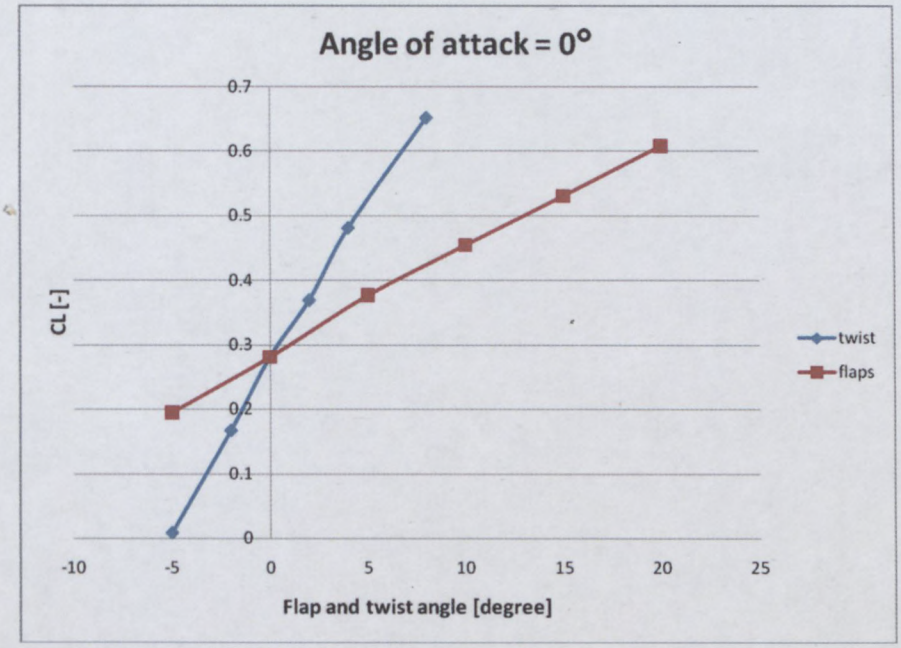

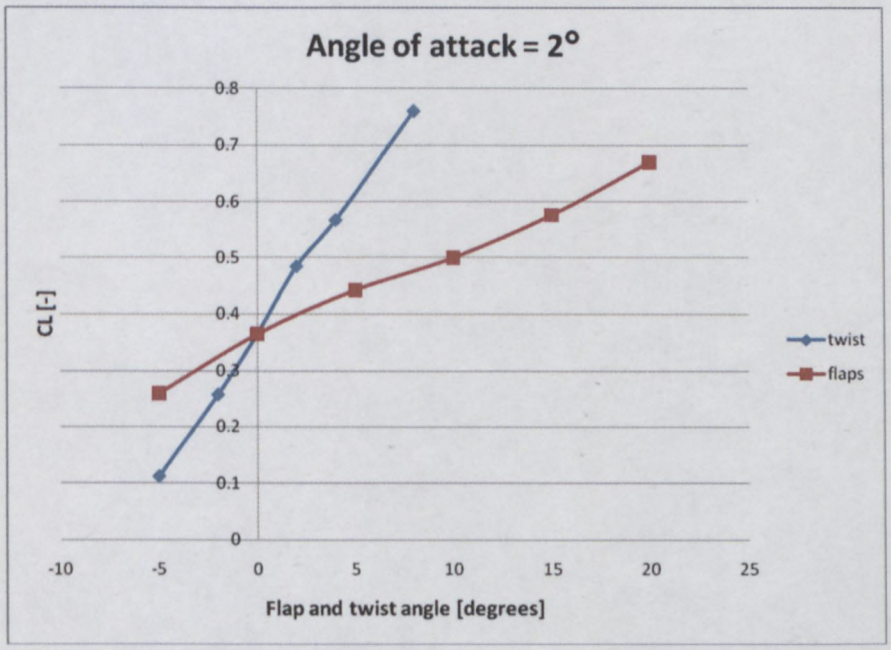

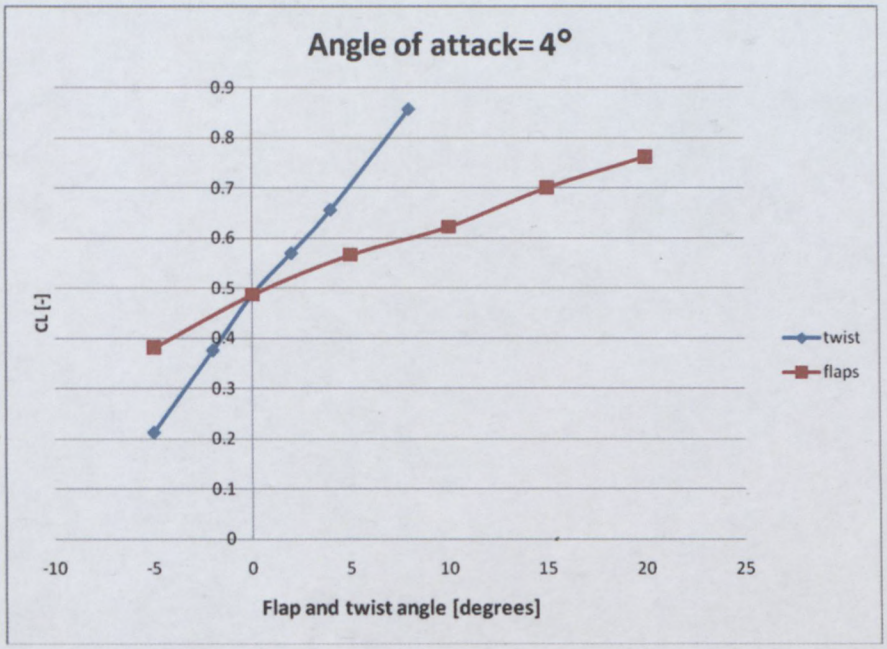
Angle of attack= 4°
CL [-]
0.9
0.8
0.7
0.6
0.5
0.4
0.3
0.2
0.1
0
-10
-5
0
5
10
15
20
25
Flap and twist angle [degrees]
twist
flaps

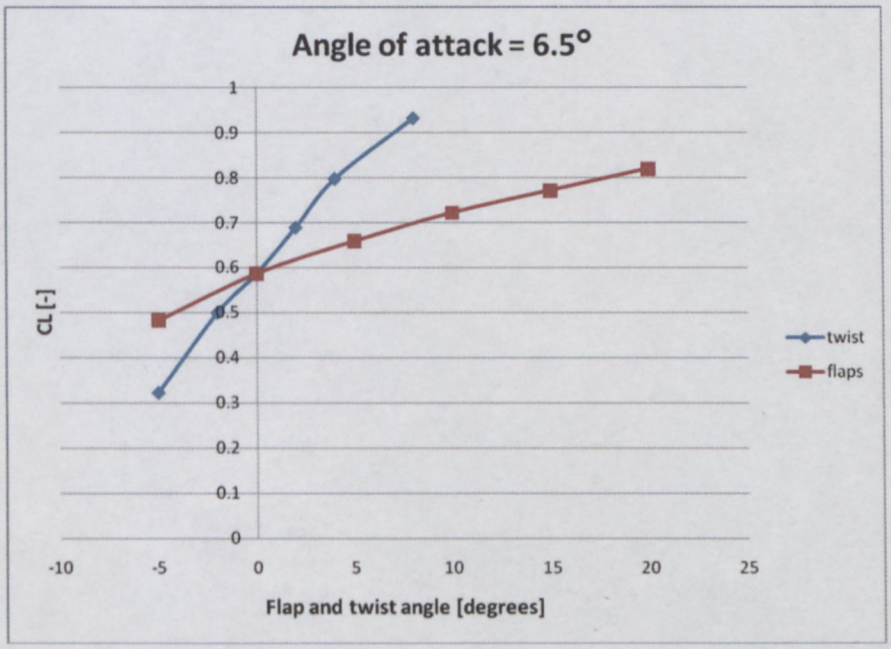
Angle of attack = 6.5°
CL [-]
1
0.9
0.8
0.7
0.6
0.5
0.4
0.3
0.2
0.1
0
-10
-5
0
5
10
15
20
25
Flap and twist angle [degrees]
twist
flaps

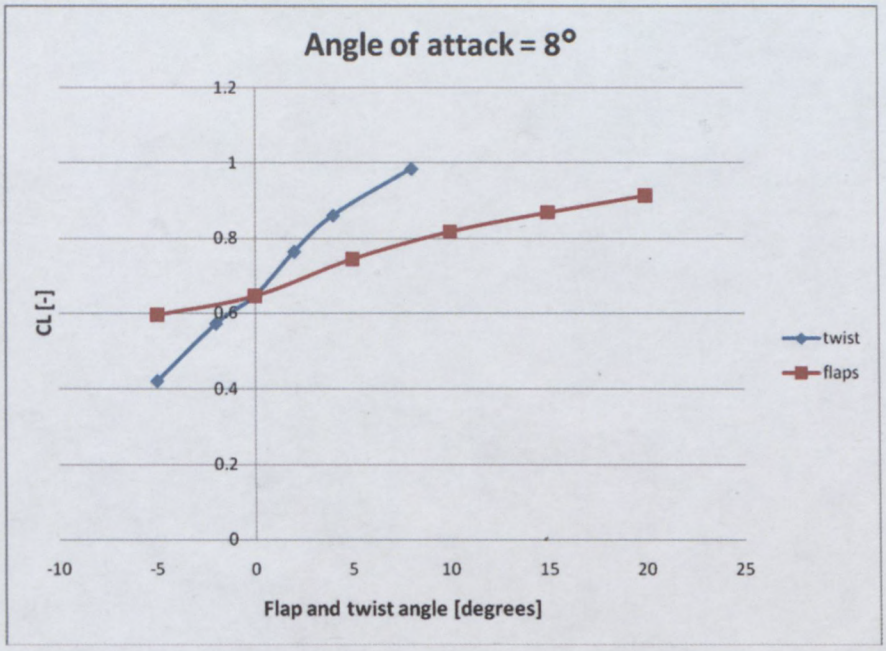
Angle of attack = 8°
1.2
1
0.8
0.6
0.4
0.2
0
CL [-]
-10
-5
0
5
10
15
20
25
Flap and twist angle [degrees]
twist
flaps

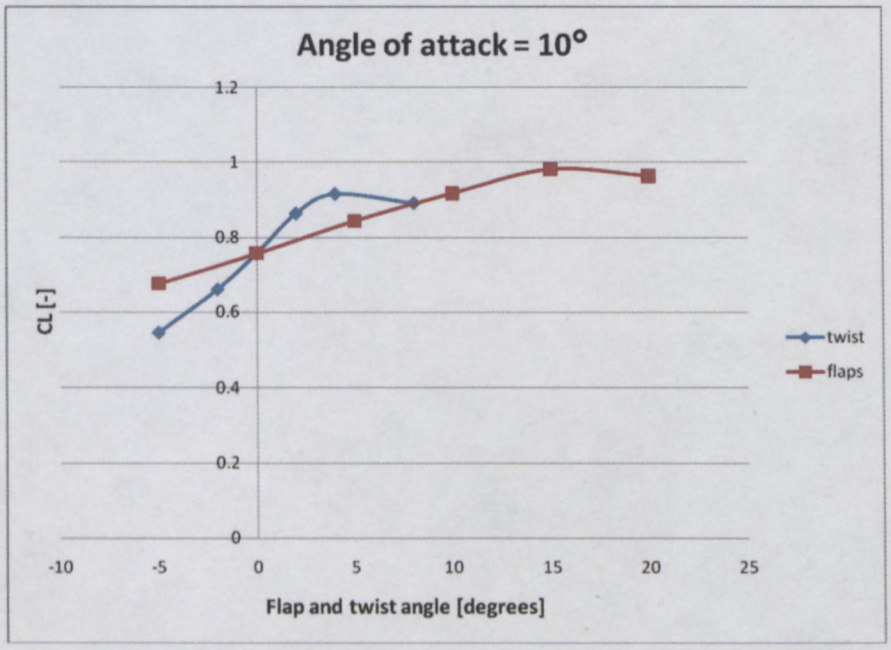
Angle of attack = 10°
1.2
1
0.8
0.6
0.4
0.2
0
CL [-]
-10
-5
0
5
10
15
20
25
Flap and twist angle [degrees]
twist
flaps

V=18m/s

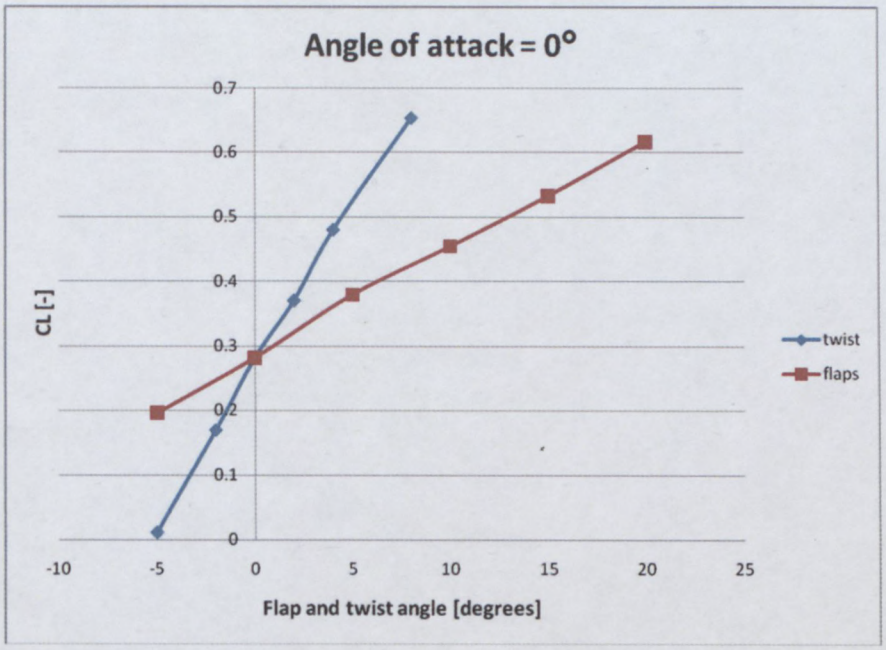
Angle of attack = 0°
0.7
0.6
0.5
0.4
0.3
0.2
0.1
0
CL [-]
-10
-5
0
5
10
15
20
25
Flap and twist angle [degrees]
twist
flaps

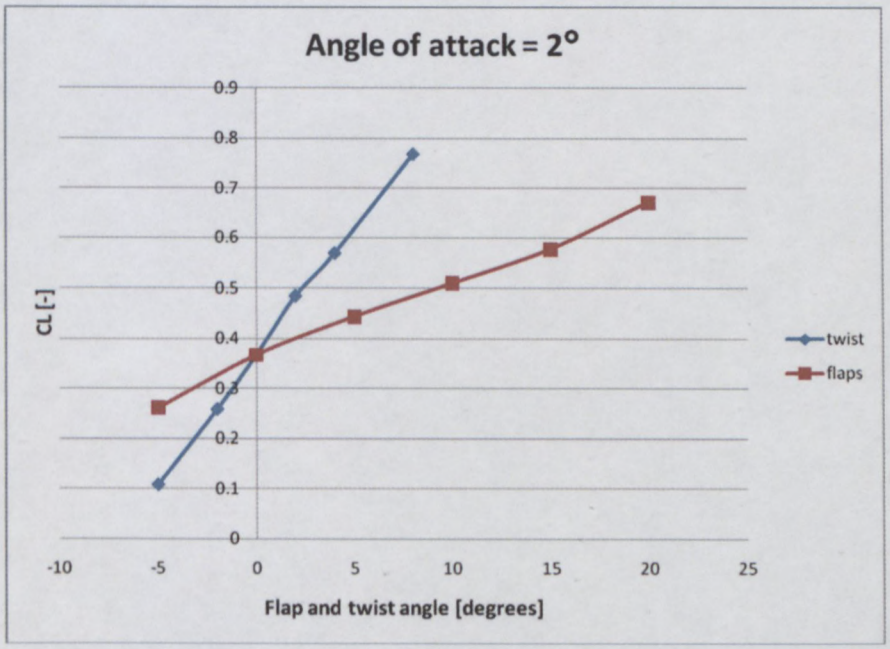
Angle of attack = 2°
0.9
0.8
0.7
0.6
0.5
0.4
0.3
0.2
0.1
0
CL [-]
-10
-5
0
5
10
15
20
25
Flap and twist angle [degrees]
twist
flaps

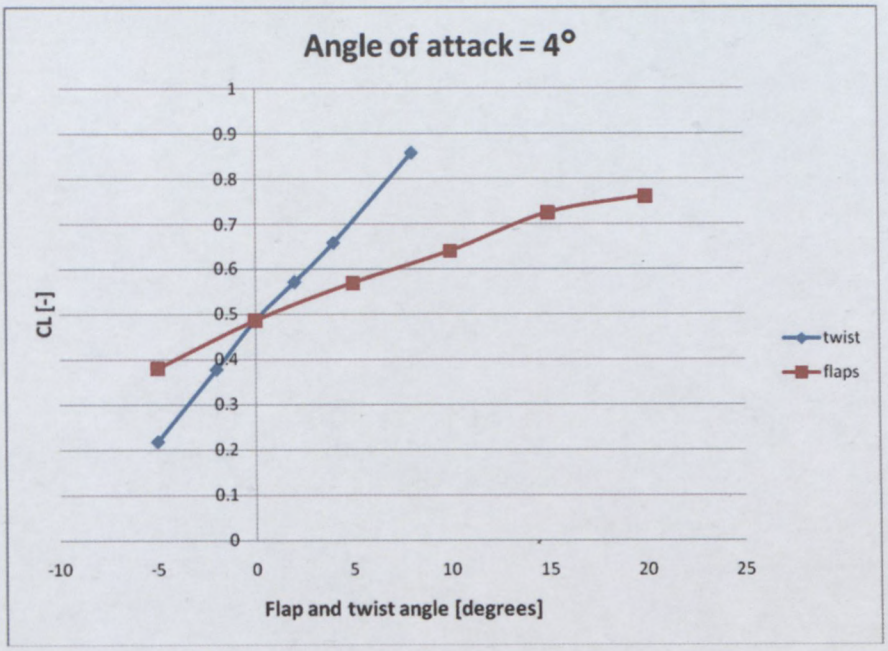
Angle of attack = 4°
CL [-]
1
0.9
0.8
0.7
0.6
0.5
0.4
0.3
0.2
0.1
0
-10
-5
0
5
10
15
20
25
Flap and twist angle [degrees]
twist
flaps

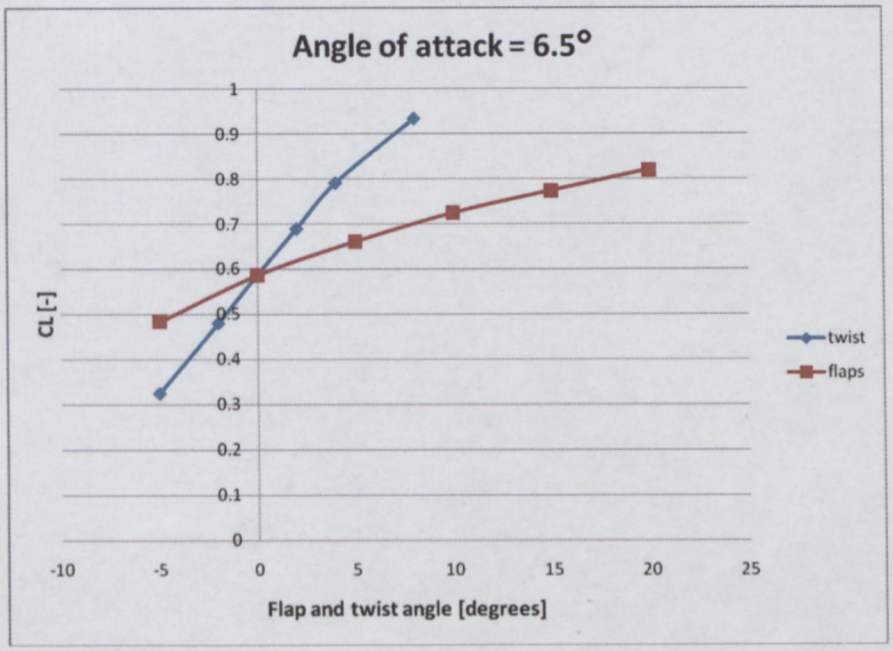
Angle of attack = 6.5°
CL [-]
1
0.9
0.8
0.7
0.6
0.5
0.4
0.3
0.2
0.1
0
-10
-5
0
5
10
15
20
25
Flap and twist angle [degrees]
twist
flaps

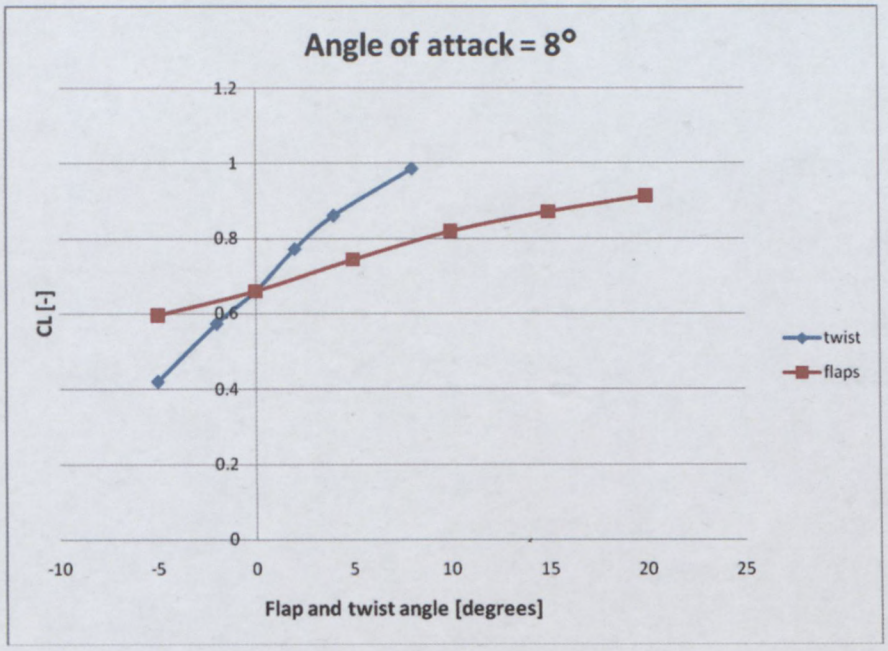
Angle of attack = 8°
1.2
1
0.8
0.6
0.4
0.2
0
CL [-]
-10
-5
0
5
10
15
20
25
Flap and twist angle [degrees]
twist
flaps

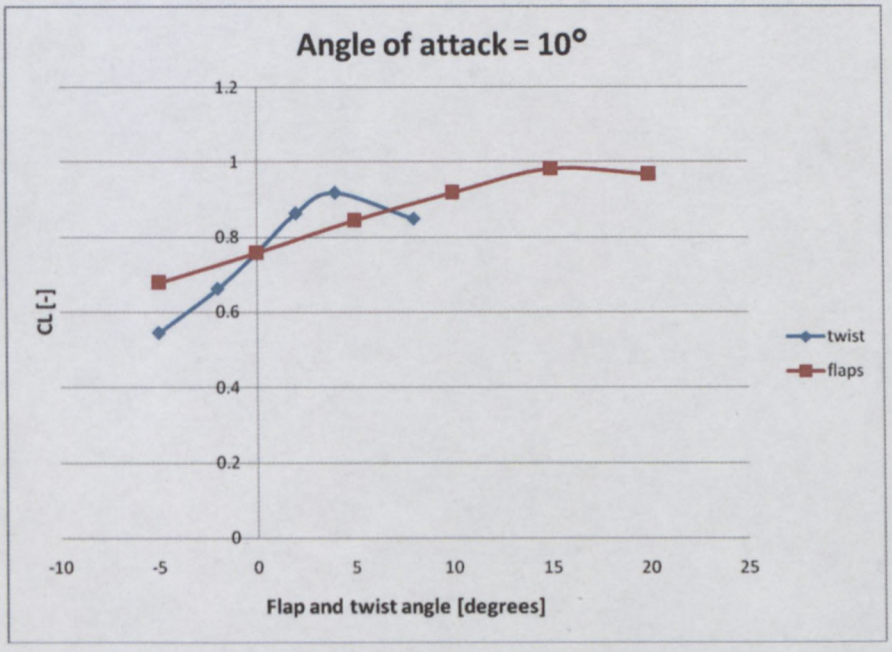
Angle of attack = 10°
1.2
1
0.8
0.6
0.4
0.2
0
CL [-]
-10
-5
0
5
10
15
20
25
Flap and twist angle [degrees]
twist
flaps

V=22.22m/s

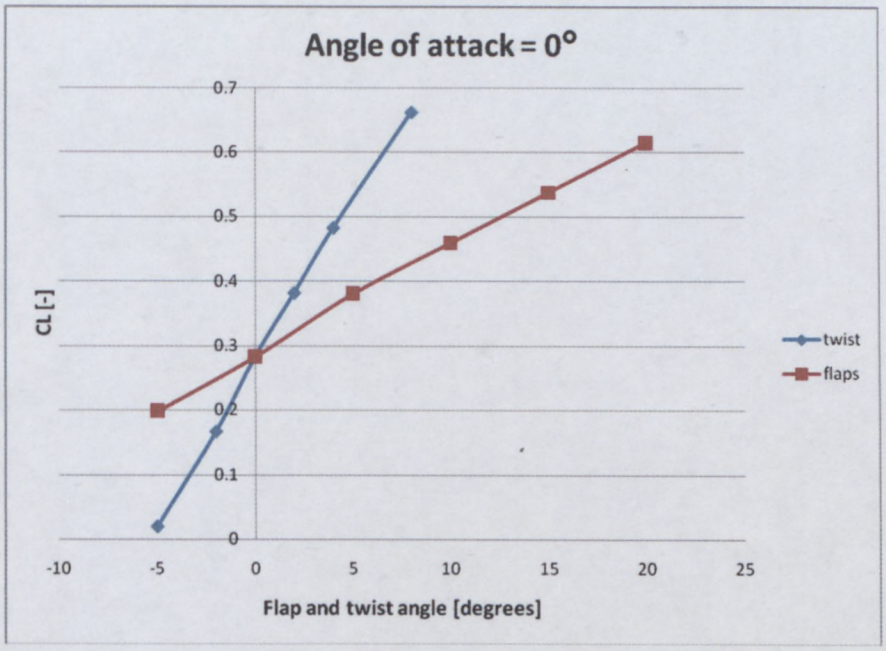
Angle of attack = 0°
CL [-]
0.7
0.6
0.5
0.4
0.3
0.2
0.1
0
-10
-5
0
5
10
15
20
25
Flap and twist angle [degrees]
twist
flaps

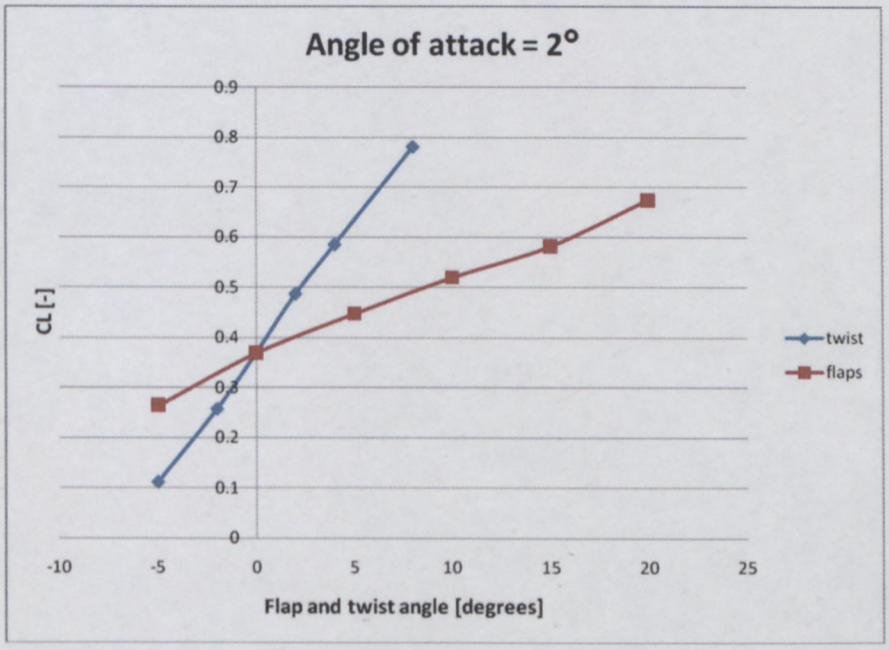
Angle of attack = 2°
CL [-]
0.9
0.8
0.7
0.6
0.5
0.4
0.3
0.2
0.1
0
-10
-5
0
5
10
15
20
25
Flap and twist angle [degrees]
twist
flaps

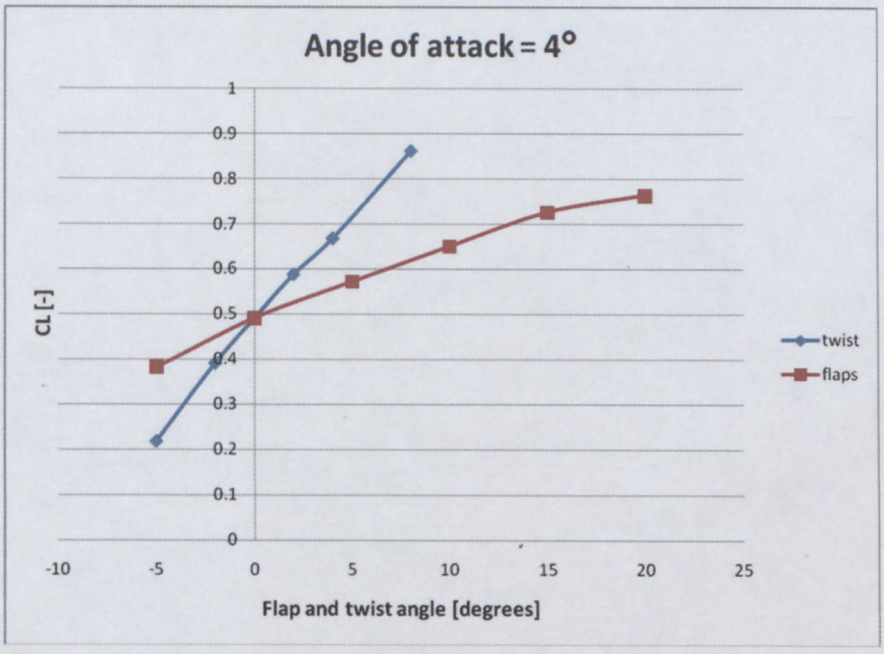
Angle of attack = 4°
CL [-]
1
0.9
0.8
0.7
0.6
0.5
0.4
0.3
0.2
0.1
0
-10
-5
0
5
10
15
20
25
Flap and twist angle [degrees]
twist
flaps

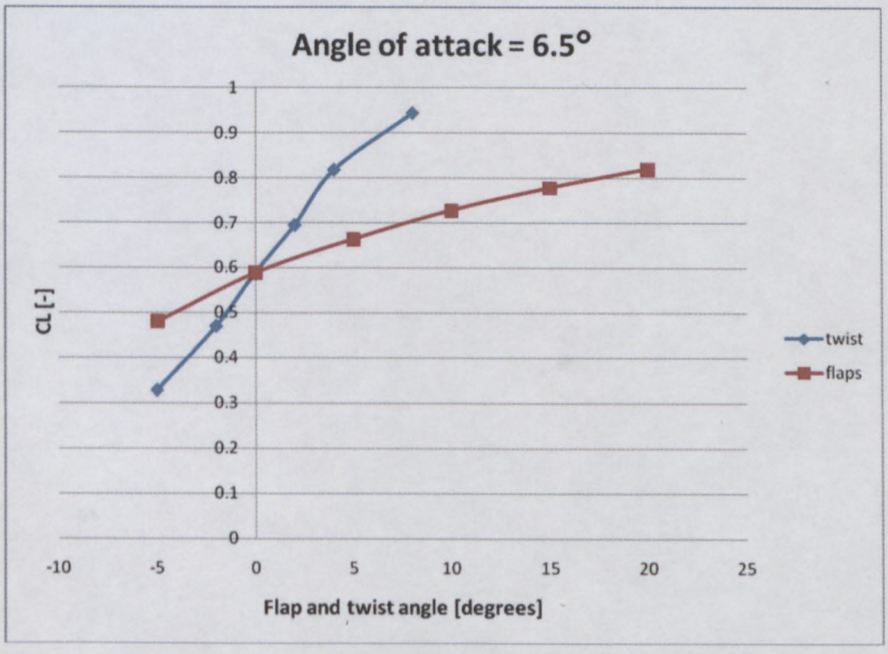
Angle of attack = 6.5°
CL [-]
1
0.9
0.8
0.7
0.6
0.5
0.4
0.3
0.2
0.1
0
-10
-5
0
5
10
15
20
25
Flap and twist angle [degrees]
twist
flaps

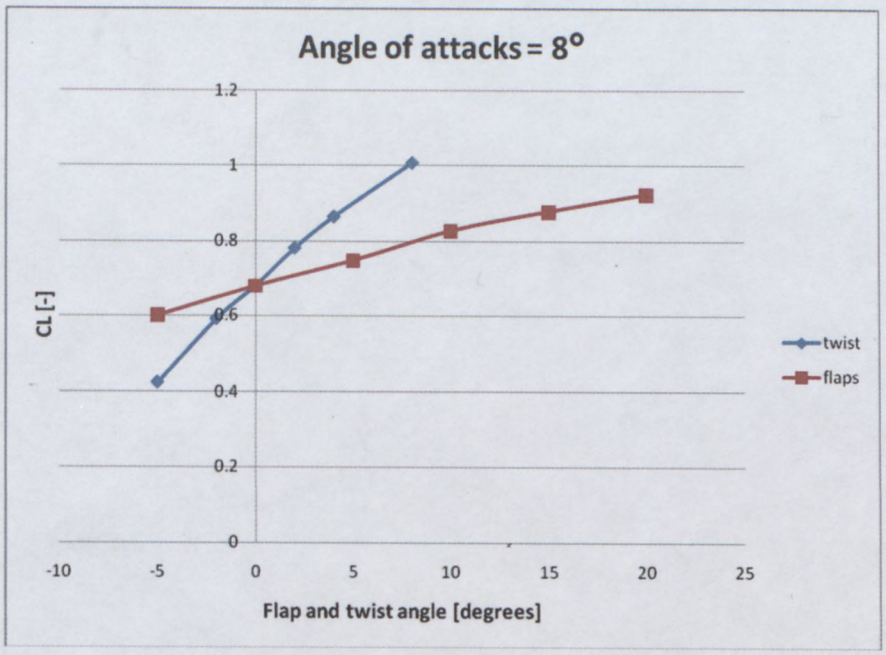
Angle of attacks = 8°
1.2
1
0.8
0.6
0.4
0.2
0
CL [-]
-10
-5
0
5
10
15
20
25
Flap and twist angle [degrees]
twist
flaps

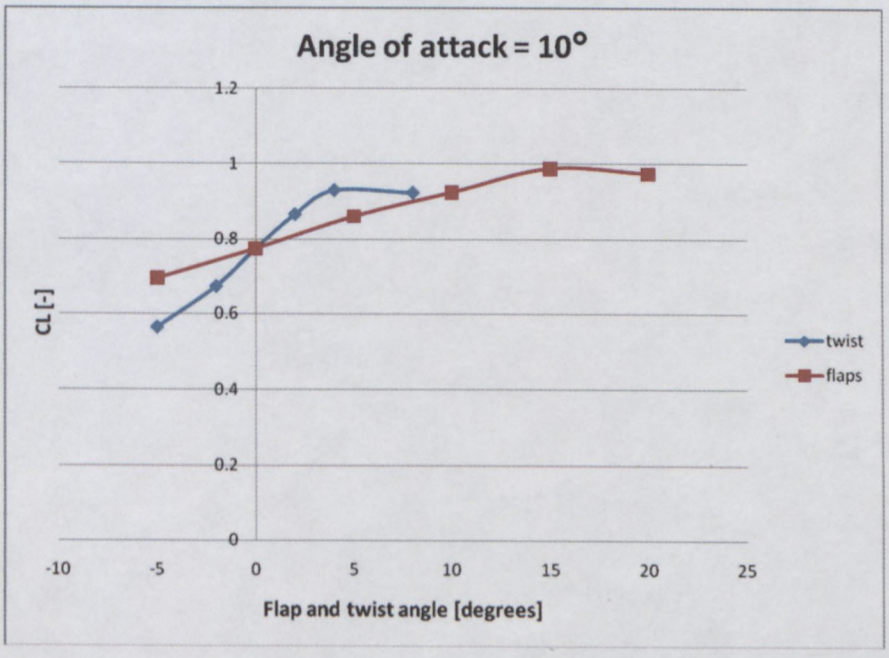
Angle of attack = 10°
1.2
1
0.8
0.6
0.4
0.2
0
CL [-]
-10
-5
0
5
10
15
20
25
Flap and twist angle [degrees]
twist
flaps

V=33.33m/s

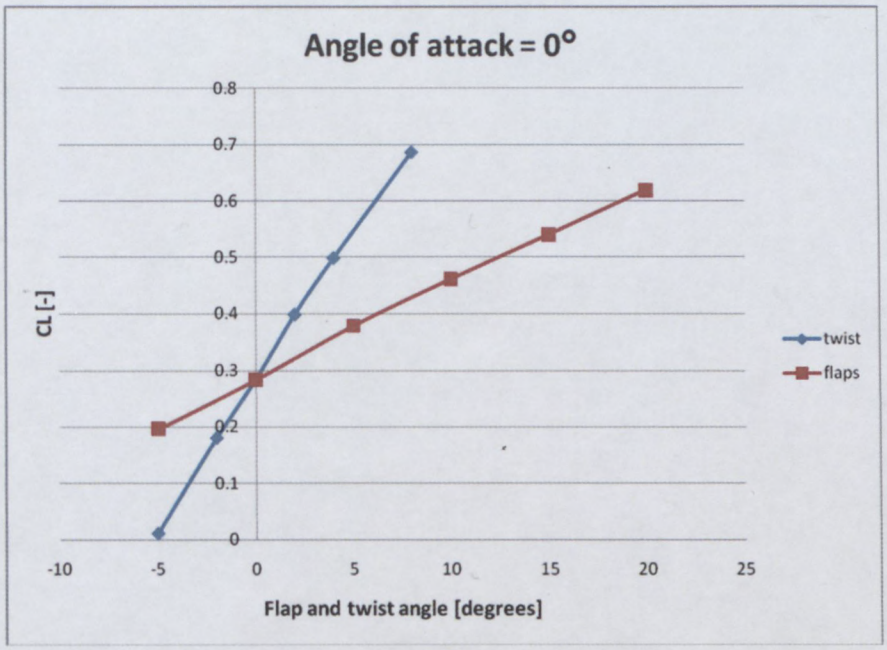
Angle of attack = 0°
0.8
0.7
0.6
0.5
0.4
0.3
0.2
0.1
0
CL [-]
-10
-5
0
5
10
15
20
25
Flap and twist angle [degrees]
twist
flaps

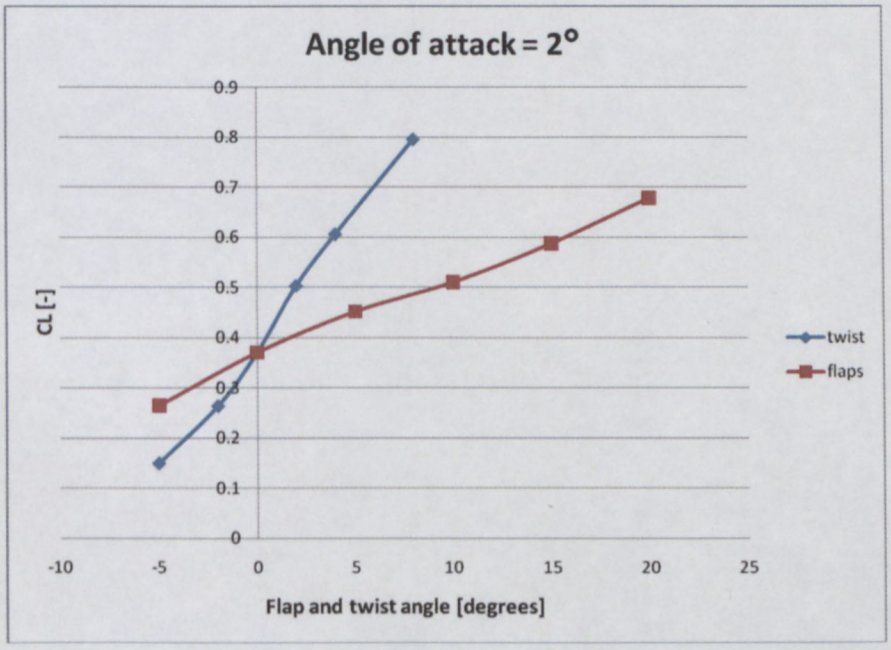
Angle of attack = 2°
0.9
0.8
0.7
0.6
0.5
0.4
0.3
0.2
0.1
0
CL [-]
-10
-5
0
5
10
15
20
25
Flap and twist angle [degrees]
twist
flaps

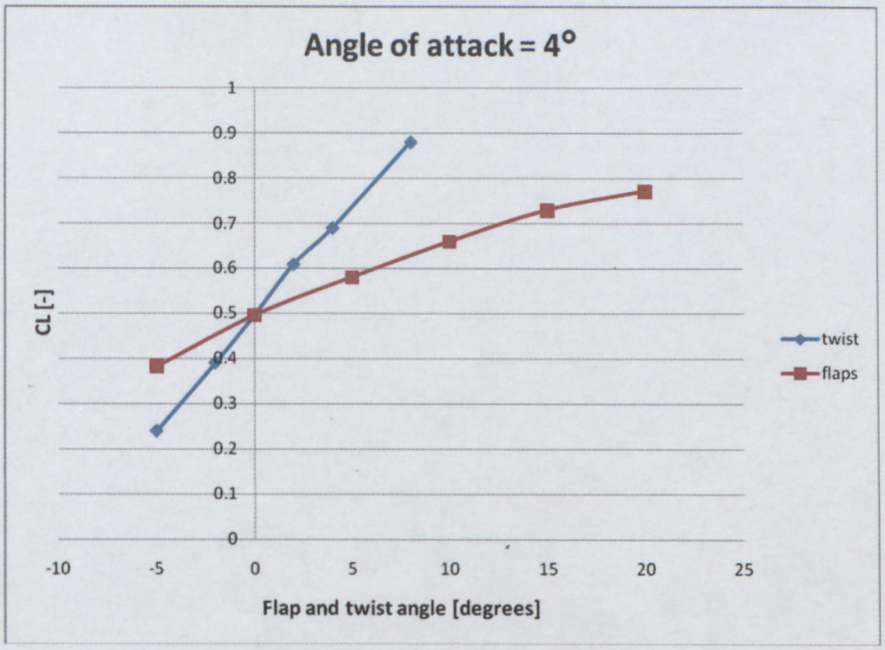
Angle of attack = 4°
1
0.9
0.8
0.7
0.6
0.5
0.4
0.3
0.2
0.1
0
CL [-]
-10
-5
0
5
10
15
20
25
Flap and twist angle [degrees]
twist
flaps

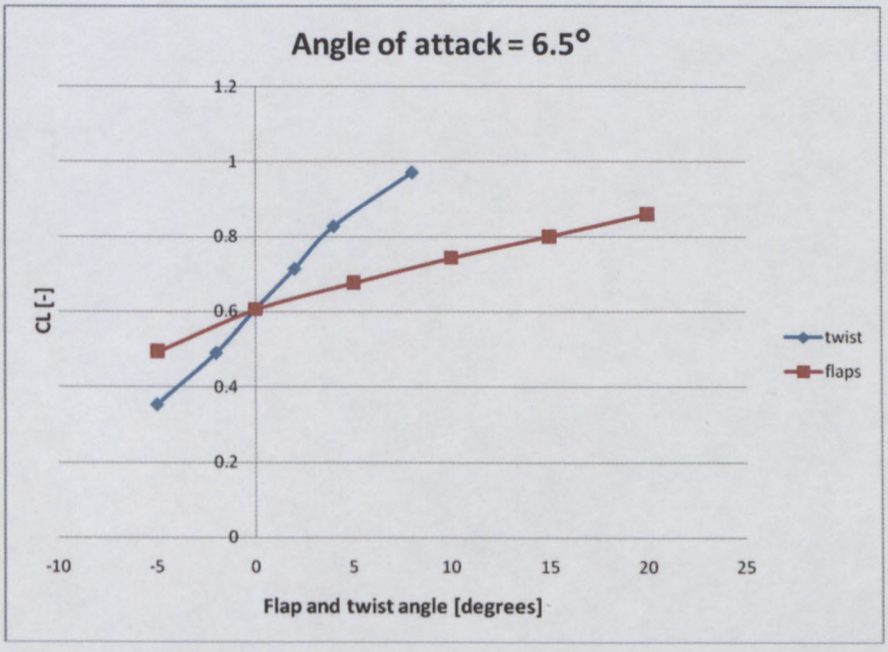
Angle of attack = 6.5°
1.2
1
0.8
0.6
0.4
0.2
0
CL [-]
-10
-5
0
5
10
15
20
25
Flap and twist angle [degrees]
twist
flaps

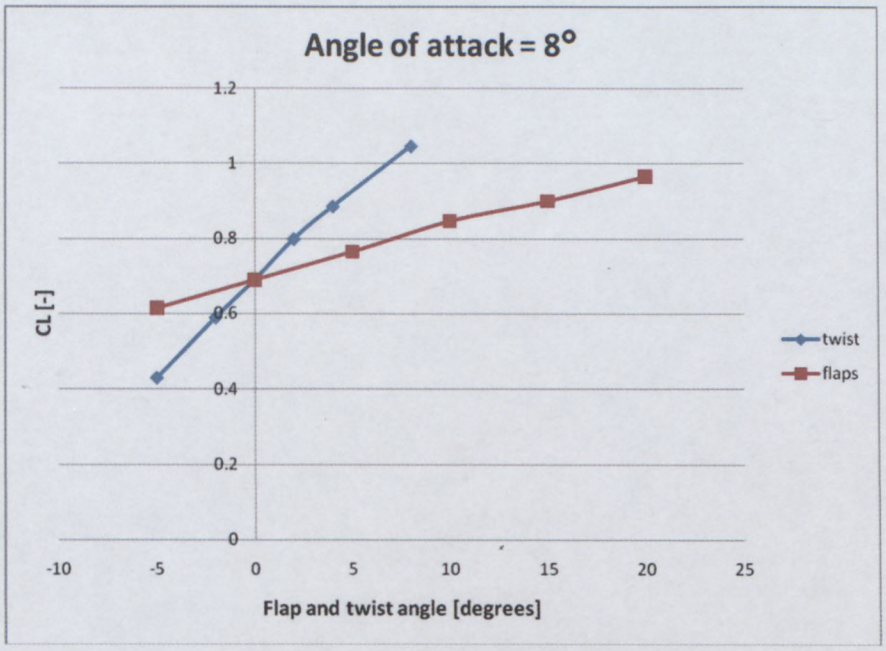
Angle of attack = 8°
1.2
1
0.8
0.6
0.4
0.2
0
CL [-]
-10
-5
0
5
10
15
20
25
Flap and twist angle [degrees]
twist
flaps

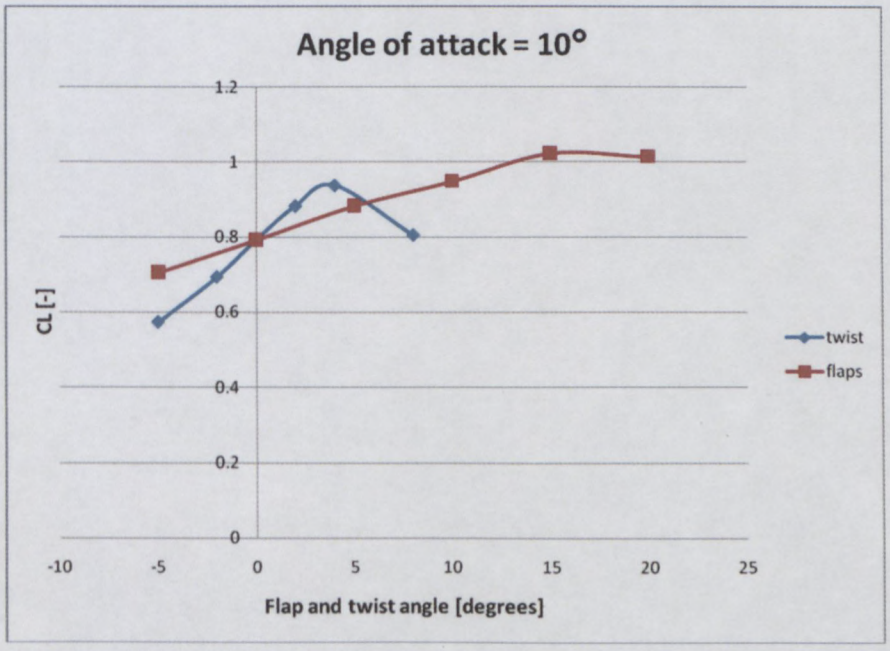
Angle of attack = 10°
1.2
1
0.8
0.6
0.4
0.2
0
CL [-]
-10
-5
0
5
10
15
20
25
Flap and twist angle [degrees]
twist
flaps

COEFFICIENT OF DRAG (CD) VS FLAP AND TWIST ANGLE

V=16.667m/s

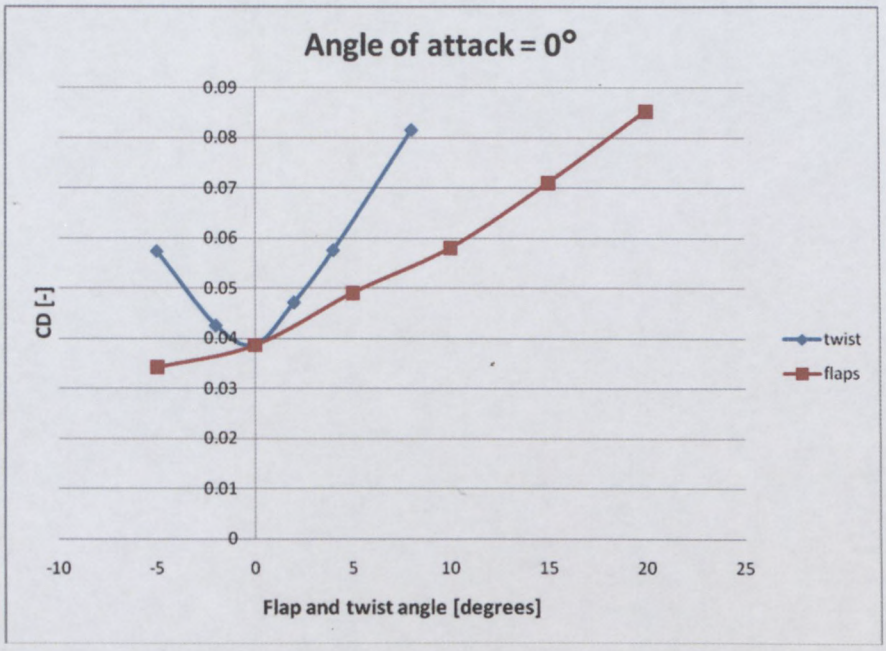

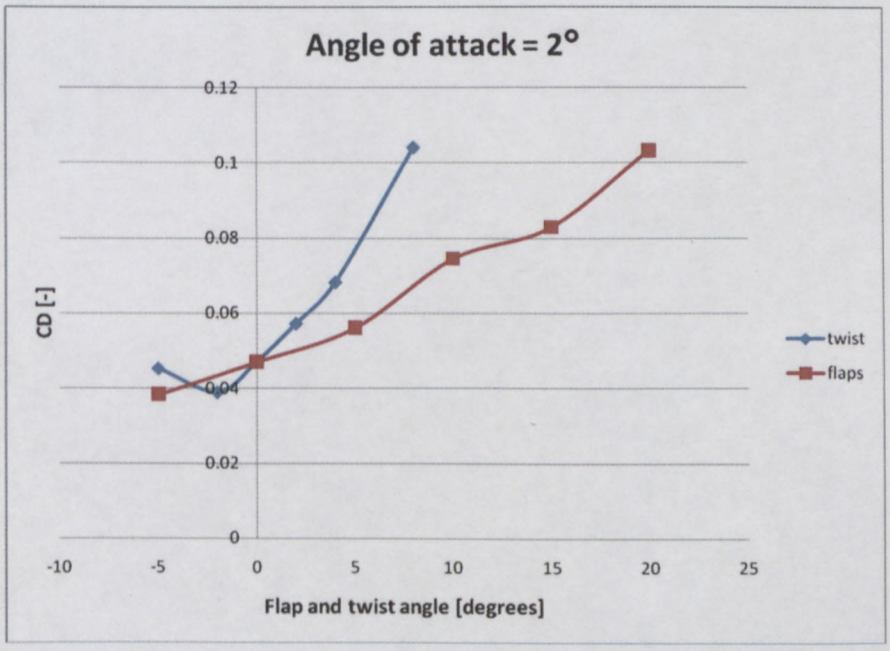

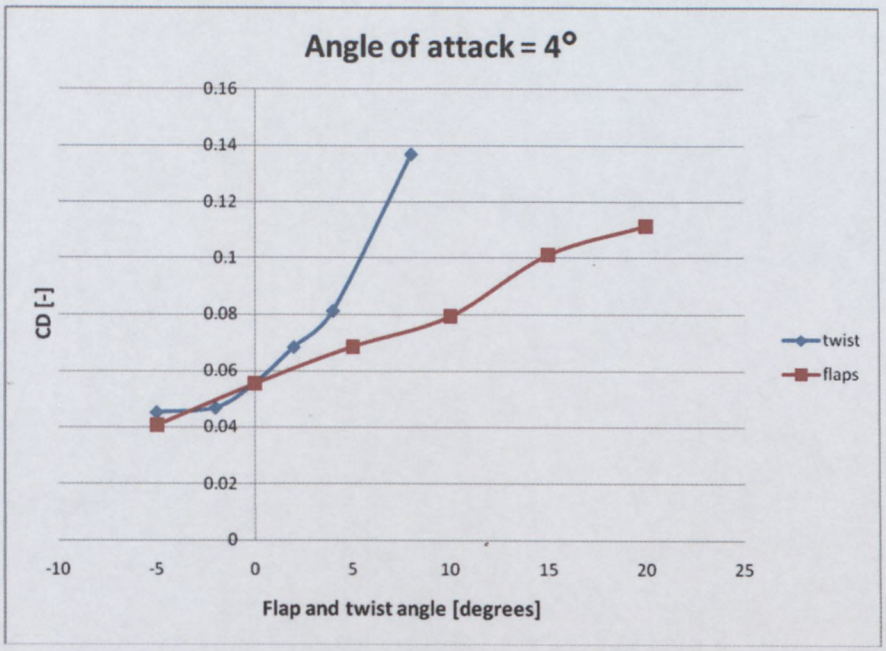
Angle of attack = 4°
0.16
0.14
0.12
0.1
0.08
0.06
0.04
0.02
0
CD [-]
-10
-5
0
5
10
15
20
25
Flap and twist angle [degrees]
twist
flaps

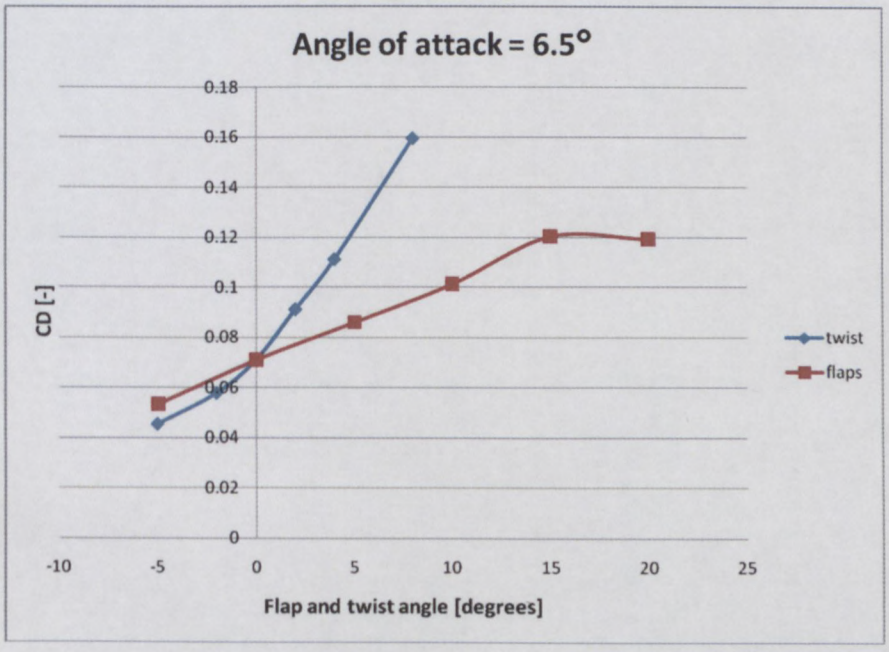
Angle of attack = 6.5°
0.18
0.16
0.14
0.12
0.1
0.08
0.06
0.04
0.02
0
CD [-]
-10
-5
0
5
10
15
20
25
Flap and twist angle [degrees]
twist
flaps

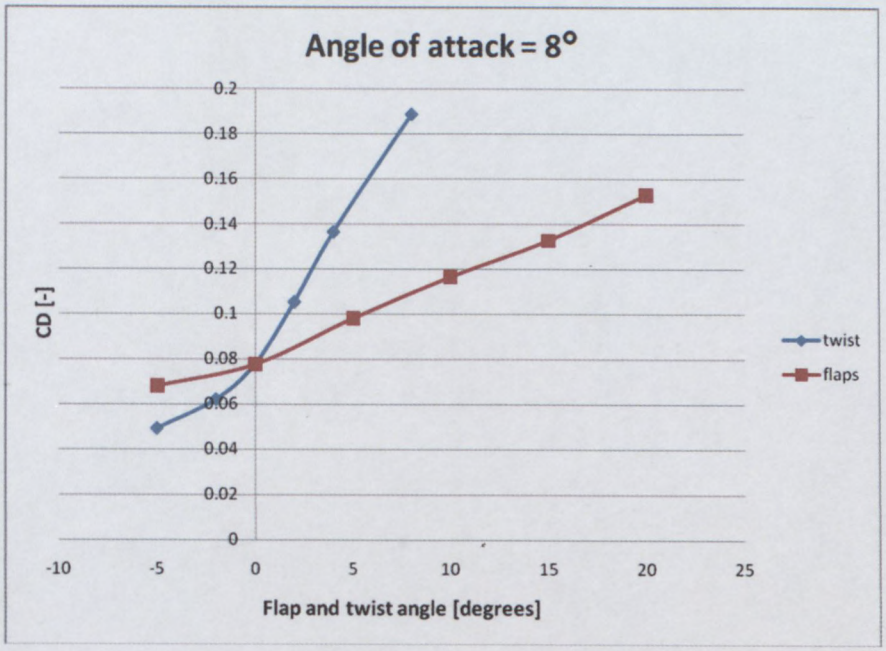
Angle of attack = 8°
CD [-]
0.2
0.18
0.16
0.14
0.12
0.1
0.08
0.06
0.04
0.02
0
-10
-5
0
5
10
15
20
25
Flap and twist angle [degrees]
twist
flaps

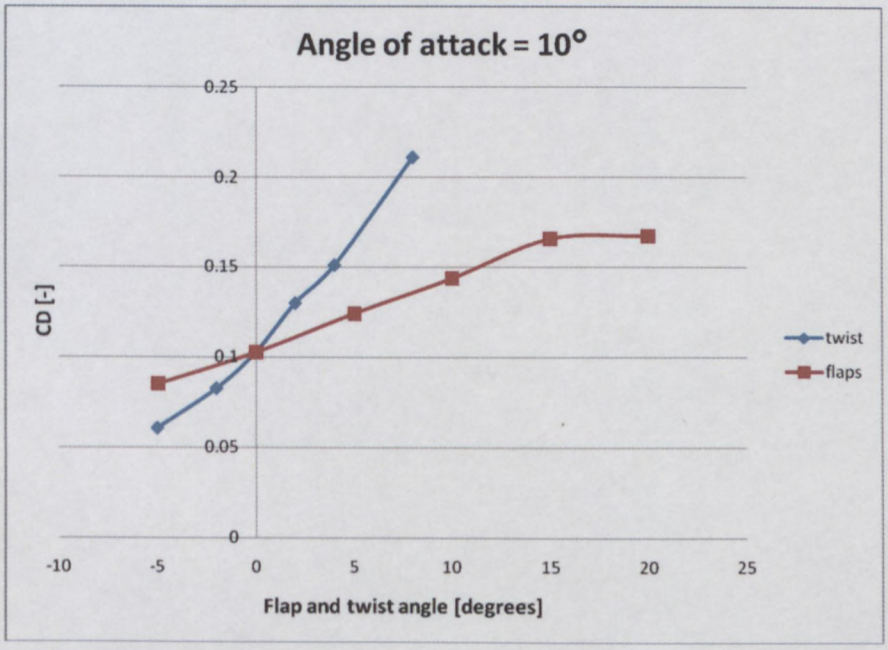
Angle of attack = 10°
CD [-]
0.25
0.2
0.15
0.1
0.05
0
-10
-5
0
5
10
15
20
25
Flap and twist angle [degrees]
twist
flaps

V=18m/s

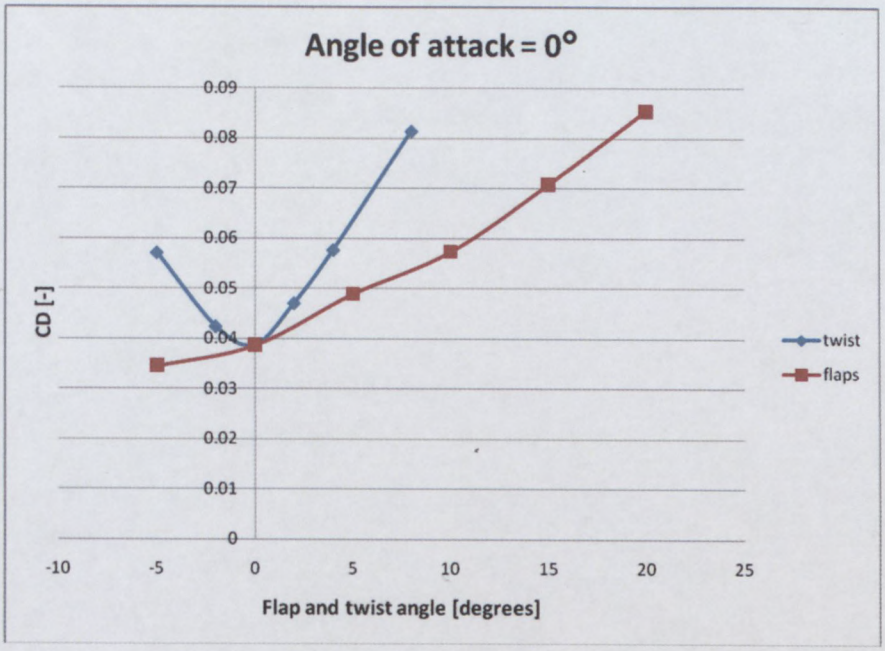
Angle of attack = 0°
CD [-]
0.09
0.08
0.07
0.06
0.05
0.04
0.03
0.02
0.01
0
-10
-5
0
5
10
15
20
25
Flap and twist angle [degrees]
twist
flaps

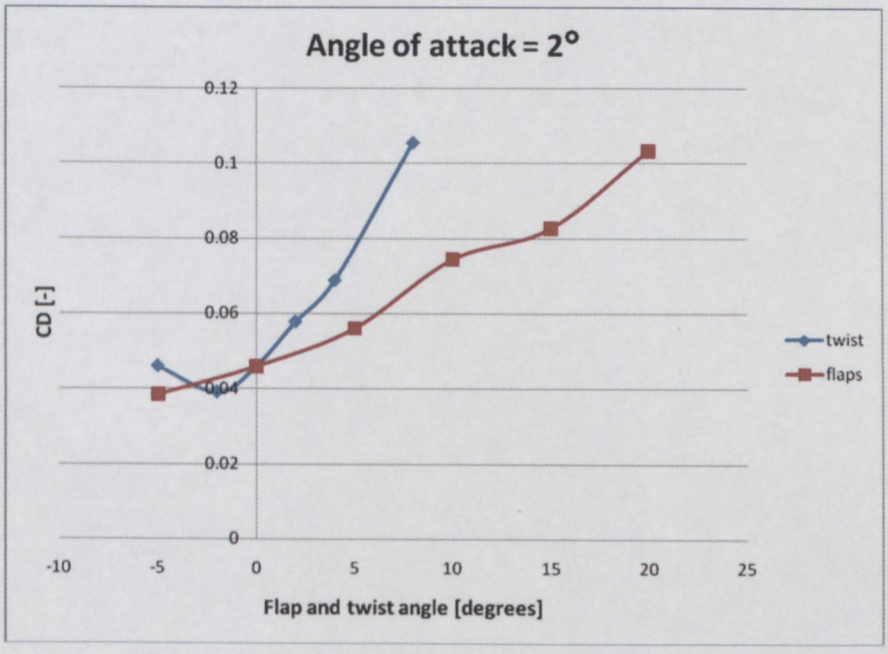
Angle of attack = 2°
CD [-]
0.12
0.1
0.08
0.06
0.04
0.02
0
-10
-5
0
5
10
15
20
25
Flap and twist angle [degrees]
twist
flaps

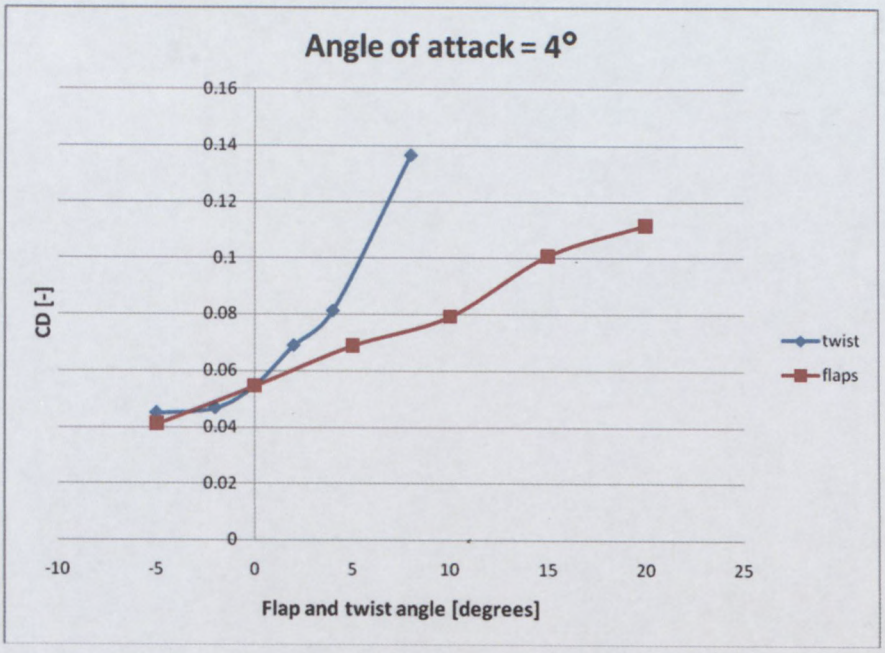
Angle of attack = 4°
0.16
0.14
0.12
0.1
0.08
0.06
0.04
0.02
0
CD [-]
-10
-5
0
5
10
15
20
25
Flap and twist angle [degrees]
twist
flaps

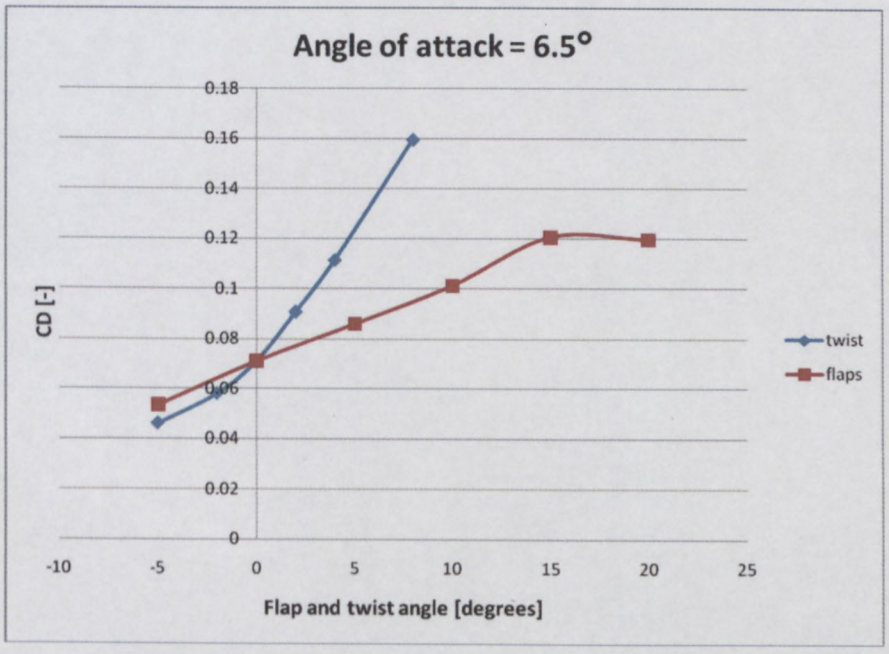
Angle of attack = 6.5°
0.18
0.16
0.14
0.12
0.1
0.08
0.06
0.04
0.02
0
CD [-]
-10
-5
0
5
10
15
20
25
Flap and twist angle [degrees]
twist
flaps

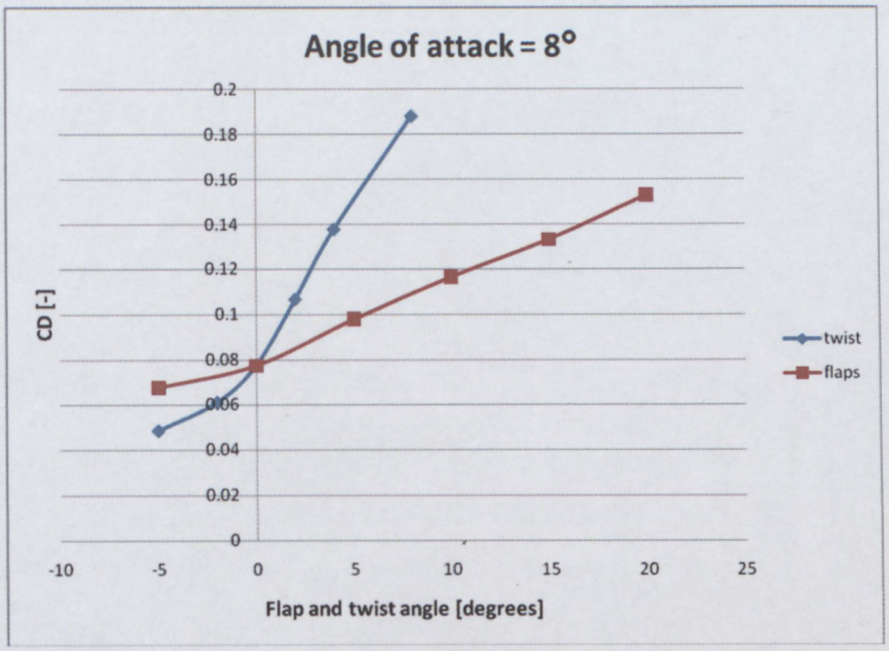
Angle of attack = 8°
CD [-]
0.2
0.18
0.16
0.14
0.12
0.1
0.08
0.06
0.04
0.02
0
-10
-5
0
5
10
15
20
25
Flap and twist angle [degrees]
twist
flaps

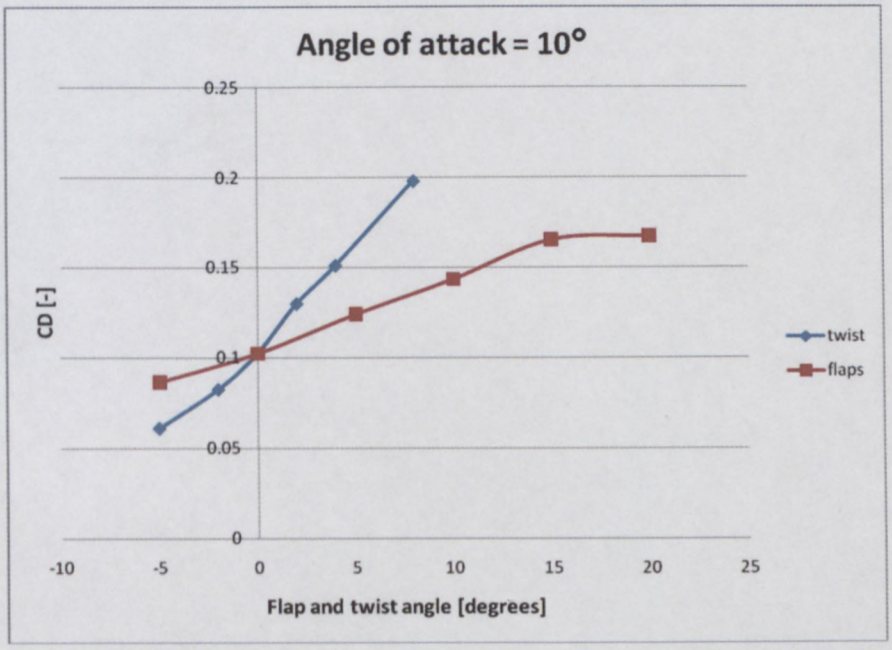
Angle of attack = 10°
CD [-]
0.25
0.2
0.15
0.1
0.05
0
-10
-5
0
5
10
15
20
25
Flap and twist angle [degrees]
twist
flaps

V = 22.22m/s

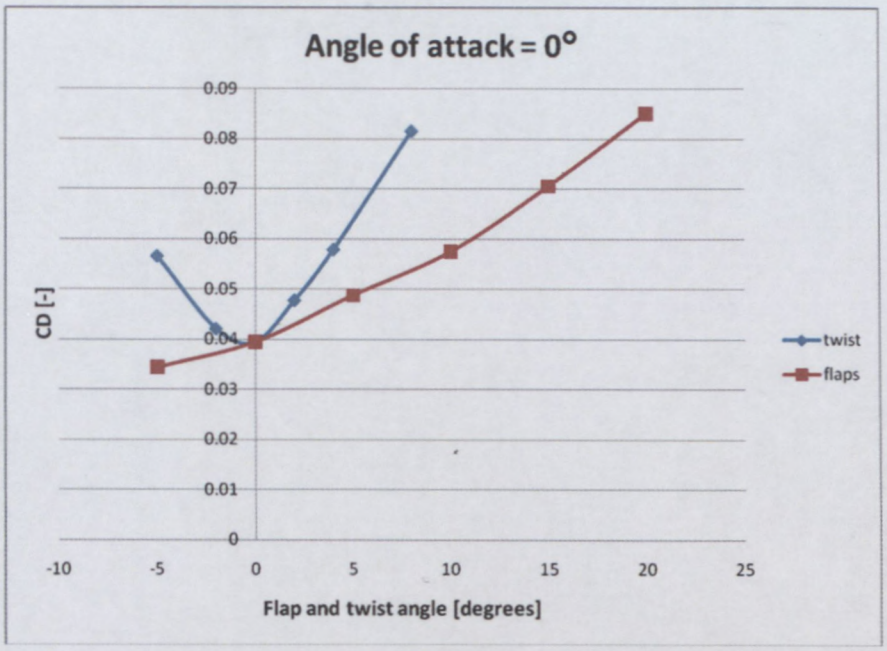
Angle of attack = 0°
CD [-]
0.09
0.08
0.07
0.06
0.05
0.04
0.03
0.02
0.01
0
-10
-5
0
5
10
15
20
25
Flap and twist angle [degrees]
twist
flaps

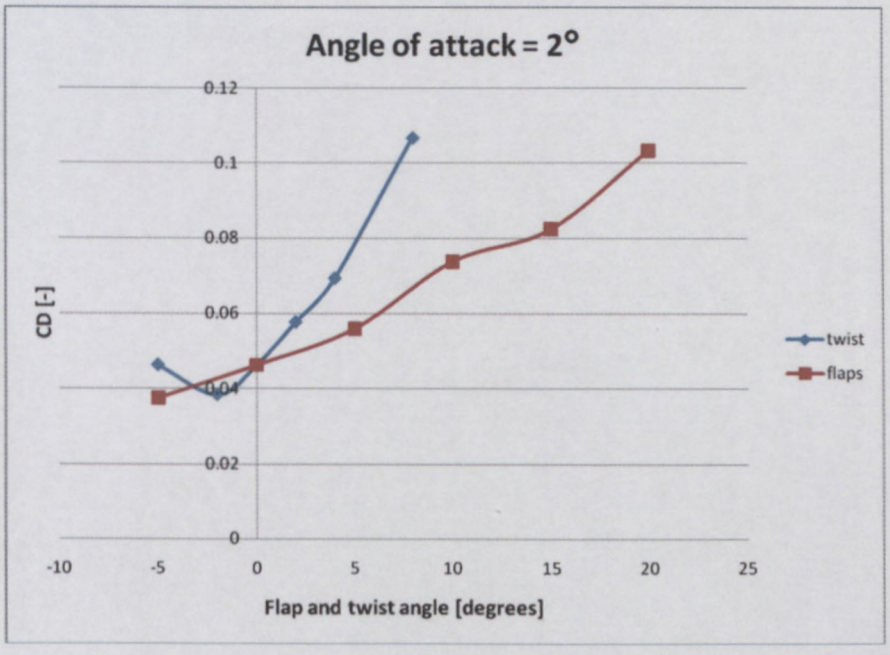
Angle of attack = 2°
CD [-]
0.12
0.1
0.08
0.06
0.04
0.02
0
-10
-5
0
5
10
15
20
25
Flap and twist angle [degrees]
twist
flaps

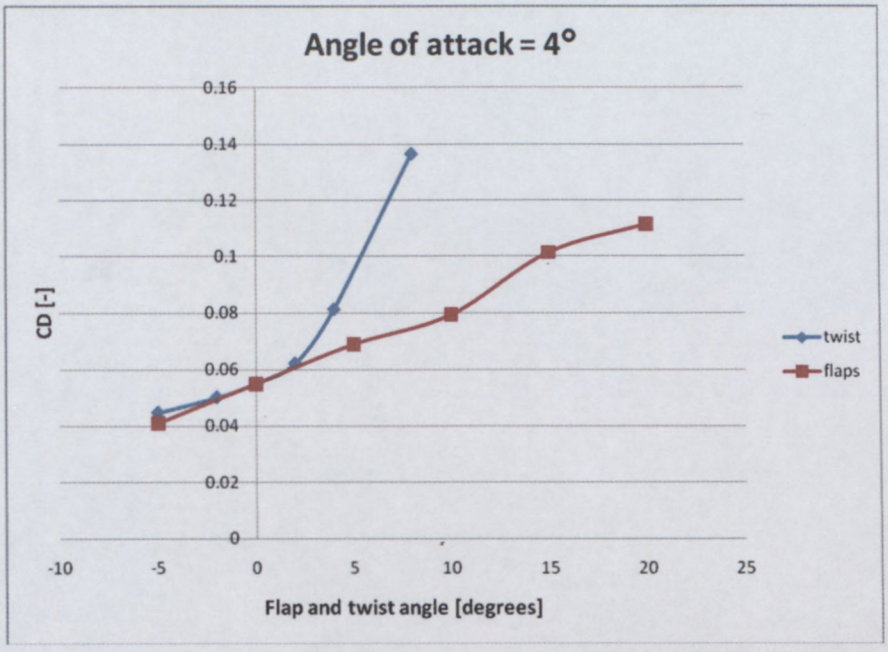
Angle of attack = 4°
0.16
0.14
0.12
0.1
0.08
0.06
0.04
0.02
0
CD [-]
-10
-5
0
5
10
15
20
25
Flap and twist angle [degrees]
twist
flaps

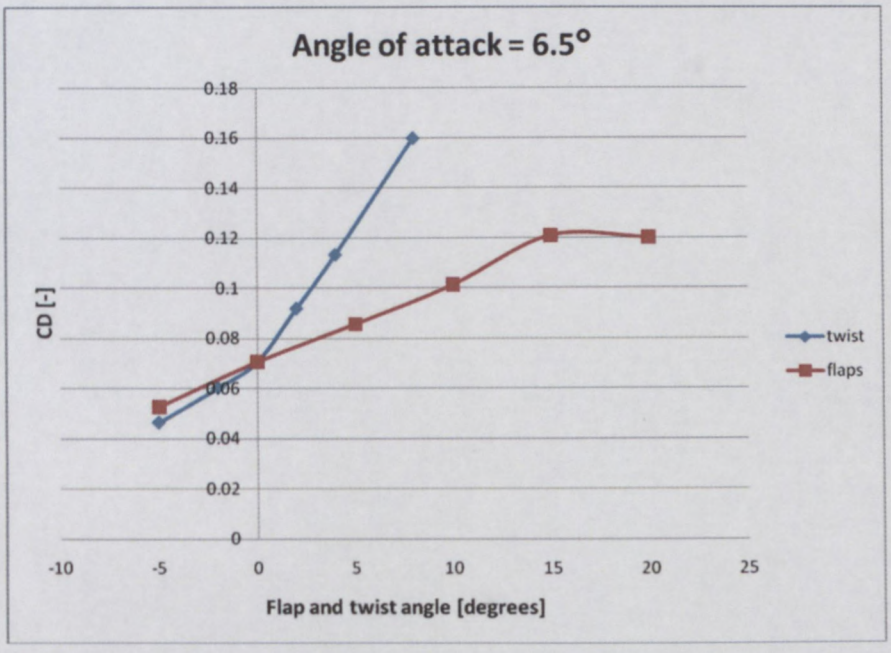
Angle of attack = 6.5°
0.18
0.16
0.14
0.12
0.1
0.08
0.06
0.04
0.02
0
CD [-]
-10
-5
0
5
10
15
20
25
Flap and twist angle [degrees]
twist
flaps

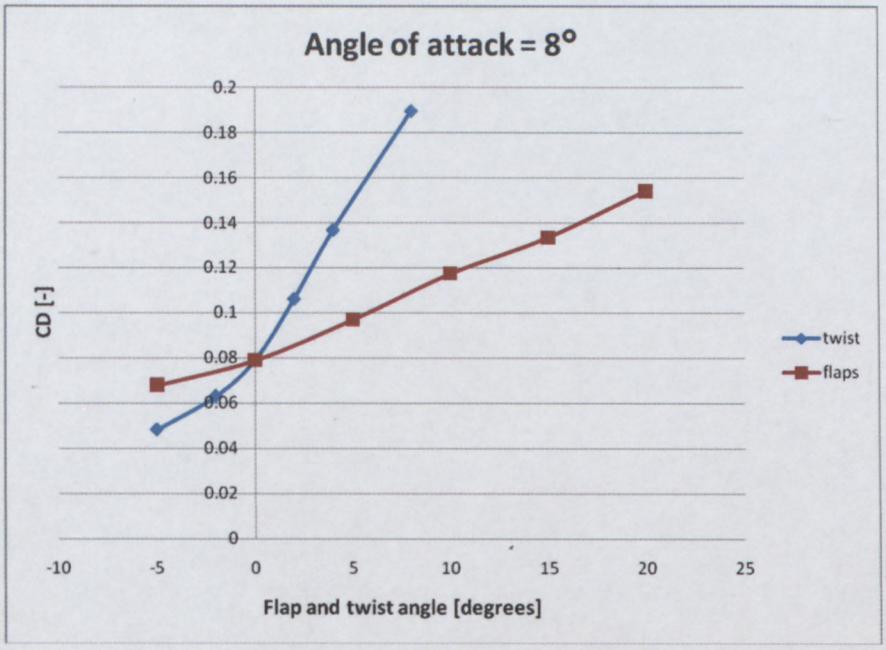
Angle of attack = 8°
CD [-]
0.2
0.18
0.16
0.14
0.12
0.1
0.08
0.06
0.04
0.02
0
-10
-5
0
5
10
15
20
25
Flap and twist angle [degrees]
twist
flaps

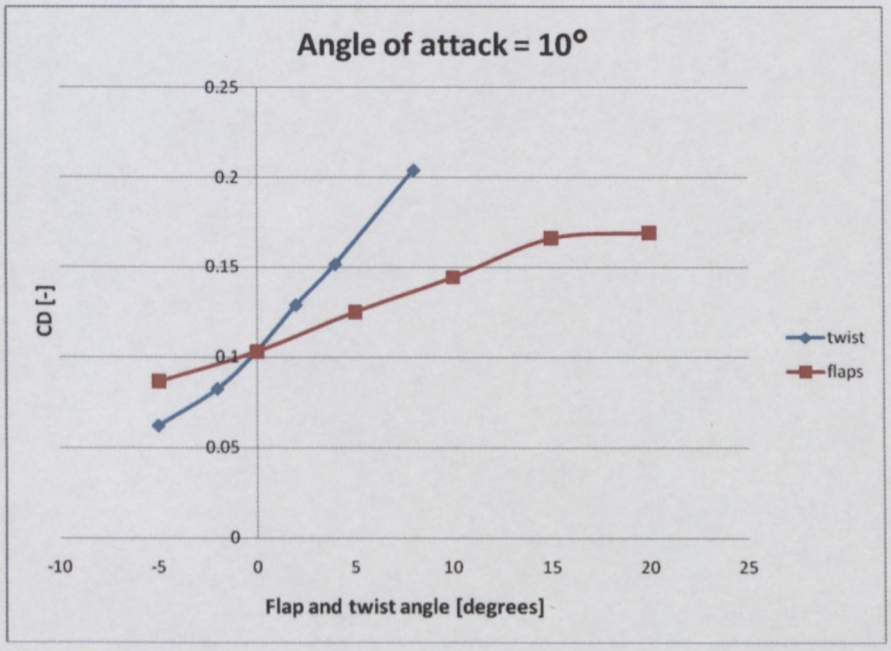
Angle of attack = 10°
CD [-]
0.25
0.2
0.15
0.1
0.05
0
-10
-5
0
5
10
15
20
25
Flap and twist angle [degrees]
twist
flaps

V = 33.33m/s

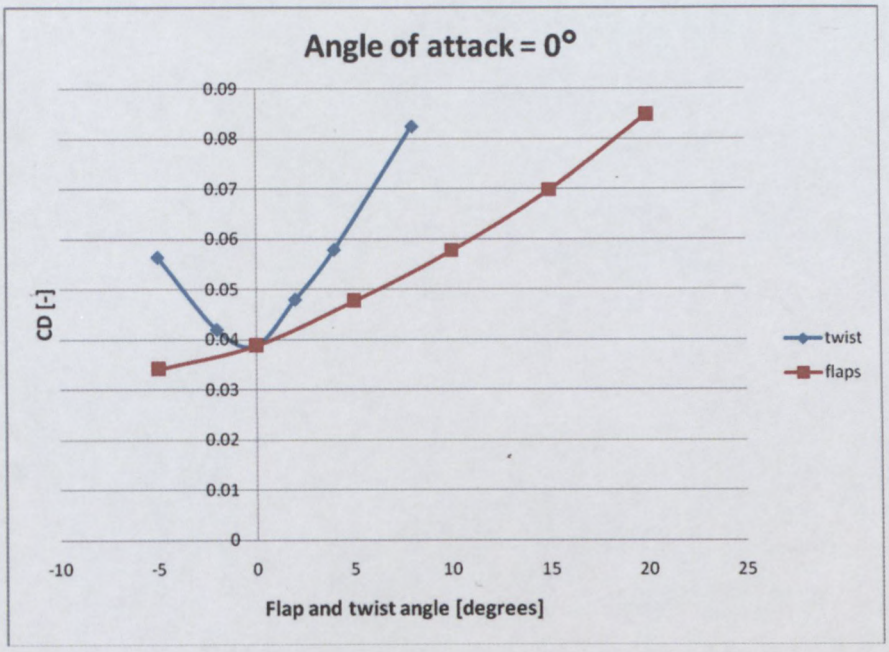
Angle of attack = 0°
CD [-]
0.09
0.08
0.07
0.06
0.05
0.04
0.03
0.02
0.01
0
-10
-5
0
5
10
15
20
25
Flap and twist angle [degrees]
twist
flaps

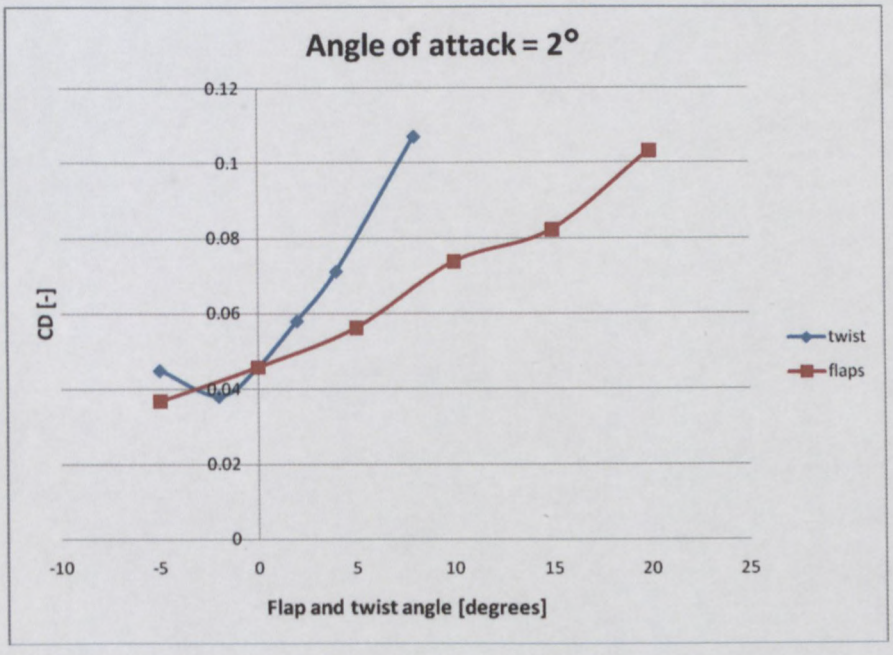
Angle of attack = 2°
CD [-]
0.12
0.1
0.08
0.06
0.04
0.02
0
-10
-5
0
5
10
15
20
25
Flap and twist angle [degrees]
twist
flaps

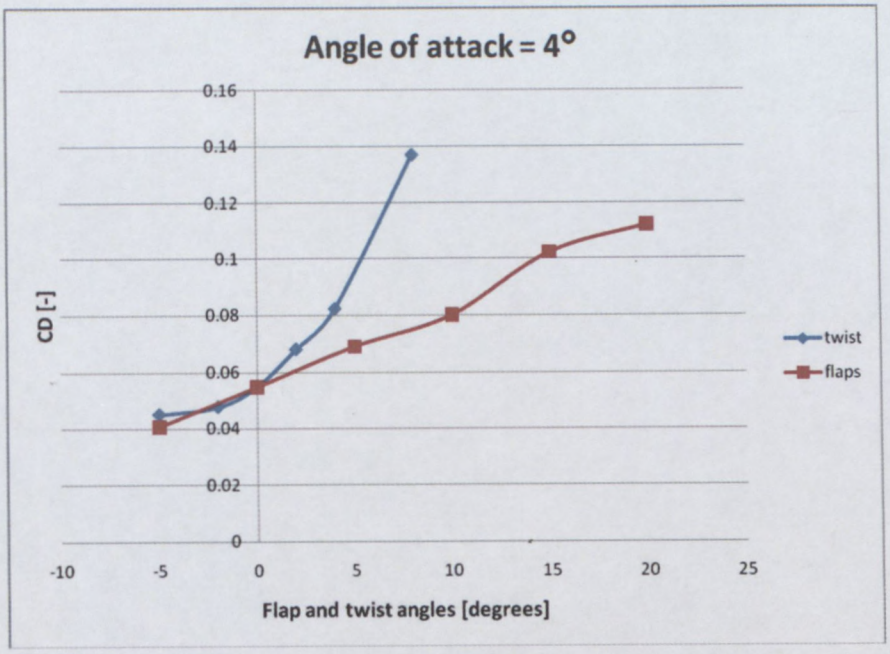
Angle of attack = 4°
0.16
0.14
0.12
0.1
0.08
0.06
0.04
0.02
0
CD [-]
-10
-5
0
5
10
15
20
25
Flap and twist angles [degrees]
twist
flaps

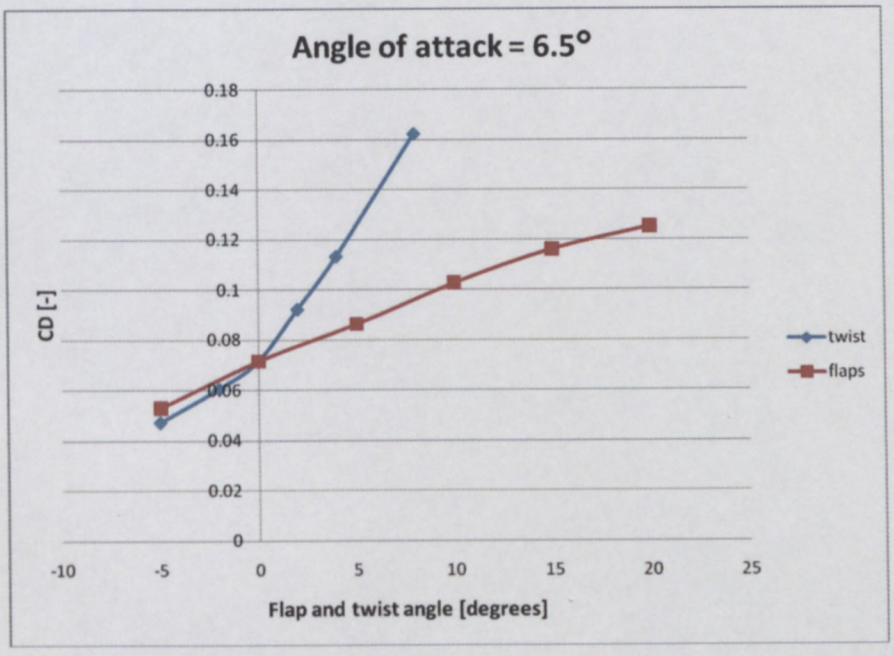
Angle of attack = 6.5°
0.18
0.16
0.14
0.12
0.1
0.08
0.06
0.04
0.02
0
CD [-]
-10
-5
0
5
10
15
20
25
Flap and twist angle [degrees]
twist
flaps

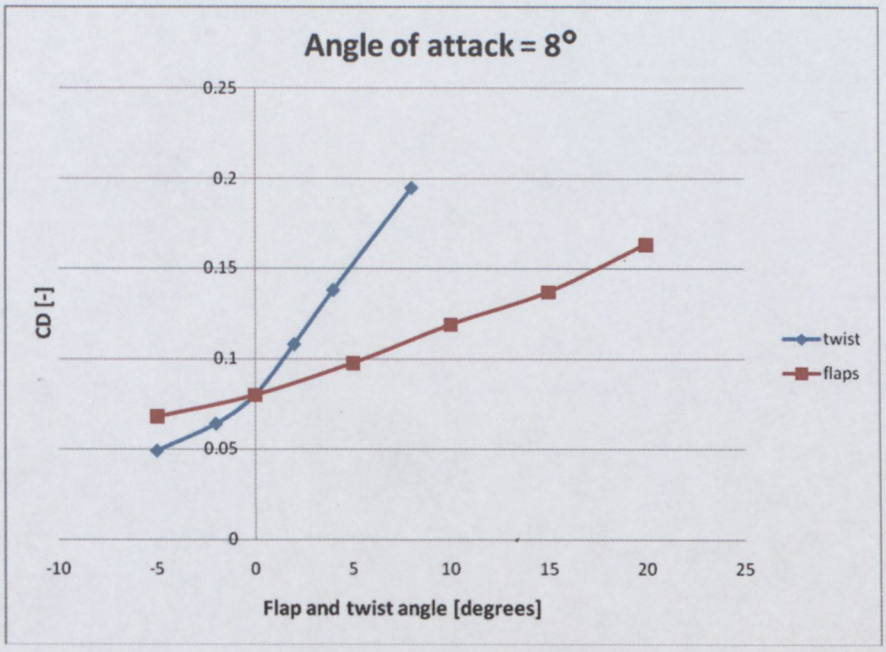
Angle of attack = 8°
0.25
0.2
0.15
0.1
0.05
0
CD [-]
-10
-5
0
5
10
15
20
25
Flap and twist angle [degrees]
twist
flaps

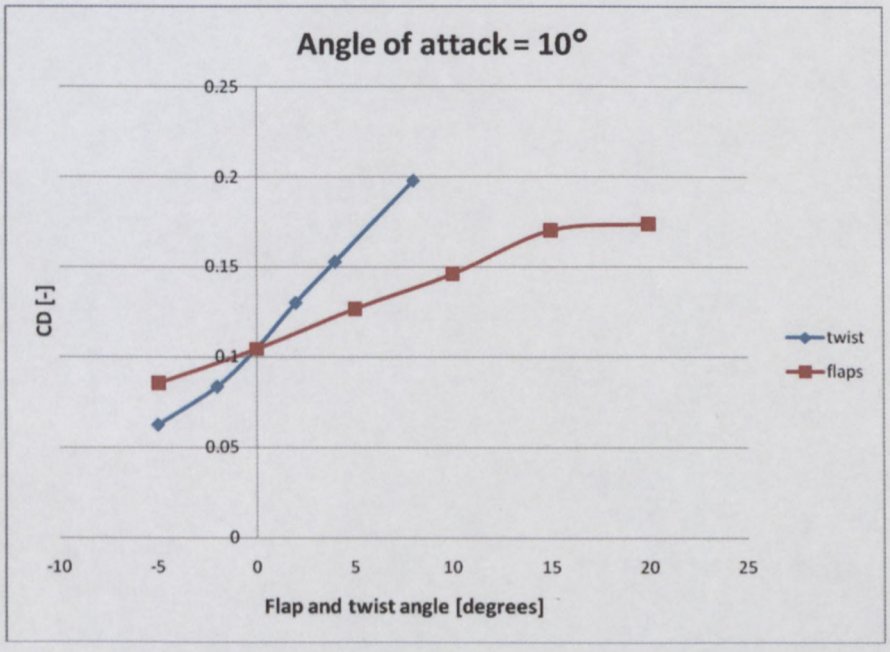
Angle of attack = 10°
0.25
0.2
0.15
0.1
0.05
0
CD [-]
-10
-5
0
5
10
15
20
25
Flap and twist angle [degrees]
twist
flaps

$CL^{3/2}$ / CD VS FLAP AND TWIST ANGLE

V = 16.667 m/s

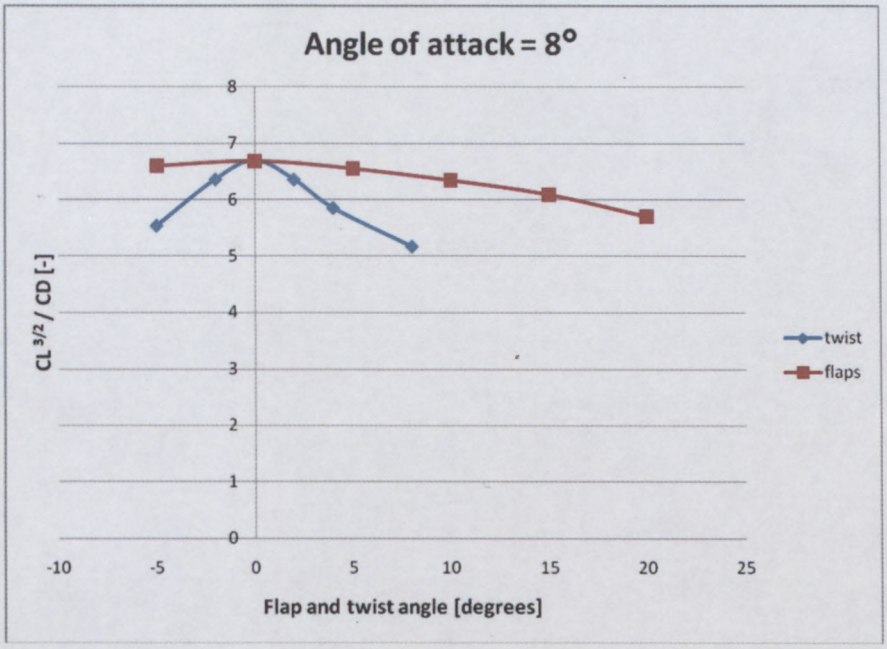

V = 18 m/s

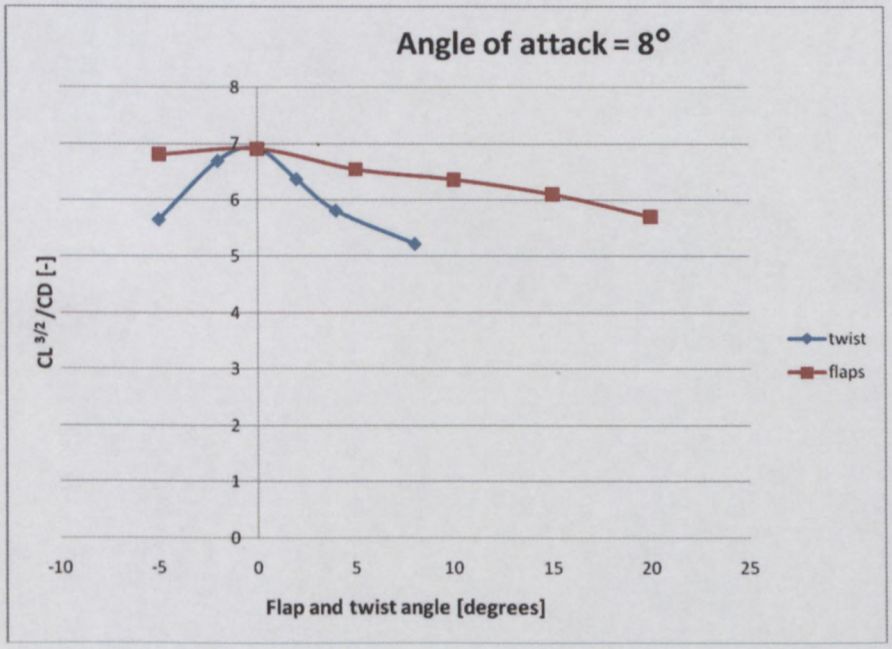

V = 22.22 m/s

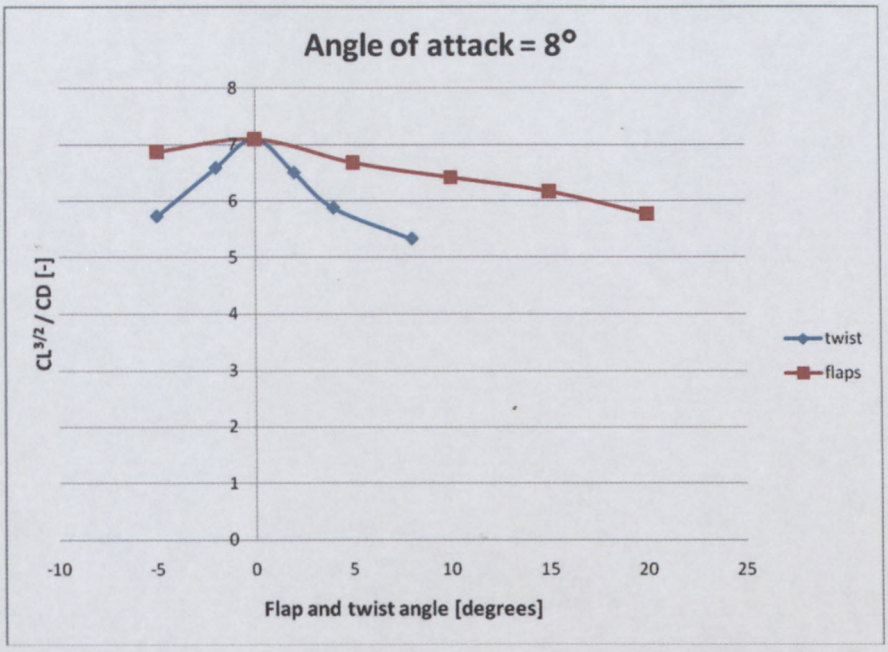

V = 33.33 m/s

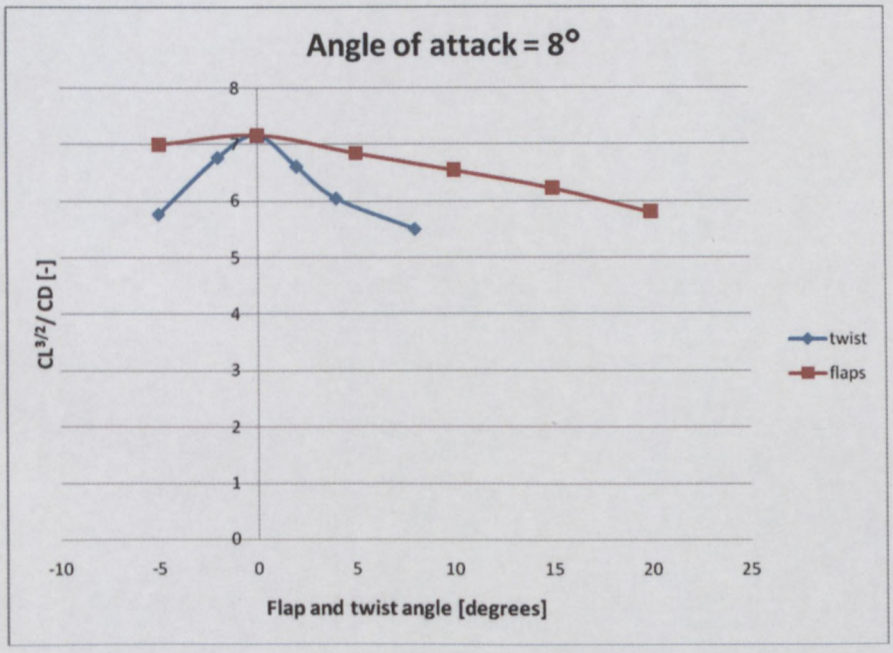

APPENDIX II

DETAILED DRAWINGS OF sVAI PROTOTYPE

Twisting Section

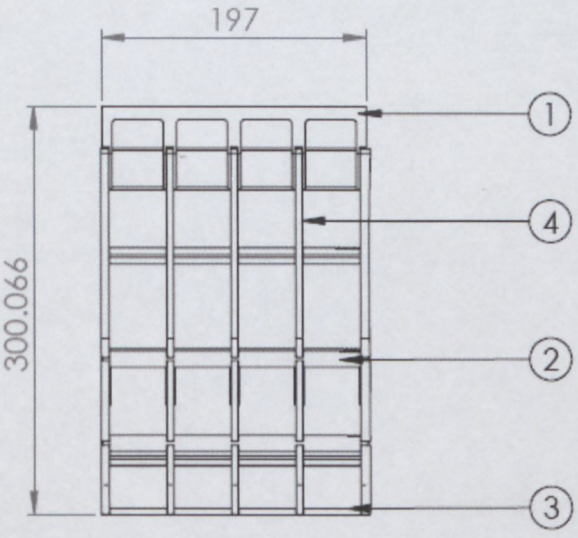

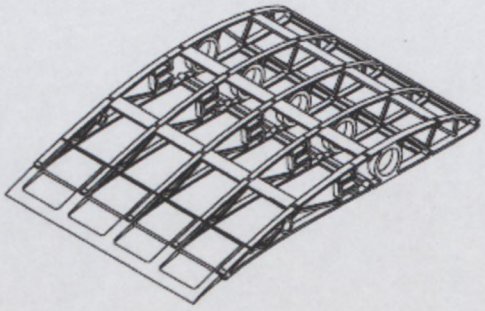

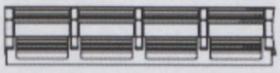

ITEM NO.	PART NUMBER	DESCRIPTION	QTY.
1	Trailing edge spacer beam		1
2	Mid-section spacer beam		3
3	Leading edge spacer beam		1
4	Longerine		5

Longerine Section

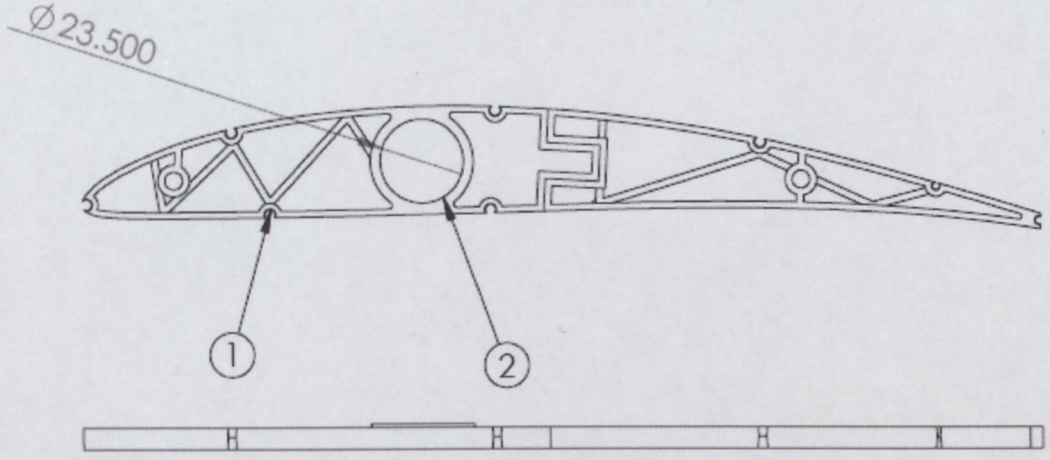

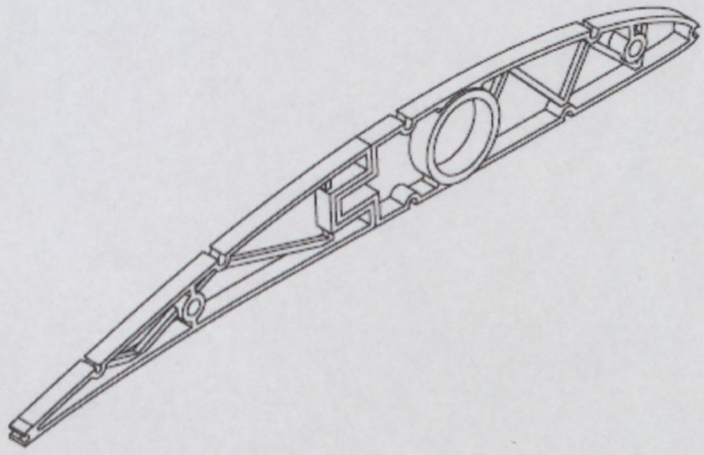

ITEM NO.	PART NUMBER	DESCRIPTION	QTY.
1	Spacer beam locators		8
2	Wing spar locator		1

Actuation System Assembly

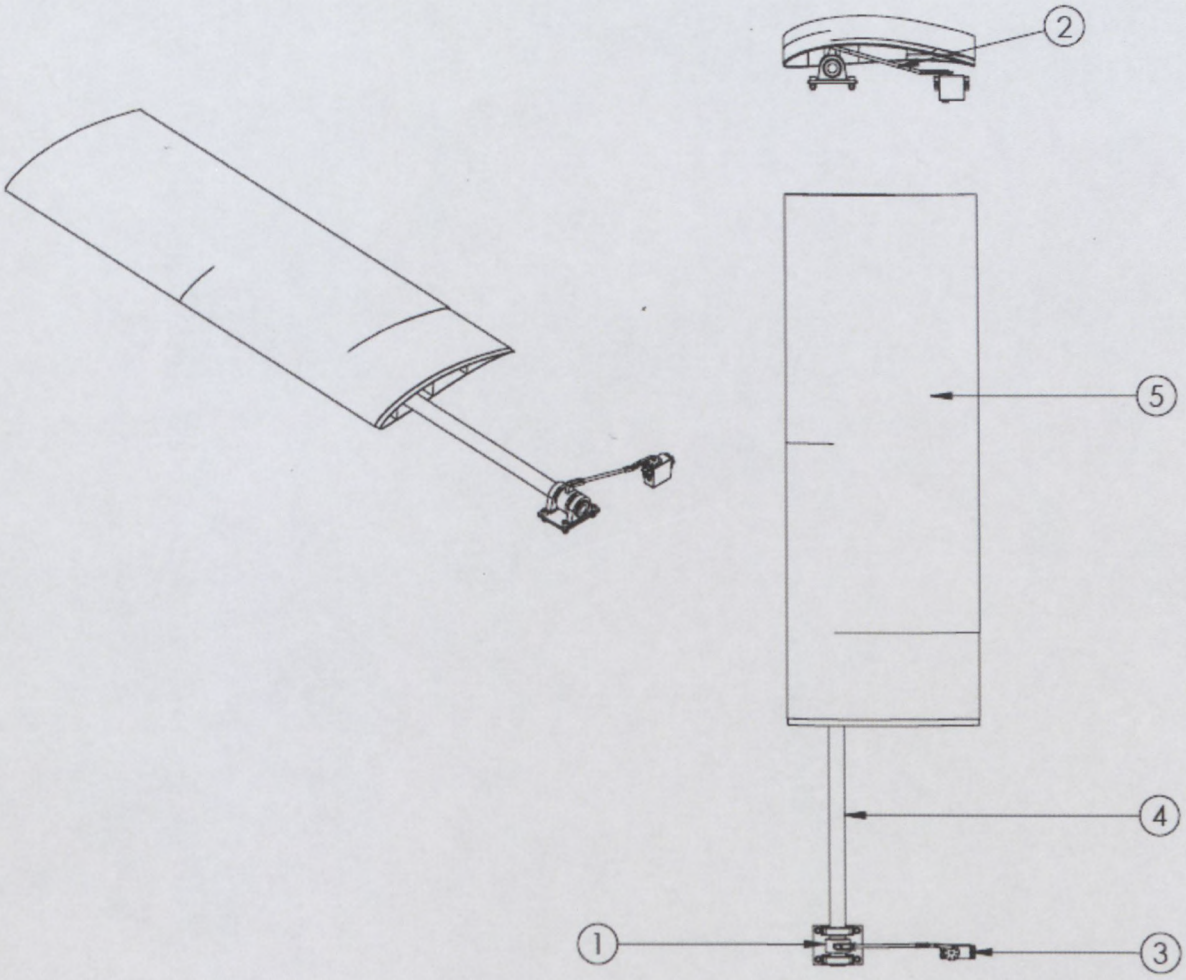

ITEM NO.	PART NUMBER	DESCRIPTION	QTY.
1	Leaver arm		1
2	Stay		1
3	Servo motor		1
4	Wing spar		1
5	Wing		1

REFERENCES

1. Kermode, A. C. 1996. *Mechanics of Flight*. 10th ed. Singapore: Longman Limited.

2. Manzo J. E. 2006. Analysis and Design of a Hyper-Elliptical Cambered Span Morphing Aircraft Wing. Master's thesis, Cornell University

3. Unmanned Aerial Vehicles. http://www.vectorsite.net/twuav.html

4. List of unmanned aerial vehicles. http://en.wikipedia.org/wiki/List_of_unmanned_aerial_vehicles

5. Blondeau, J. E. 2004. Development and Testing of a Variable Aspect Ratio Wing Using Pneumatic Telescopic Spars. Master's thesis, University of Maryland, College Park.

6. Henry, J. 2004. Roll Control for UAVs by use of a Variable Span Morphing Wing. Master's thesis, University of Maryland, College Park.

7. Poonsong, P. 2004. Design and Analysis of Multi-Section Variable Camber wing. Master's thesis, University of Maryland, College Park.

8. Historic Milestones in Aerospace, 2003. http://www.aerospaceweb.org

9. Johnston, C.O., Neal, D.A., Wiggins, L.D., Robertshaw, H.H., Mason, W.H., & Inman, D.J. 2003. A model to compare the flight control energy requirements of morphing and conventionally actuated wings. *AiAA journal*, 1716.

10. Anderson, J.D., Jr. 2008. *Introduction to Flight*. 6th ed. New York: McGraw-Hill.

11. Lazos, B. 2005. Biologically inspired fixed-wing configuration studies. *AIAA journal*, 42(5):1089-1098, Sep-Oct.

12. Lind R., M. Abdulrahim, K. Boothe, & P. Ifju. Morphing for Flight Control of Micro Air Vehicles. University of Florida

13. Ifju, P.G., Jenkins, D.A., Ettinger, S., Yongsheng, L., Shyy, W. & Waszak, M.R. 2002. Flexible-wing based micro air vehicle. *AIAA journal,* 0705.

14. Philips, W.F. 2003. Minimizing induced drag with geometric and aerodynamic twist on a wing of arbitrary planform. Utah State University.

15. W.F Philips, Alley N.R. & Goodrich W.D., "*Lifting-line analysis of roll control and variable twist*", Utah State University, 2004.

16. Anderson, J. D., Jr. 2007. *Fundamental of Aerodynamics*. 4th ed. New York: McGraw-Hill.

17. Pendleton, E.W., Bessette, D., Field, P.B., Miller, G.D., Griffin, K.E. 2000. Active aeroelastic wing flight research program: technical program and model analytical development. *Journal of Aircraft*, 37(4):554-561, July-Aug.

18. NASA. Active Aeroelastic Wing (AAW), 2008. http://www.nasa.gov/centers/dryden/news/ResearchUpdate/AAW/index.html

19. Gano, S.E. & Renaud, J.E. 2002. Optimized unmanned aerial vehicle with wing morphing for extended range and endurance. *AIAA journal*, 5668.

20. Burkett, C.W. 1989.Reduction in Induced Drag by the use of Aft Swept Wing Tips. *The Aeronautical Journal*, 93:400-405

21. Good, M.G. 2003. Development of a variable camber compliant aircraft tail using structural optimization. Master's thesis, State University, Blacksburg, Virginia.

22. Vishwanathan, A. 2007. Numerical investigation of wing morphing capabilities applied to a Horten type swept wing geometery. Master's thesis, West Virginia University, West Virginia.

23. UAVs. http://en.wikipedia.org/wiki/UAVs

24. Aeronautics, 2007. http://www.aeronautics-sys.com

25. Anderson, J.D., Jr. 1999 .*Aircraft Performance and design*. New York: McGraw-Hill Book Company.

26. Filippone, A. *Flight Performance of Fixed and Rotary Wing Aircraft*, American Institute of Aeronautics and Astronautics, Inc. and Butterworth-Heinemann, 2006.

27. Abbott, I.H.; Von Doenhoff, A.E. *Theory of Wing Sections*, Dover publications, INC. New York, 1959

28. Anderson, J.D., Jr. *Computational Fluid Dynamics*, McGraw-Hill Book Company, New York, 1995.

29. Versteeg, H.K.; Malalasekera, W. *An Introduction to Computational Fluids Dynamics. The Finite Volume Method*. 2nd ed. Prentice Hall, 2007

30. CFD Online, 2005. http://www.cfd-online.com/Wiki/Favre_averaged_Navier-Stokes_equations

31. Impac Systems Engineering, 2009. http://www.impacsystems.com/uploads/DimFam_web.pdf

32. Globalspec, 2009. http://materials.globalspec.com/Industrial-Directory/latex_rubber_property

33. Konical Minolta. Polygon Editing Tool, 2009. http://www.konicaminolta.com/instruments/products/software/polygon-editing-tool/index.html

34. Hardy, G.H.; Littlewood, J.E.; Pólya, G. *Inequalities*. 2nd ed. Cambridge University Press, 1988.